

AD-761 820

STATIC CONSTITUTIVE RELATIONS FOR CONCRETE

TERRA-TEK, INC.

PREPARED FOR
AIR FORCE WEAPONS LABORATORY

APRIL 1973

Distributed By:

NTIS

National Technical Information Service
U. S. DEPARTMENT OF COMMERCE

AFWL-TR-72-244

AFWL-TR-
72-244

AD 761820



STATIC CONSTITUTIVE RELATIONS FOR CONCRETE

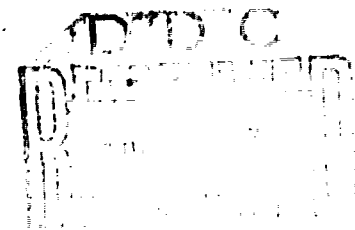
S. J. Green

S. R. Swanson

Terra-Tek, Inc.

TECHNICAL REPORT NO. AFWL-TR-72-244

April 1973



AIR FORCE WEAPONS LABORATORY

Air Force Systems Command

Kirtland Air Force Base

New Mexico

Approved for public release; distribution unlimited.

Reproduced by
NATIONAL TECHNICAL
INFORMATION SERVICE
U.S. Government Printing Office
Springfield, VA 22151

ACCESSION FOR	
NTIS	White Section <input checked="" type="checkbox"/>
DGC	Ball Section <input type="checkbox"/>
UNANNOUNCED	<input type="checkbox"/>
JUSTIFICATION	
BY	
DISSEMINATION SYMBOLS LIST 00000	
Dist.	Final Review Symbol
A	

AIR FORCE WEAPONS LABORATORY
Air Force Systems Command
Kirtland Air Force Base
New Mexico 87117

When US Government drawings, specifications, or other data are used for any purpose other than a definitely related Government procurement operation, the Government thereby incurs no responsibility nor any obligation whatsoever, and the fact that the Government may have formulated, furnished, or in any way supplied the said drawings, specifications, or other data, is not to be regarded by implication or otherwise, as in any manner licensing the holder or any other person or corporation, or conveying any rights or permission to manufacture, use, or sell any patented invention that may in any way be related thereto.

DO NOT RETURN THIS COPY. RETAIN OR DESTROY.

UNCLASSIFIED

Security Classification

DOCUMENT CONTROL DATA - R & D

(Security classification of title, body of abstract and indexing annotation must be entered when the overall report is classified)

1. ORIGINATING ACTIVITY (Corporate author) Terra-Tek, Inc. 815 East 4th South Salt Lake City, Utah 84102		2a. REPORT SECURITY CLASSIFICATION UNCLASSIFIED	
		2b. GROUP	
3. REPORT TITLE STATIC CONSTITUTIVE RELATIONS FOR CONCRETE			
4. DESCRIPTIVE NOTES (Type of report and Inclusive Dates) September 1970 through November 1972			
5. AUTHOR(S) (First name, middle initial, last name) S. J. Green and S. R. Swanson			
6. REPORT DATE April 1973		7a. TOTAL NO. OF PAGES 138	7b. NO. OF REFS 40
8a. CONTRACT OR GRANT NO. F29601-71-C-0016		8b. ORIGINATOR'S REPORT NUMBER(S) AFWL-TR-72-244	
D. PROJECT NO 5710			
C. Subtask SC157		9b. OTHER REPORT NO(S) (Any other numbers that may be assigned this report)	
d.			
10. DISTRIBUTION STATEMENT Approved for public release; distribution unlimited.			
11. SUPPLEMENTARY NOTES		12. SPONSORING MILITARY ACTIVITY AFWL (DEV) Kirtland AFB, NM 87117	
13. ABSTRACT (Distribution Limitation Statement A) Static constitutive stress-strain relations are developed for concrete at intermediate pressure levels, up to 10-12 ksi mean normal stress. An elastic-plastic model is developed that qualitatively fits the loading features exhibited for a variety of controlled laboratory tests conducted in this program and found in the literature. Laboratory tests were conducted on several batches of concrete with 3/8-inch maximum aggregate. Considerable attention was paid to the casting of the concrete so that batch-to-batch repeatability could be obtained, and to specimen preparation. Some data are presented for aggregate variation from 3/16-inch to 3/4-inch so that scaling to different aggregate could be performed. The laboratory tests presented represent a series of tests where all stresses and strains have been measured, thereby allowing the shear and dilation stress-strain responses to be observed during a variety of load-unload paths. Strain rate effects are not considered in the model developed, nor are the features of unloading correctly handled. Each of these represents an area where additional detailed work is needed.			

DD FORM 1473

NOV 65

UNCLASSIFIED

Security Classification

UNCLASSIFIED

Security Classification

14.

KEY WORDS

Concrete
Concrete testing
Constitutive relations
Stress-strain relations

1a

LINK A

LINK B

ROLE

ROLE

WT

ROLE

WT

UNCLASSIFIED

Security Classification

STATIC CONSTITUTIVE RELATIONS
FOR CONCRETE

S. J. Green
S. R. Swanson

Terra-Tek, Inc.

TECHNICAL REPORT NO. AFWL-TR-72-244

Approved for public release; distribution unlimited.

FOREWORD

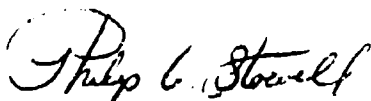
This report was prepared by Terra-Tek, Inc., Salt Lake City, Utah, under Contract F29601-71-C-0016. The research was performed under Program Element 61102H, Project 5710, Subtask SC157, and was funded by the Defense Nuclear Agency (DNA).

Inclusive dates of research were September 1970 through November 1972. The report was submitted 1 March 1973 by the Air Force Weapons Laboratory Project Officer, Captain Philip G. Stowell (DEV).

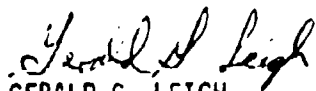
Thanks are given to Captain Stowell, Dr. M. Plamondon, and Major J. Galloway of the AFWL for technical comments during the performance of the contract.

Thanks are extended to Mr. S. W. Butters, Mr. R. M. Griffin and Dr. H. R. Pratt for technical support in the conduction of the experimental program. Thanks are also extended to Dr. W. Brace, M.I.T. and to Dr. W. Brown, University of Utah, for helpful discussions throughout the program; to Professor Press Linford, University of Utah, and Dr. J. Isenberg, Agbabian Associates, for assistance in casting the concrete; and to Mr. S. Snapp for contributing to the specimen preparation. Discussions and technical interchange with Dr. H. Read, Systems, Science and Software were very helpful.

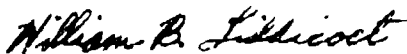
This technical report has been reviewed and is approved.



PHILIP G. STOWELL
Captain, USAF
Project Officer



GERALD G. LEIGH
Lt Colonel, USAF
Chief, Facility Survivability
Branch



WILLIAM B. LIDDICOET
Colonel, USAF
Chief, Civil Engineering Research
Division

ABSTRACT

Static constitutive stress-strain relations are developed for concrete at intermediate pressure levels, up to 10-12 ksi mean normal stress. An elastic-plastic model is developed that qualitatively fits the loading features exhibited for a variety of controlled laboratory tests conducted in this program and found in the literature. Laboratory tests were conducted on several batches of concrete with 3/8-inch maximum aggregate. Considerable attention was paid to the casting of the concrete so that batch-to-batch repeatability could be obtained, and to specimen preparation. Some data are presented for aggregate variation from 3/16-inch to 3/4-inch so that scaling to different aggregate could be performed. The laboratory tests presented represent a series of tests where all stresses and strains have been measured, thereby allowing the shear and dilatation stress-strain responses to be observed during a variety of load-unload paths.

Strain rate effects are not considered in the model developed, nor are the features of unloading correctly handled. Each of these represents an area where additional detailed work is needed.

(Distribution Limitation Statement A)

CONTENTS

<u>Section</u>		<u>Page</u>
I	INTRODUCTION	1
II	REVIEW OF EXISTING LITERATURE	3
III	EXPERIMENTAL TECHNIQUES	11
IV	EXPERIMENTAL DATA	29
V	THEORETICAL FORMULATION OF MODEL	52
VI	COMPARISON OF MODEL AND EXPERIMENT	66
VII	COMPARISON TO THICK-WALLED CYLINDER TESTS	87
VIII	SUMMARY AND CONCLUSIONS	99
	APPENDIXES	
	A Constitutive Equation Subroutine	101
	B Inelastic Thick-Walled Cylinder Program	107
	C Derivation of Equations for λ_1 and λ_2	117
	REFERENCES	121

ILLUSTRATIONS

<u>Figure</u>		<u>Page</u>
1	Effect of confining pressure on strength of concrete, from Newman and Newman (5).	5
2	Effect of triaxial stress state on strength of concrete.	6
3	Actual grading curves for batches cast.	12
4	Coring method used for obtaining solid cylinder test specimens.	15
5	Compression and tension test specimens.	17
6	Thick-walled, hollow-cylinder specimen.	18
7	Precision aligned loading press for unconfined tests.	20
8	Loading press and intensifier for confined tests.	21
9	Tests to determine the effect of different strain gages and the uniformity of strain.	23
10	Compressive loading of specimens with different length-to-diameter ratios.	25
11	28-day compressive strength of various batches cast.	27
12	Unconfined compression and tension tests.	30
13	Unconfined compression load beyond maximum stress.	31
14	Aging curve for batch tested.	33
15	Principal stress-strain curves for compressive loading under constant confining pressure.	34
16	Deviatoric stress-strain curves for constant confining pressure tests.	35
17	Dilatation stress-strain curves for constant confining pressure tests.	36
18	Stress paths for various tests.	39
19	Principal stress-strain curves for various load paths.	40
20	Dilatational stress-strain curves for various load paths.	41
21	Deviatoric stress-strain curves for various load paths.	42

ILLUSTRATIONS (continued)

<u>Figure</u>		<u>Page</u>
22	Maximum stress locus.	43
23	Triaxial compression load-unload at constant confining pressure of about 2 ksi.	45
24	Triaxial compression load-unload at constant confining pressure of about 2 ksi followed by compressive reloading unconfined.	46
25	Triaxial compression load-unload, reload-unload, reload path at constant confining pressure of about 2 ksi.	47
26	Triaxial compression load-unload, reload-unload path at constant confining pressure of about 2 ksi followed by compressive reloading unconfined.	48
27a	Photographs of tested solid cylinders (2.7 inch diameter by 6.0 inch long) loaded in compression.	49
27b	Photographs of tested solid cylinders (2.7 inch diameter by 6.0 inch long) deformed by tension or extension.	50
28	Illustration of compaction and bulking seen in volume behavior of porous materials.	53
29	Illustration of two yield surfaces used for porous material plasticity model.	55
30	Comparison of model and experimental dilatational curves for concrete in hydrostatic compression.	69
31	Comparison of model and experimental shearing stress-strain response in constant confining pressure tests.	70
32	Comparison of model and experimental dilatational stress-strain response in constant confining pressure tests.	71
33	Comparison of model and experimental shearing stress-strain response in constant $\sqrt{J_2}$ and constant J_1 tests.	72
34	Comparison of model and experimental dilatational stress-strain response in constant $\sqrt{J_2}$ and constant J_1 tests.	73
35	Comparison of model and experimental shearing stress-strain response in extension test.	74

ILLUSTRATIONS (continued)

<u>Figure</u>		<u>Page</u>
36	Comparison of model and experimental dilatational stress-strain response in extension test.	75
37	Comparison of model and experimental shearing stress-strain response in one-dimensional strain tests.	76
38	Comparison of model and experimental dilatational stress-strain response in one-dimensional strain tests.	77
39	Comparison of model and experimental stress path response in one-dimensional strain tests.	78
40	Comparison of model and experimental shearing stress-strain response in constant confining pressure load/unload test.	79
41	Comparison of model and experimental dilatational stress-strain response in constant confining pressure load/unload test.	80
42	Illustration of volumetric strain "S" used for correction of model parameter H_2 for different concrete.	84
43	Illustration of volumetric strain "T" used for correction of model parameter H_2 for different concrete.	84
44	Failure locus for Westerly granite (uniform stress).	86
45	Comparison of numerical and exact solution for elastic thick-walled cylinder.	89
46	Comparison of model and experiment for cylinder No. 7-1.	91
47	Comparison of model and experiment for cylinder No. 7-2.	92
48	Comparison of model and experiment for cylinder No. 7-3.	93
49	Comparison of model and experiment for cylinder No. 7-4.	94
50	Comparison of model and experiment for cylinder No. 8-2.	95
51	Comparison of model and experiment for cylinder No. 8-3.	96
52	Comparison of model and experiment for cylinder No. 8-4.	97

ILLUSTRATIONS (continued)

<u>Figure</u>		<u>Page</u>
53	Subroutine PLASTK flow chart.	102
54	Inelastic cylinder program flow chart.	107
55	Flow chart of elastic coefficient subroutine of cylinder program.	108
56	Flow chart of matrix solver subroutine of cylinder program.	108

ABBREVIATIONS AND SYMBOLS

$A_1, A_2, A_3, A_4, A_5, A_6$	notation for terms of λ_1, λ_2
B	bulk modulus
C_{ijkl}	elastic stress-strain matrix
d	specimen diameter
dF_1, dF_2	loading of yield surface segments
dK_1, dK_2	change in yield function constants
E	Young's modulus
F_1, F_2	segments of yield surface
f_c	unconfined compressive strength
G	shear modulus
$g_1 (J_1)$	function of J_1 in F_1 yield segment
h_1, h_2	hardening functions
J_1	stress invariant
K_1, K_2	yield function constants
L	Lamé constant
l	specimen length
p	pressure
p_m	mean normal stress
r	constant in F_2 yield segment
S, T	strains defined for present concrete
$d\varepsilon_v^p$	plastic volume strain increment
$d\sqrt{I_2}^p$	deviatoric invariant of plastic strain increments
$d\varepsilon_{ij}$	strain increment
$d\varepsilon_{ij}^e$	elastic strain increment
$d\varepsilon_{ij}^p$	plastic strain increment

$d\sigma_{ij}$	stress increment
$d\varepsilon_{vc}^p$	plastic volume strain
$\Delta V/V_0$	relative volume change
$\sqrt{J_2}$	deviatoric stress invariant
$\sqrt{I_2}$	deviatoric strain invariant
σ_A	axial stress
σ_c	unconfined compressive strength
σ_T	lateral stress
$\sigma_1, \sigma_2, \sigma_3$	principal stresses
$\sigma_{11}, \sigma_{22}, \sigma_{33}, \sigma_{12}, \sigma_{23}, \sigma_{31}$	stresses
$\varepsilon_1, \varepsilon_2, \varepsilon_3$	principal strains
$\varepsilon_{11}, \varepsilon_{22}, \varepsilon_{33}, \varepsilon_{12}, \varepsilon_{23}, \varepsilon_{31}$	strains
λ_1, λ_2	proportionality constants in flow law
ν	Poisson's ratio

SECTION I

INTRODUCTION

Concrete is a composite material of naturally occurring sand and gravels or crushed rock, bonded together by some form of cement, and may contain as many as eight different components. These include coarse aggregate, sand, unhydrated cement, cement gel, gel pores, capillary pores, air voids and free water. For many engineering purposes, concrete may be considered as a composite of aggregate, cement matrix, water and unfilled voids. This simplified model does not in any way imply that all concretes are similar in material response. Quite the contrary, 'concrete' alone is not adequate to specify a given material. The nature of concrete, including the complicated chemical reactions that take place, is well documented, for example by K. Newman (Ref. 1).

The response of concrete to either very rapid, quasistatic or long-term loading is quite different, and sufficient data are available to indicate that concrete exhibits a relatively complicated stress-strain response, very different from the frequently used approximation of linear elasticity. Under quasistatic loading nonlinear effects become particularly significant at stresses greater than about one-half the maximum stress, as indicated for example by the papers shown in Reference 2, "The Structure of Concrete" (1968). Under very rapid loading, concrete shows viscous response, and a recent report by Read and Maiden (Ref. 3) gives a good survey of the response of concrete to shock loading.

Even though plain concrete is a composite material, the work indicated here treats it as a homogeneous continuum. That is, the aggregate, cement matrix, water and voids are assumed to be distributed in a homogeneous manner,

and the geometry of the concrete specimen is assumed sufficiently large so that the size of the aggregate and voids are relatively small compared to the geometry of the specimen. Testing methods have recently become available to determine the bulk, or continuum, response of concrete for a variety of loading conditions (Ref. 4), which thereby makes the continuum approach to modeling the stress-strain response particularly attractive. Admittedly for some applications, such as shock loading where the load pulse may be small compared with size of the aggregate and voids, the continuum model may need additional detail. A reinforced concrete structure would need to be treated as a 'composite' structure consisting of the reinforcement in a concrete matrix, and the continuum model developed here would suffice to model the matrix.

The work here considers only quasistatic loading and does not address creep or high strain rates. The objective of this research was to develop general three-dimensional constitutive equations which qualitatively fit the features of deformation exhibited by concrete at intermediate pressures, up to 10-12 ksi, and to this end a variety of loadings were made on specimens from a specific laboratory cast batch of concrete.

A constitutive model was developed that represented the data obtained in this program. Although this model fits only the specific concrete studied, it could be applied to another concrete of interest by using different values for the constants involved.

SECTION II

REVIEW OF EXISTING LITERATURE

Strength: Considerable attention has been given to the tensile and compressive strength of plain concrete. The effect of mix ratios, aggregate size and grading, curing time and environment, have generally been investigated (Ref. 1 and 5). The water-cement mix ratio appears to have the greatest influence on strength, with lower water ratios giving greater strength. Different mixing and casting techniques can give different amounts of entrapped air, and hence, large differences in porosity.

Specimen design, fabrication and end conditions, or constraints, have likewise been investigated. Although 'casting' of specimens to the desired size and shape has been extensively used (Refs. 1,5,6), the surface mortar layer and nonuniformity of specimens due to the different casts may be less desirable than casting a single large block and diamond cutting or coring samples from the single casting. Compressive specimens with length to diameter ratio of two are generally considered adequate to obtain a region with uniform stress, while shorter specimens will undoubtedly exhibit non-homogeneous stress through the specimen (Ref. 7). The type of end lubrication used, if any, seems to vary; however, tests on hard rocks by Wawersik (Ref. 8) suggest that 'lubricants' may lead to low apparent strength caused by intrusion in pores and splitting of the end. End conditions which lead to apparent increased or decreased strength must carefully be separated from the effect of triaxial loading on strength. Although end effects due to unknown end conditions lead to triaxial stress loading in the specimen, the results will likely not be scalable or subject to interpretation.

Tests under triaxial compressive stress (Refs. 9-13) show that the compressive

strength of concrete is sensitive to confining pressure and increases rapidly with increases in confining pressure. Figure 1, taken from Newman and Newman (Ref. 5), illustrates this effect. This figure also shows that the classic expression of Richart, et al. (Ref. 9)

$$\sigma_1 = f_c + 4.1 \sigma_3$$

is inaccurate at the higher confining pressures.

Concrete tensile strength is *much* lower than compressive strength, but the ratio of these strengths depends on the mix parameters (Ref. 14). A ratio of uniaxial compressive strength to tensile strength of about ten may be considered typical although ratios on the order of twenty have been observed (Ref. 13).

Tests under triaxial extension stress (Refs. 12,13) and under biaxial stress (Refs. 15,16,17) indicate that strength is not only sensitive to confining pressure but is also more precisely dependent upon the stress state. For example, the maximum stress difference is greater in triaxial compression than in triaxial extension at the same confining pressure, as shown by Figure 2 which is a replot of data by Hobbs (Ref. 13).

The tension plus biaxial compression data of McHenry and Karni (Ref. 18), Bresler and Pister (Ref. 19) and others as summarized by Newman and Newman (Ref. 5) all indicate that a steady reduction in tensile strength results as the biaxial compressive stress is increased. This can be seen in Figure 2 which also indicates that as the lateral compressive stress is raised, a point is reached where the axial stress is zero. This should correspond to the biaxial strength under equal biaxial stresses, and thus provides a comparison point between the two kinds of tests. Further increases in the lateral compressive stress produce failure under axial compressive stress, again as illustrated

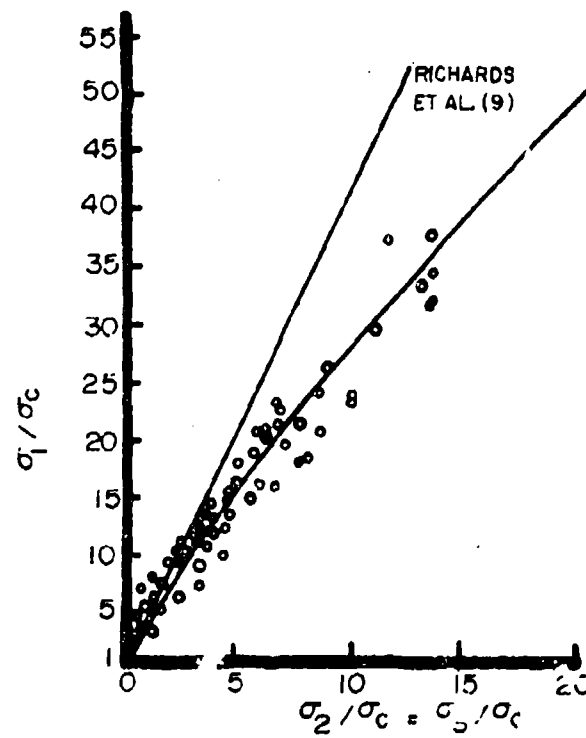


Figure 1. Effect of confining pressure on strength of concrete, from Newman and Newman (5).

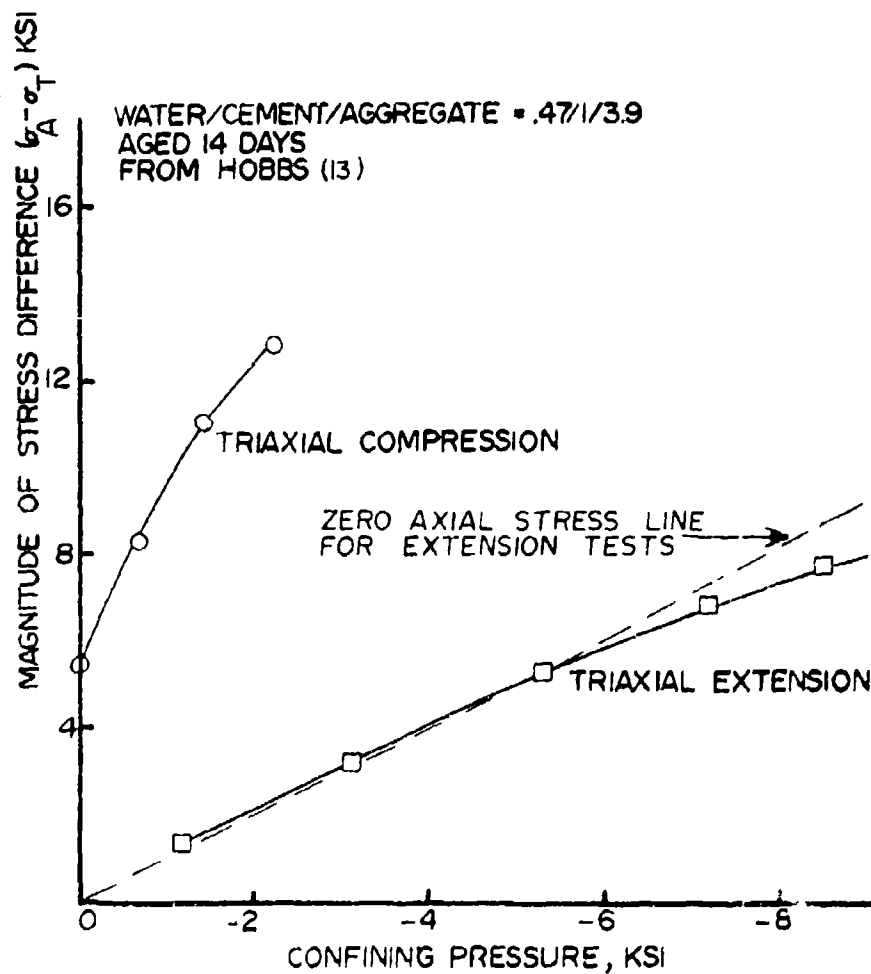


Figure 2. Effect of triaxial stress state on strength of concrete.

in Figure 2.

The strength of concrete under biaxial compressive loading has been investigated by Kupfer, Hilsdorf and Rusch (Ref. 15) using special brush platens to minimize adverse end conditions. A strength increase of 16 percent in equal biaxial compression relative to uniaxial compression was obtained, which is in accord with the value of 10 to 25 percent suggested by Newman and Newman (Ref. 5). This value is not universally obtained; for example, the extension tests of Chinn and Zimmerman (Ref. 12) show an increase of approximately 110 percent in equal biaxial compressive strength over uniaxial compressive strength.

A number of failure criteria have been proposed to predict concrete strength under general multiaxial stress conditions. A recent review by Newman and Newman (Ref. 5) indicates that this is not a settled issue. The classic Mohr-Coulomb criteria states that strength can be described by

$$\sigma_1 - \sigma_3 = f(\sigma_1 + \sigma_3)$$

This expression has been used by a number of investigators. For example, the expression by Richart, et al. (Ref. 9) given previously can be put in this form with f being a linear function. However, the Coulomb-Mohr hypothesis implies that the strength value does not depend on the intermediate principal stress, in variance with biaxial test results. Bresler and Pister (Ref. 19) and McHenry and Karni (Ref. 18) have used a generalization of the Mohr-Coulomb criterion in which the octahedral shear stress is taken as a function of the octahedral normal stress. A good fit to data in the mixed tension-compression stress range was obtained.

Chinn and Zimmerman (Ref. 12) found that neither the Mohr theory nor the octahedral stress generalization fit their compression and extension test

results. This conclusion was supported by Mills and Zimmerman (Ref. 20). They proposed that their data could be fitted by using a modification of the octahedral shear stress, however, the application of this theory was not presented.

Stress-Strain Response: During loading in uniaxial compression, concrete behaves in a nearly linear elastic manner up to about half the maximum stress, where significant microcracking begins. Unloading from above this stress level will result in permanent set, while continued loading will eventually result in massive break up of the concrete microstructure and large scale dilation as maximum stress is neared (Refs. 1,5). Careful control of the testing machine strain rate allows the complete stress-strain curve to be obtained (Refs. 8,21), and shows that fracture does not occur immediately after reaching peak load. The load tends to drop with increasing strain, with large scale cracking, slabbing and complete loss of cohesion occurring well after peak load. Specimens loaded to slightly beyond peak load and then unloaded may show no macrocracks, and in general have the appearance of an undeformed specimen.

The stress level at the onset of significant microcracking is termed the "discontinuity stress" (Ref. 5) and can be observed by deviations from linearity in the stress-strain response. The microcracking has been detected by a number of methods including microscopic and X-ray examination of specimen exterior and cross section surfaces, measurement of acoustic emissions, and other methods (Ref. 5). A measurement of all three principal strains permits the calculation of the relative change in volume. Increases in volume (relative to the elastic deformation) due to microcracking have been observed by a number of investigators (Ref. 5).

Concrete is capable of large deformations under confining pressure.

Chinn and Zimmerman (Ref. 12) applied axial strain of 16% to triaxial compression specimens at confining pressures of 25 ksi or more, and many other investigators have noted similar increases in maximum axial deformation (Refs. 10,11,13). The stress-strain response becomes significantly non-linear at high deformations and permanent set upon unloading is large.

Measurement of all principal strains has not received widespread attention, and, in general, insufficient data are available to define the triaxial stress-strain response. Also relatively little data exist to determine the unloading and reloading path, the effect of varying amounts of free water (dry or saturated), temperature and thermal cycling or other preconditioning effects on the triaxial stress-strain response.

Concrete Constitutive Laws: Little previous work has been performed on developing constitutive equations that even reasonably represent the triaxial stress-strain response of concrete. This is likely due to two factors; first, that experimental techniques for measuring all the independent components of the strain tensor with sufficient accuracy have only recently become available, and secondly, the usage of large computers that can effectively utilize more accurate (and perhaps complicated) stress-strain representations has only recently become common. Because of this, the stress-strain behavior of plain concrete has usually been modeled as either elastic or elastic-perfectly plastic. Nilson (Ref. 22) has presented a typical computer program for structural analysis of reinforced concrete using nonlinear properties. However, an adequate representation of the necessary properties was not available.

On the basis of a careful study of the stress-strain behavior of several rocks, Swanson (Ref. 23) and Brown and Swanson (Ref. 4) proposed that a strain hardening plasticity model could be used to phenomenologically represent the

features of dilatancy (bulking) and permanent set. Baron, et al. (Ref. 24) have added to the model a strain hardening "capped" yield surface that was particularly appropriate for modeling soils, because the capped yield surface permitted some control over the amount of dilatancy exhibited by the plasticity model. Recently Swanson (Ref. 25) has shown how his earlier strain hardening model could be combined with a capped yield surface in a manner appropriate for some porous rocks.

Herrmann (Ref. 26) has recently given a survey of constitutive equations for the shock compaction of porous materials, but only briefly touches on general three-dimensional stress-strain response.

SECTION III

EXPERIMENTAL TECHNIQUES

Concrete Mix: Smooth aggregate was selected which contained very small percentages of crushed, irregular, or elongated material. The primary mineralogical components are sandstone, quartzite, limestone/marble, granite, gneiss, and schist, which are naturally occurring around Salt Lake City, Utah. The aggregate is generally rounded to subangular because it is stream deposited material. To achieve a minimum aggregate to specimen cross section ratio of one to five, 3/8 inch was selected as the maximum aggregate size for the detailed tests on thick-walled, hollow cylinders and solid cylinders, with some unconfined compression tests run on different batches of concrete having 3/16, 1/2, and 3/4 inch maximum aggregate sizes to investigate the strength dependence on maximum aggregate size.

Grading curves were selected for the four different aggregates so as to maintain the overall surface area per unit of concrete weight (in^2/lb) constant within the resolution of the calculations, estimated at $\pm 30\%$. This was considered important since surface area is a major factor in establishing the water/cement ratio. The surface area was calculated for the aggregate by assuming all aggregate was spherical in shape. This calculation was thus only approximate.

The aggregate/cement ratio by weight of 6.3/1 was selected to afford a 'medium workability' (Ref. 27) of the 3/8-inch aggregate mix. Figure 3 shows the actual grading curves, where the percentages are given as weight percentages of the total aggregate passing through the screen size indicated. A single lot of aggregate was obtained and stored for all batches cast, and a laboratory check analysis was run on each aggregate mixture to determine the

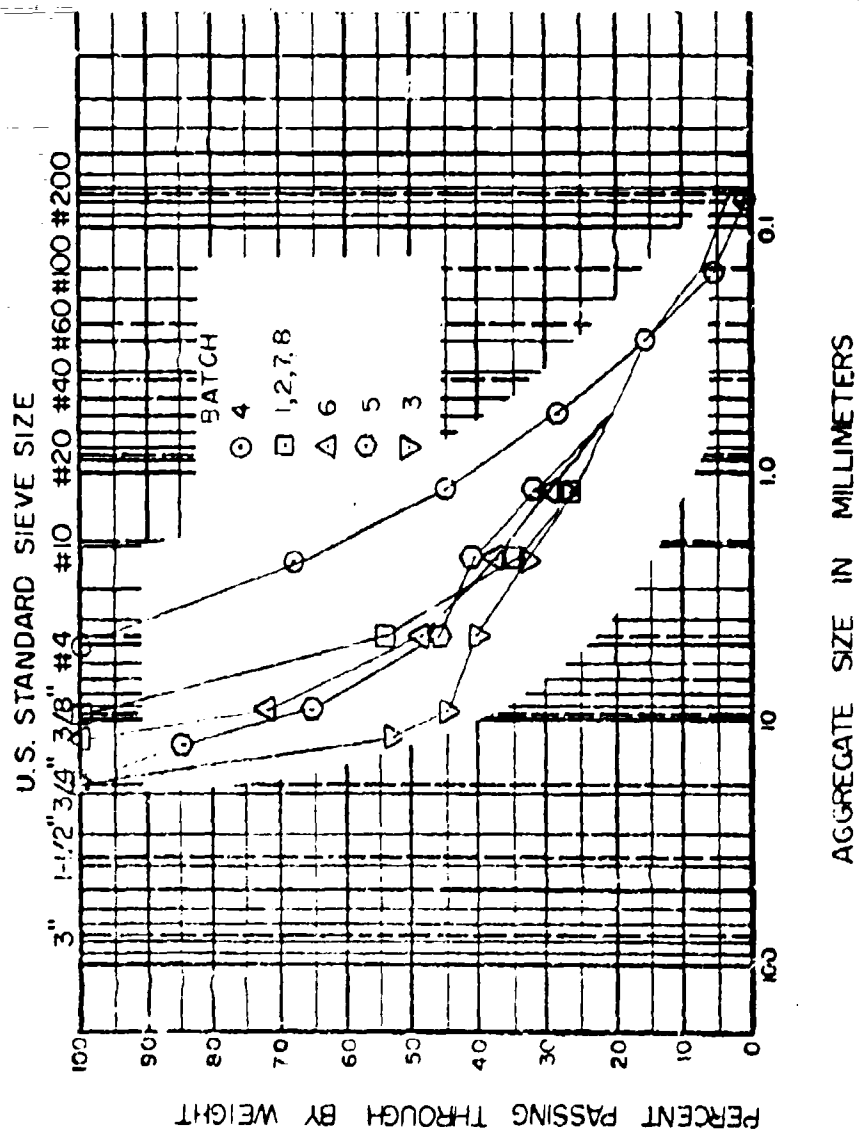


Figure 3. Actual grading curves for batches cast.

actual grading curve.

A water/cement ratio (by weight) of 0.6, and a Type I Portland cement were selected. To ensure homogeneity of the cement, a local supplier ran a special batch which was bagged directly from the mixer. This one lot was used for all concrete batches cast. Table I presents the batches cast.

Table I
Concrete Specimen Batches

Batch No.	Maximum Aggregate Size, Inches	Comments
1	3/8	1 tub, inadequate vibration
2	3/8	1 tub
3	3/4	1 tub, different surface area
4	3/16	1 tub
5	3/4	1 tub
6	1/2	1 tub
7	3/8	1 tub, plus 5 hollow cylinders
8	3/8	5 hollow cylinders

Mixing, Pouring and Curing: The desired amount of graded aggregate was weighed and placed in a 5-cubic foot drum mixer, and mixed several minutes to ensure an even distribution. A sample was taken for moisture analysis, and the mixer was sealed with a clear plastic film. A moisture analysis, which entailed careful weighing, then heating to 250°F and weighing at 30-minute intervals until no further weight loss was observed, was run on the aggregate sample. A dry aggregate weight of 1% was allowed as normal interstitial water content, and the remainder was considered as excess water which reduced the amount of water added to the mix.

Appropriate cement and water quantities were weighed and added to the mixer to bring the water, cement, 1% moisture aggregate ratio by weight to

0.6 / 1 / 6.3. The batch was mixed 5 minutes and then poured into approximately 2-foot diameter tubs (to be cored later for solid cylinders) or in forms for hollow cylinders. The tubs were vibrated 15-20 seconds with a 1½-inch diameter commercial concrete vibrator and the forms for thick walled cylinders lesser amounts. In general, this amount of vibration was adequate to stop air bubbles from appearing on the surface and to produce only very slight amounts of water at the surface.

The concrete was moved immediately to a constant temperature-humidity curing room. After 4 days the forms were removed and the cast specimens covered with saturated burlap material kept moist by absorption from water reservoirs. Solid cylinder specimens were wet diamond core drilled from the tubs at about 20 days and then placed under water for continued curing (except for a few specimens as noted later). Some specimens were removed from the water at 24 days to be ground on sides and ends, strain gaged, and then tested at 28 days. Other specimens remained submerged until about 80 days and then were kept in the constant temperature (78°F)/constant humidity (40%) room until time of test.

Specimen Preparation - Solid Cylinders: Solid cylinders were core drilled to about 2 3/4-inch diameter using a water lubricated diamond core bit on a large vertical drill press as shown in Figure 4 with each specimen marked for identification and location in the larger block. By using proper core bit, feed, speed, lubrication, and very rigid alignment, solid cylinders were obtained with no appreciable chipping or loosening of the exposed aggregate. No indication of internal cracking was suggested by either microscopic observation or by scatter in tensile or compressive strengths. The solid cylinders were ground to 2.7-inch diameter with a tolerance of .001 inch on roundness and straightness. Thereafter they were cut and ground to length,

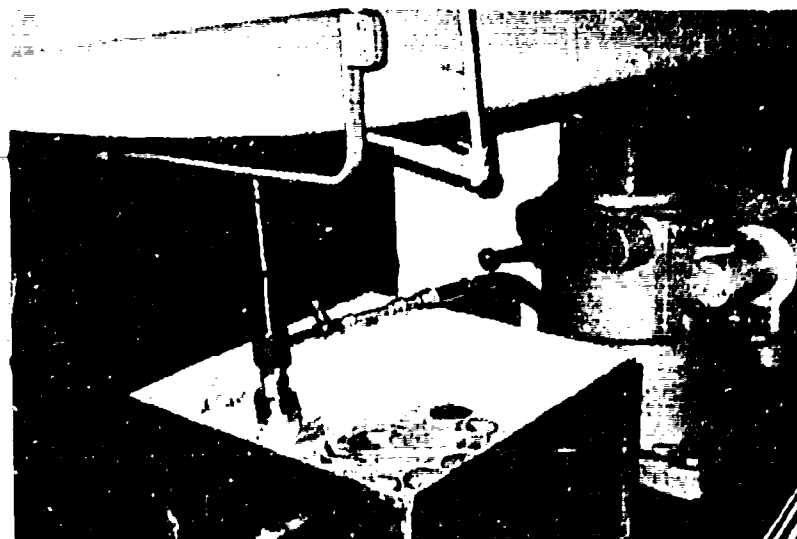


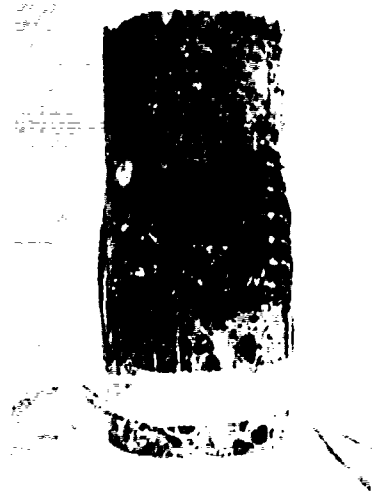
Figure 4. Coring method used for obtaining solid cylinder test specimens.

(6 inches for most of the tests) parallel and flat to within .0003 inch.

Specimens for unconfined tests had strain gages applied directly to the concrete surface with commercial strain gage adhesives. Typically gages were applied at the specimen center in axial and transverse orientations spaced 180° apart around the specimen. Foil gages with a 3/4-inch gage length (Micro Measurements EA-06-750DT-120) were selected for most of the tests, as discussed later. Terminal strips and leads were attached, and the specimens appeared as shown in Figure 5a. For tensile testing, aluminum alloy tension grips were epoxy bonded to the specimen ends, as shown in Figure 5b.

Specimens for tests under confining pressure had large surface voids filled with a fine commercial grout, and then a .005-inch-thick soft aluminum sleeve was shrunk onto the specimen with about a .005-inch interference fit. Strain gages were bonded to the aluminum jacket as shown in Figure 5c, and the specimen was then sealed in tygon tubing as shown in Figure 5d. The effect of the aluminum sleeve on strength was considered negligible (Refs. 4,28).

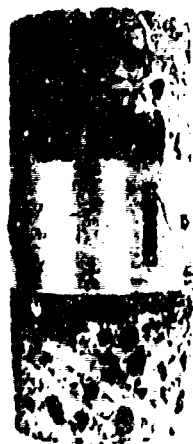
Specimen Preparation - Hollow Cylinders: The thick-walled, hollow-cylinder specimens to be tested in axial compression and internal pressurization (hoop tension) were cast in forms 7 inches inside diameter by 11 inches outside diameter by 20+ inches long. The metal forms, as illustrated in Figure 6a, were removed after 4 days, and the specimens were covered inside and out with saturated burlap material. At about 20 days the specimens were placed under water until about 80 days. The specimen ends were diamond ground flat and perpendicular to the specimen axis, to within .001 inch. The inside of the cylinders were lightly sandblasted with fine grit to expose subsurface voids (which might collapse under internal pressure), and these voids were filled



a. UNCONFINED COMPRESSION



b. UNCONFINED TENSION



c. CONFINED COMPRESSION
OR TENSION



d. COMPLETELY SEALED SPECIMEN

Figure 5. Compression and tension test specimens.



a. FORMS FOR CASTING



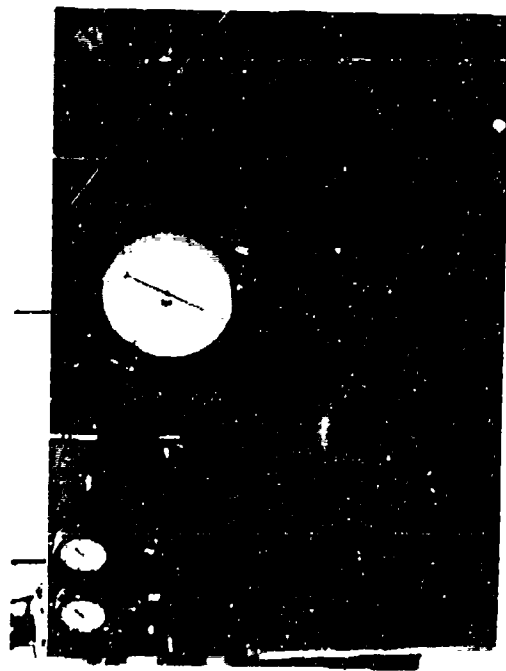
b. FULLY INSTRUMENTED SPECIMEN

Figure 6. Thick-walled, hollow-cylinder specimen.

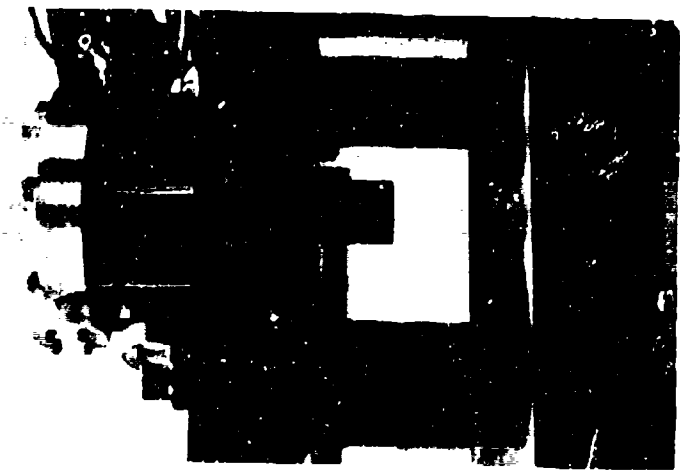
with a fine commercial grout. Because of the matrix cement surface layer inherent in cast specimens, 2-inch-long foil strain gages (Micro Measurements EA-06-20CBW-120) were selected (as opposed to 3/4-inch-long gages) for use on the hollow cylinders. The gages were applied at about the specimen center internally and externally at axial and transverse directions 180° apart. A specimen ready for testing is shown in Figure 6b.

Testing - Solid Specimens: Specimens were tested using a very stiff, well aligned servocontrolled press. The press for unconfined tension and compression tests is shown in Figure 7. Load was measured from a precalibrated load cell and strains from high elongation strain gages directly mounted on the test specimen as previously discussed. Axial strain rate was kept constant at 10^{-4} /second by the servocontrolled press, and because of the high stiffness of the press the compressive stress-strain curve beyond maximum stress was recorded in some cases.

For tests on solid cylinders under confining pressure, a test vessel and loading press shown in Figure 8a were used. The specimen was aligned inside the test vessel, with a precalibrated load cell and pressure measuring manganin coil inside the test vessel. Strains were again measured by high elongation strain gages directly mounted on the specimen, with a pressure correction of $+0.5 \times 10^{-8}$ /psi (Ref. 29) applied to all strain gage readings (which was generally insignificant for the pressures tested here). Kerosene was used as the fluid inside the test vessel, with pressure generated by a servocontrolled intensifier shown in Figure 8b. The manganin pressure coil inside the test vessel, a strain gage on the specimen, or the load cell, provided the input signal to control the intensifier unit such that the desired pressure or load, or the desired specimen strain condition was met. Axial strain rate was generally kept at 10^{-4} /second, as for the unconfined tests.

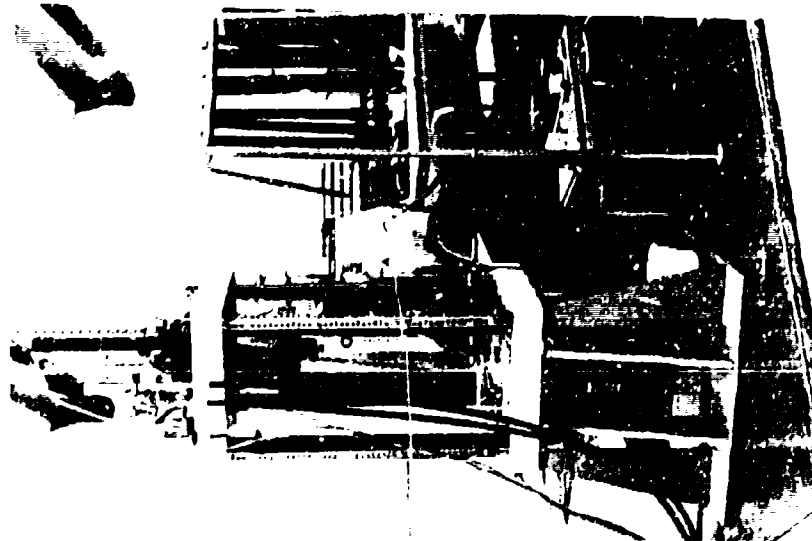


a. CONTROL PANEL

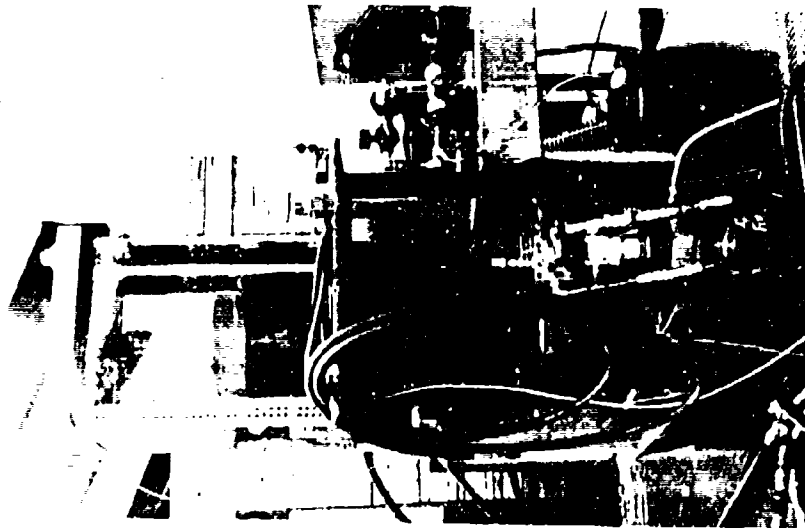


b. LOADING PRESS

Figure 7. Precision aligned loading press for unconfined tests.



a. LOADING PRESS AND VESSEL



b. INTENSIFIER RIG

Figure 8. Loading press and intensifier for confined tests.

All signals were recorded in analog form with direct signal calibration. Load and pressure are accurate to $\pm 2\%$, while strains are somewhat less accurate with uncertainty mainly due to the porous, inhomogeneous nature of the concrete. Repeatability of stresses and strains from similar tests on adjacent concrete specimens was $\pm 3-4\%$. No specimen end lubrication was used for compression tests; the concrete was loaded directly against a steel end platen.

Preliminary Tests: The sign convention adopted throughout this report is that tensile stress and extensional strain are positive, and compressive stress and shortening strain are negative. Axial refers to length of the specimen and transverse to the diameter. No apparent anisotropy was noted from visual or microscopic examinations, and no difference in strength or stiffness was noted for different directions; therefore, no distinction has been made between transverse strains, and in general, isotropic behavior is assumed.

Variation in Strain Gage Size: Previous work reported in the literature has suggested that strain gage readings on concrete and mortar specimens are a measure of the average strains to within at least 5%, as long as the gage length is greater than four times the maximum aggregate size (Ref. 30). To better determine the effect of strain gage size on strain reading, several 2.7-inch diameter by 6.0-inch long specimens were prepared and tested in unconfined compression with 2.0-inch long (>5 times maximum aggregate dimension), 0.75-inch long and 0.5-inch long strain gages applied directly to the specimen and adjacent to each other, to indicate axial strain. The strain indication difference between the longest and shortest gages was less than 8%, with essentially no difference between the 2.0-inch and 0.75-inch long gages, as shown in Figure 9a. Since experience had revealed that larger strain gages are more subject to failure at confining pressure because they are more likely

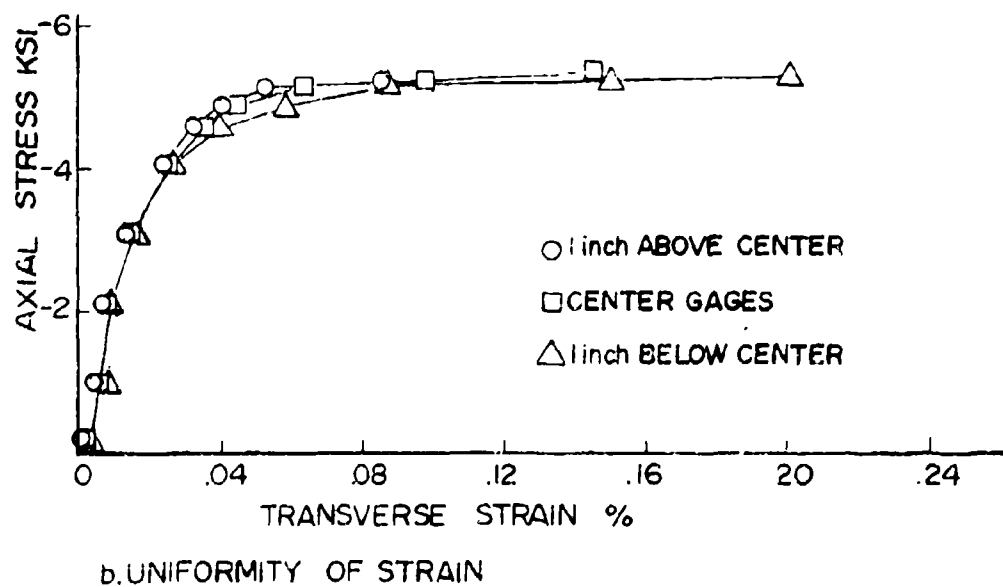
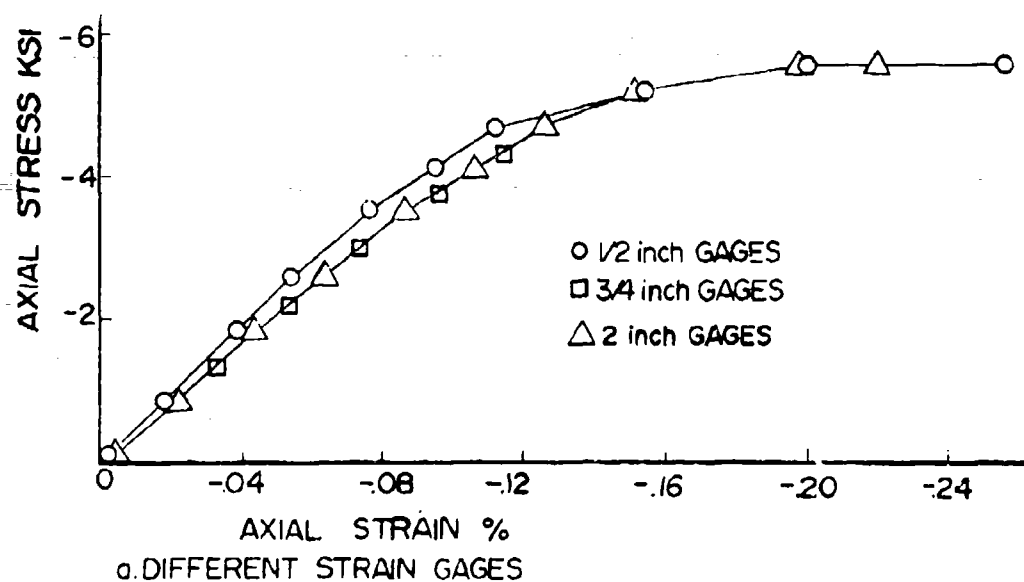
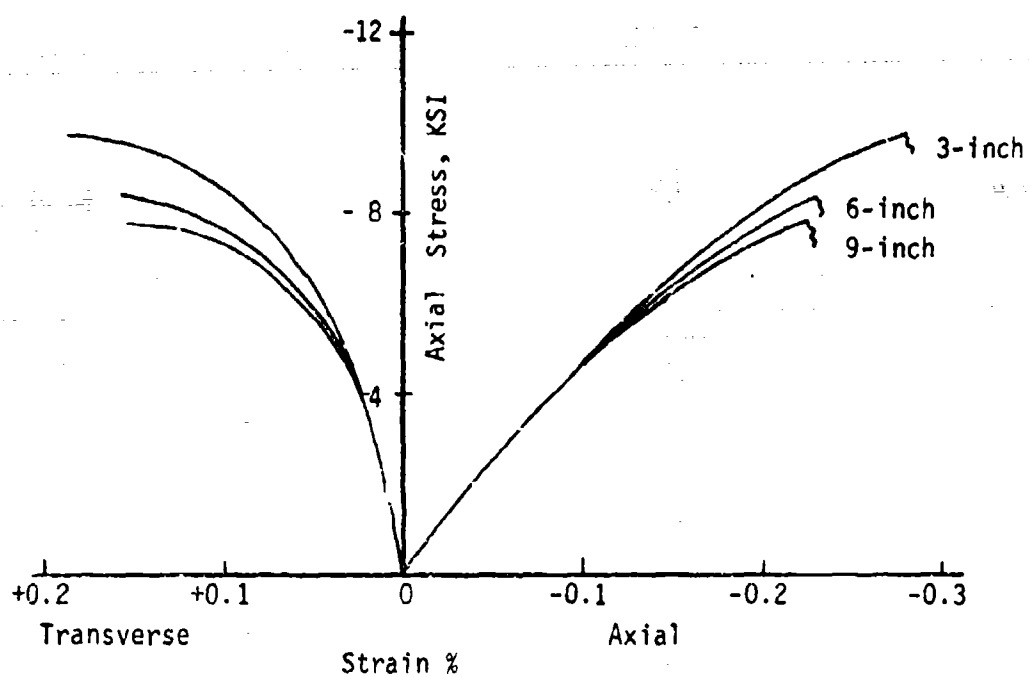


Figure 9. Tests to determine the effect of different strain gages and the uniformity of strain.

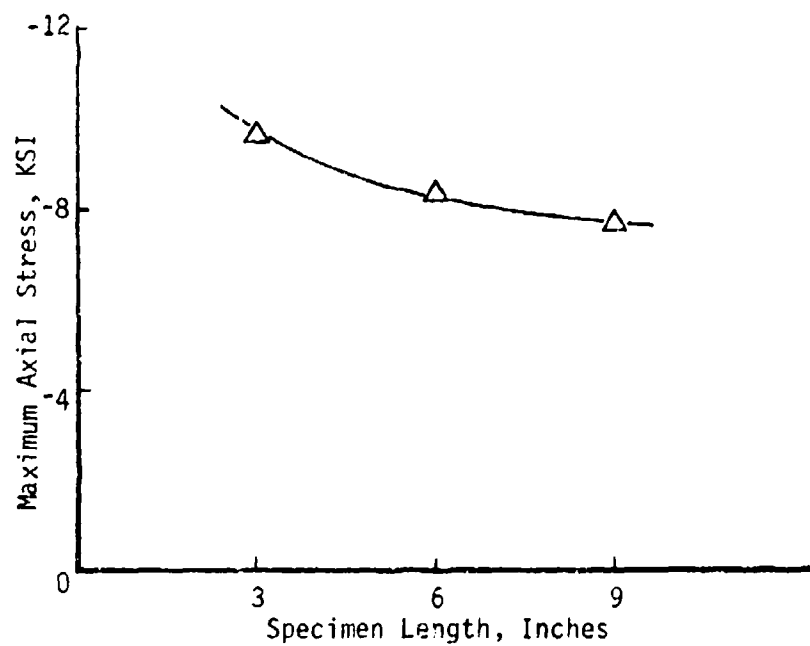
to cover and be deformed into specimen voids, the gage length selected was 0.75 inch, which is twice the maximum aggregate size (for most tests).

Cylinder Length/Diameter Ratio: Newman and Lachance (Ref. 31) and Johnson and Sidwell (Ref. 7) suggest a length over diameter (l/d) ratio of >2.5 to ensure freedom from end effects in the central gage section. To verify an adequate length to diameter ratio for our test techniques, several 2.7-inch diameter by 6.0-inch long specimens were instrumented with three 0.75-inch long strain gages to indicate transverse strains over about a 2-inch center section length of the specimen. These were specimens from batch 2 cured about 28 days. One gage was located at the center of the specimen and one gage 1 inch above and 1 inch below center, with lateral strain selected as the most sensitive indication of end effects since typical specimen barreling, due to the end constraint, would be indicated by lateral gages. The three lateral strains were uniform to $<5\%$ difference for specimens tested without lubrication between platens and specimen, as shown in Figure 9b.

To further investigate the effect of specimen configuration on apparent physical properties, unconfined compression tests were run on specimens with l/d ratios of 1.1, 2.2 (similar to the previous tests) and 3.3 (nominal 3, 6, and 9-inch lengths by 2.7-inch diameter). These were specimens from batch 2 cured for about 90 days, but not under water. The stress-strain curves indicate that all specimens exhibit an initial tangent modulus (slope of axial stress-axial strain curve at near zero stress) of 4.7×10^6 psi $\pm 8\%$ as seen in Figure 10a; however, maximum loads were 9710, 8270, and 7660 psi for l/d ratios of 1.1, 2.2, and 3.3, respectively, as plotted in Figure 10b. This represents a 17% apparent strength reduction from 3 to 6-inch specimen length, but only a 7% reduction from 6 to 9 inches, further indicating that a l/d of 2.2 is adequate for tests here (7% is considered small, of the



a. STRESS - STRAIN CURVES



b. MAXIMUM STRESS

Figure 10. Compressive loading of specimens with different length-to-diameter ratios.

order of batch scatter as will be shown later). From these tests it was found that the effects are negligible for our techniques, if a 1/d ratio is maintained.

Variation in Aggregate Size: To determine the effect of maximum aggregate size on strength, 28-day unconfined compressive tests were performed on specimens with maximum aggregate sizes of 3/16, 3/8, 1/2, and 3/4 inch (2.7-inch diameter by 6.0-inch long specimens). Aggregate specific surface area was held constant by selecting grading curves to give an appropriate distribution of various sizes of aggregate in each mix. Other concrete parameters were also held constant, as listed below.

- Cement
- Water-cement ratio
- Aggregate-cement ratio
- Mixing time and technique
- Pouring time and technique
- Vibrating time and technique
- Curing time and technique
- Specimen preparation

Maximum stress increases only slightly with increasing aggregate size as shown in Figure 11. A strength decrease of less than 11% was observed with decrease in maximum aggregate size from 3/4 to 3/16 inch. These values cannot be compared directly with other published tests, for example that given by Walker and Bloem (Ref. 32) for 3/8 and 3/4-inch aggregates, since no attempt was made to hold specific surface area constant for different aggregate mixes in these other testing programs.

One concrete batch with 3/4-inch maximum aggregate (batch 3) was mixed with a specific surface area (in^2/lb) about 20-50% lower than the other batches. The strength was 17% lower than the other 3/4-inch aggregate, batch 5, with the weakening believed to occur because the lower surface area ties up less water in surface bonding and effectively increases the water available for hydration,

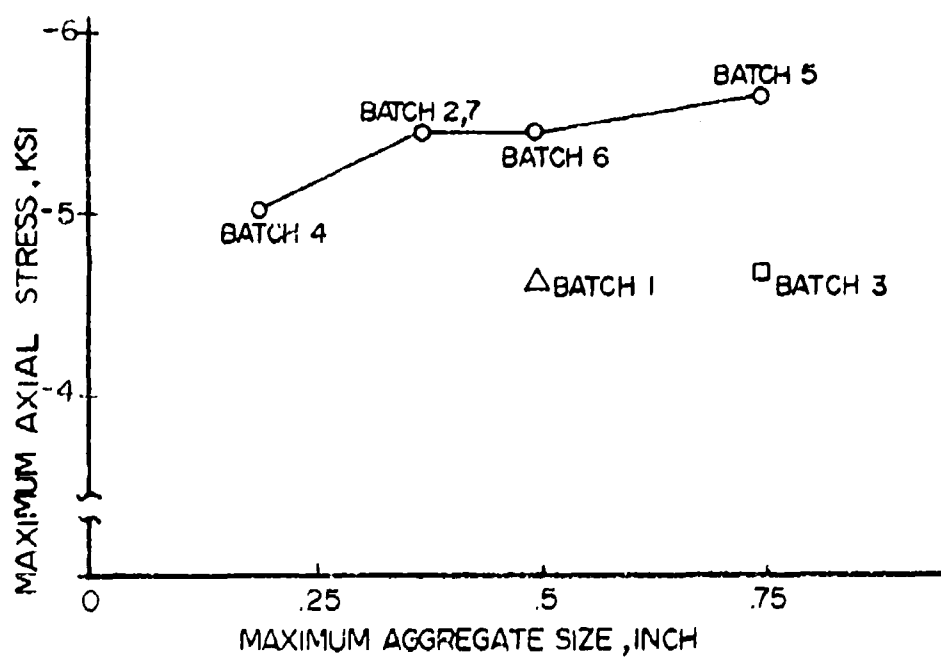


Figure 11. 28-day compressive strength of various batches cast.

or equivalently this gives an effective increase in the water-cement ratio, which is known to produce weaker concrete (Ref. 27). In another batch, about 50% less vibration during casting resulted in excessive air entrapment and substantially weakened concrete, as shown by the point for batch 1 on Figure 11.

From these tests on variable aggregate size concretes it is concluded that the strength is more dependent on aggregate surface area than on aggregate size, and that careful aggregate grading with consideration for specific surface area is required to produce concrete with similar properties. Furthermore, such sensitivity to pouring and casting processes points out the need for extreme quality control in obtaining test specimens.

SECTION IV

EXPERIMENTAL DATA

All tests reported in this section were conducted on 2.7-inch diameter by 6.0-inch long solid cylinders, cast and aged for greater than 200 days. The tests were performed on servocontrolled machines that maintained a constant axial strain rate of 10^{-4} /second. Specimens were nominally 'dry', in that they had been exposed to dry laboratory environment for several days prior to test, and tests were performed at room temperature, about 70°F. Average density at the time of test was $2.27 \pm .03$ g/cc.

Unconfined Tests: Figure 12a shows the results of compression tests, with engineering stress plotted versus engineering strain, while Figure 12b shows the tension test results. Each curve is the average of 2-4 tests with material scatter shown as bars on the curves. The apparent elastic modulus is about 6×10^6 psi in compression and 7×10^6 psi in tension, with an unconfined compressive strength of 7020 psi and a tensile strength of 805 psi.

If the test machine is adequately controllable, the decreasing stress part of the stress-strain curve can be readily mapped as was done in Figure 13 where a compression specimen was loaded beyond maximum stress and unloaded, then reloaded until large scale slabing occurred (as shown by the picture in insert). Visible, prominent axial cracks and slabing occur well after maximum compressive stress. In tension fracture occurs mainly through the mortar, with fracture seldom running through the aggregate (Refs. 1,5). This fracture pattern is quite different than for extension tests, which are discussed later.

The aging of concrete is generally well documented (Refs. 1,5) and shows a rapid increase in strength during the first 28 days followed by slower increase in strength for the next 60 days, and relatively little increase in strength

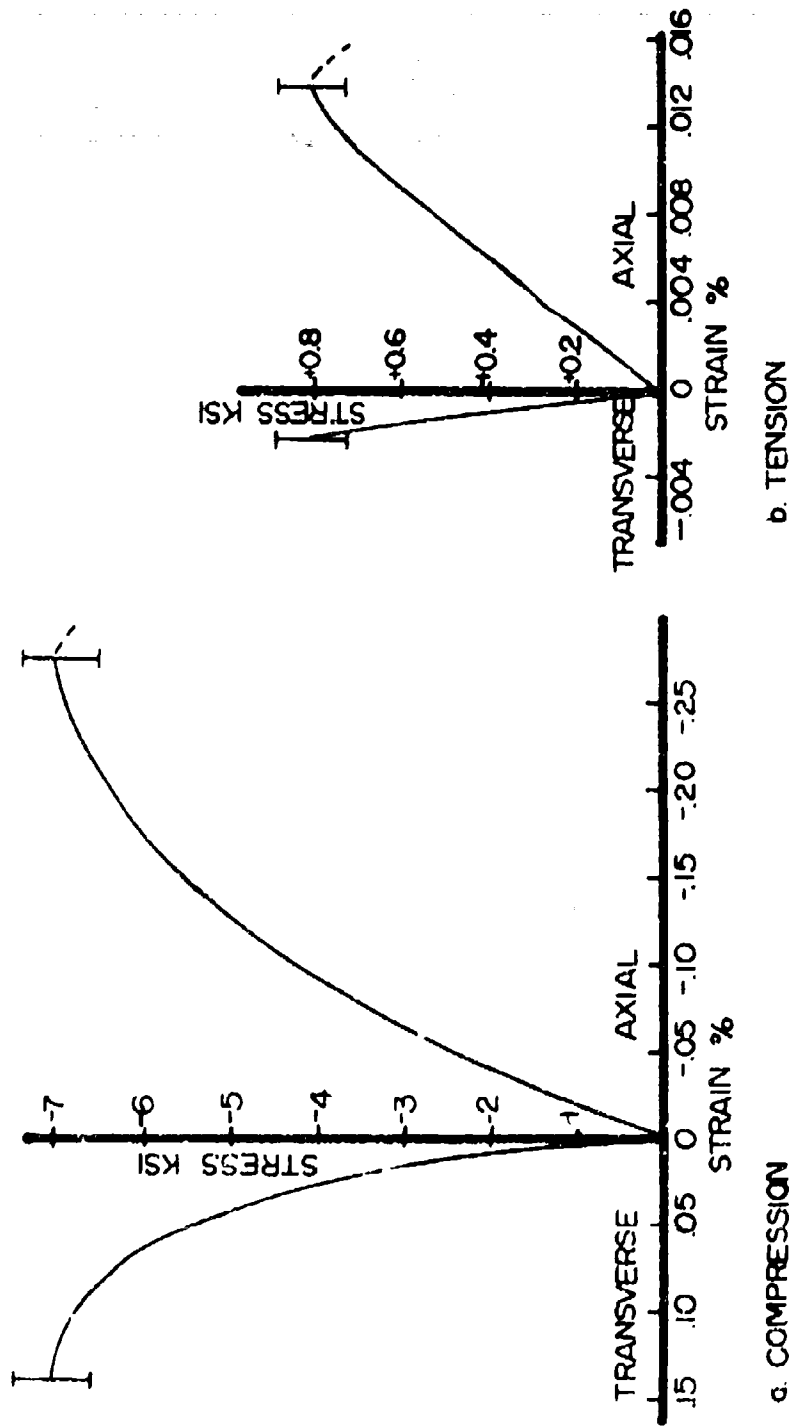


Figure 12. Unconfined compression and tension tests.

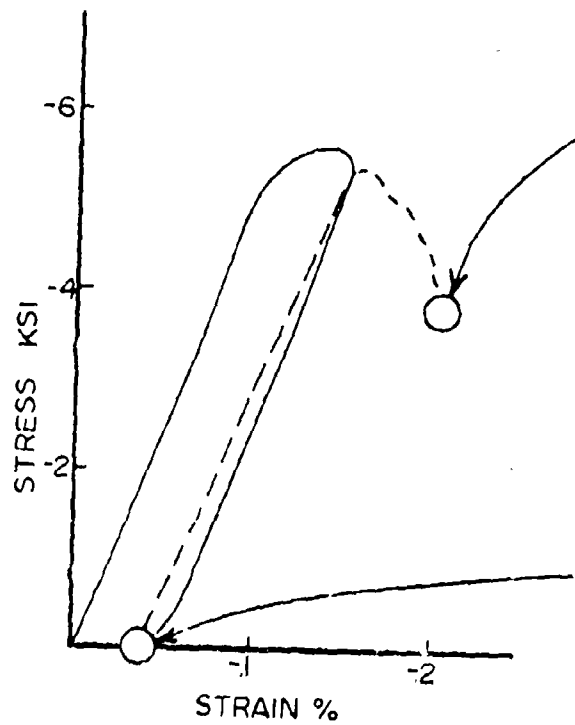


Figure 13. Unconfined compression load beyond maximum stress.

after 90-100 days. The strength of the concrete tested here is plotted versus log time in Figure 14.

Constant Confining Pressure Tests: Compression tests were conducted at constant confining pressure of 0.5, 1.0, 2.0 and 3.0 ksi. Strains were obtained only at 0, 1.0 and 2.0 ksi. The compressive stress (difference) versus axial shortening and transverse extension strains are shown in Figure 15, with each curve the average of 4-6 tests and scatter as shown by bars. Increased strength is shown with confining pressure, quantitatively agreeing with other data available (Ref. 5). At 2 ksi confining pressure ductile behavior is shown, and relatively large compressive strains are possible. The negative ratio of transverse to axial strains (the apparent Poisson ratio) and the slope of the stress difference-shortening strain curve (the apparent Young's elastic modulus) near zero stress difference increase slightly with confining pressure.

The data from the constant confining pressure tests are replotted in the shear plane in Figure 16 and in the dilatation plane in Figure 17. In Figure 16 the square root of the second deviatoric invariants of stress and strain are plotted (equal to $2/\sqrt{3}$ times shear stress and $1/\sqrt{3}$ times engineering shear strain, respectively), with each defined as shown below in terms of principal stresses, $\sigma_1, \sigma_2, \sigma_3$ and principal strains, $\epsilon_1, \epsilon_2, \epsilon_3$ (Ref. 33).

$$\sqrt{J_2'} = (1/\sqrt{6}) \sqrt{(\sigma_1 - \sigma_2)^2 + (\sigma_2 - \sigma_3)^2 + (\sigma_1 - \sigma_3)^2} \quad (1)$$

$$\sqrt{I_2'} = (1/\sqrt{6}) \sqrt{(\epsilon_1 - \epsilon_2)^2 + (\epsilon_2 - \epsilon_3)^2 + (\epsilon_1 - \epsilon_3)^2} \quad (2)$$

The slope of this curve is equal to twice the apparent shear modulus, G . The values taken near zero shear stress ($\sqrt{J_2'} < 0.005$ ksi) increase only

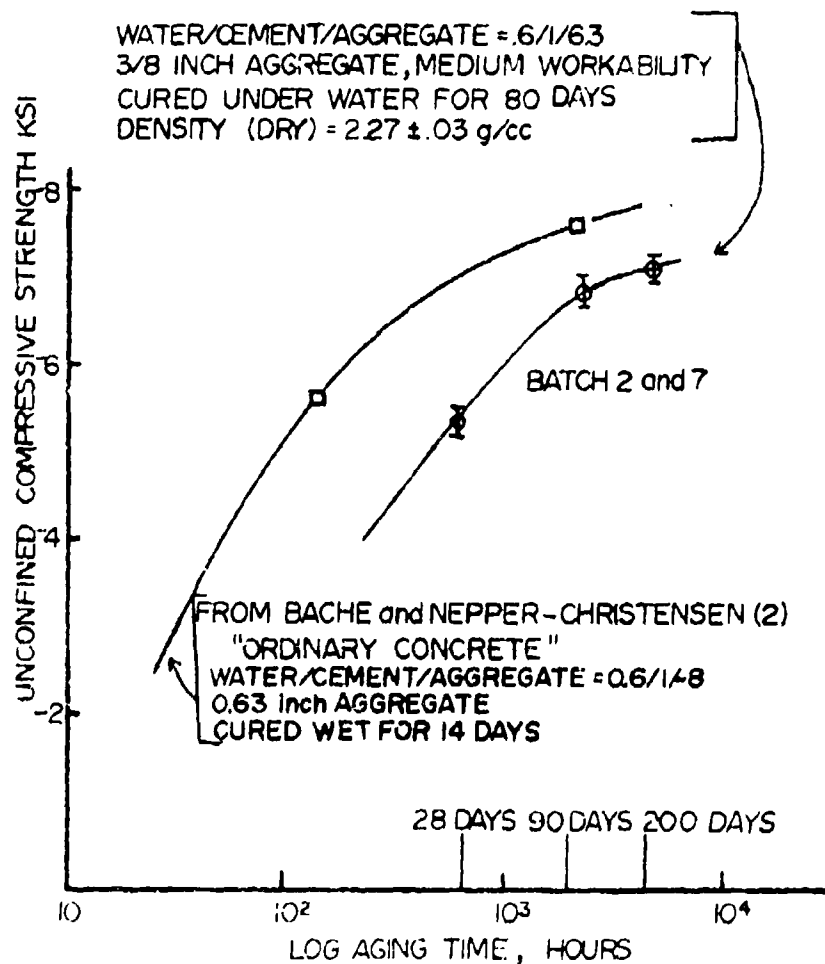


Figure 14. Aging curve for batch tested.

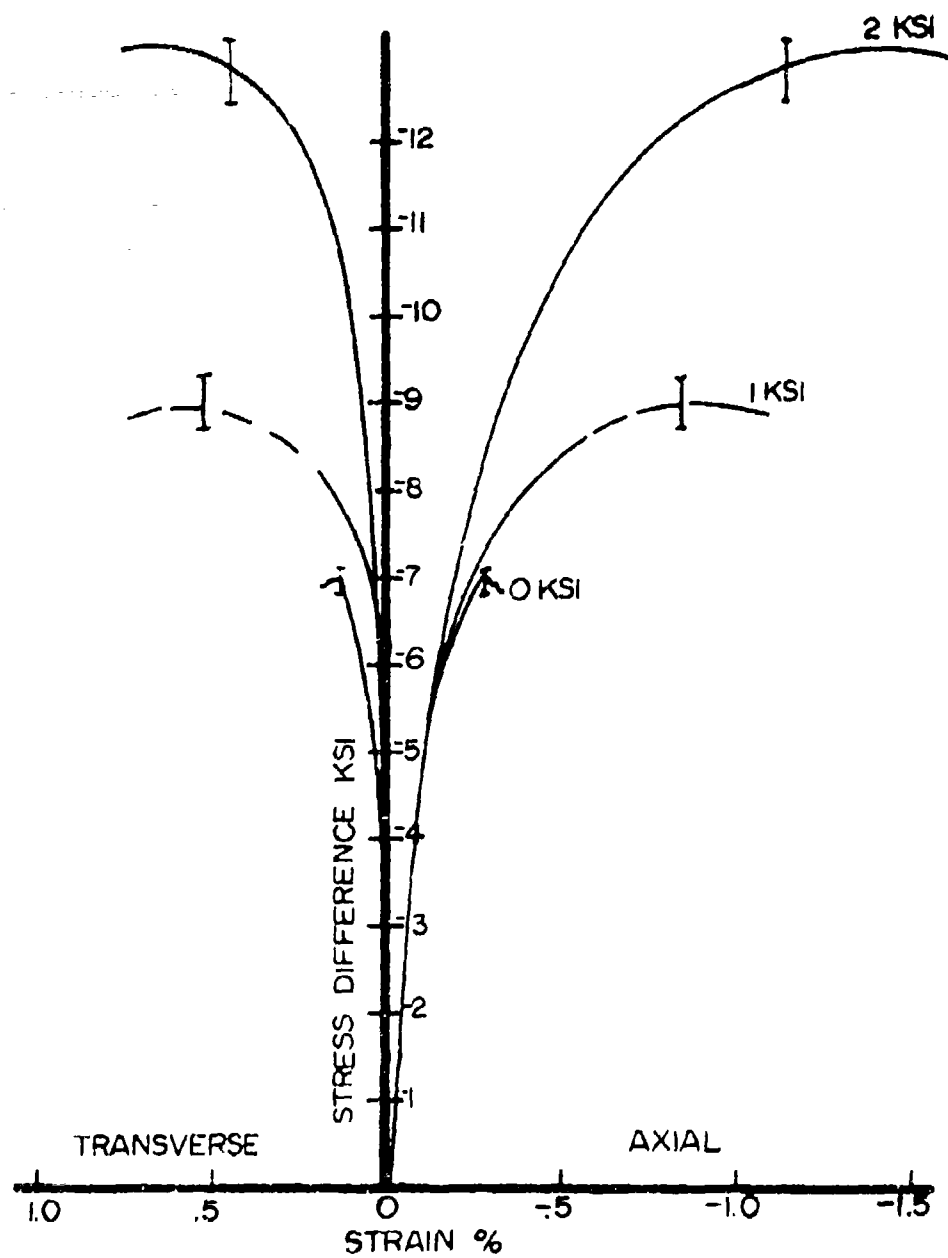


Figure 15. Principal stress-strain curves for compressive loading under constant confining pressure.

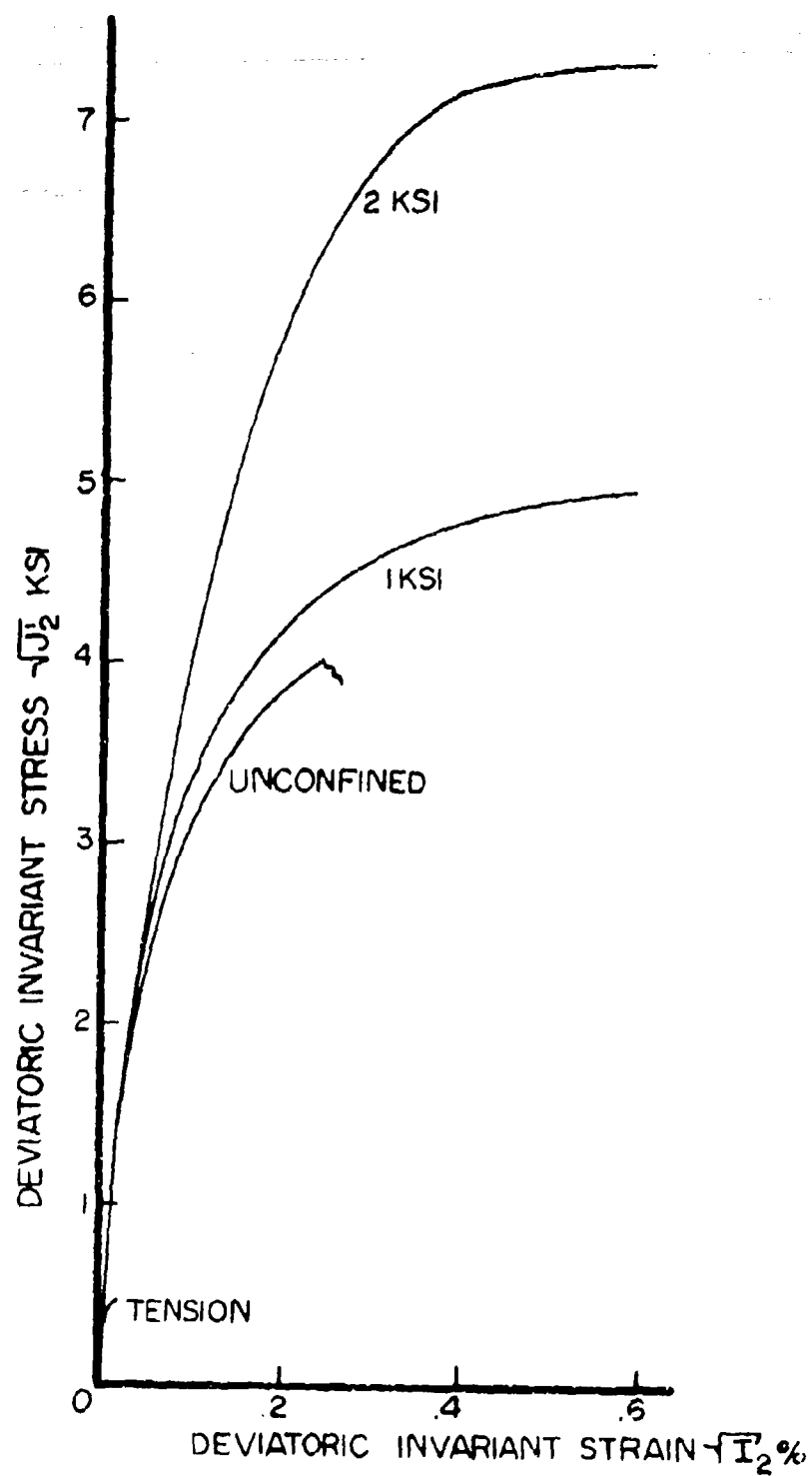


Figure 16. Deviatoric stress-strain curves for constant confining pressure tests.

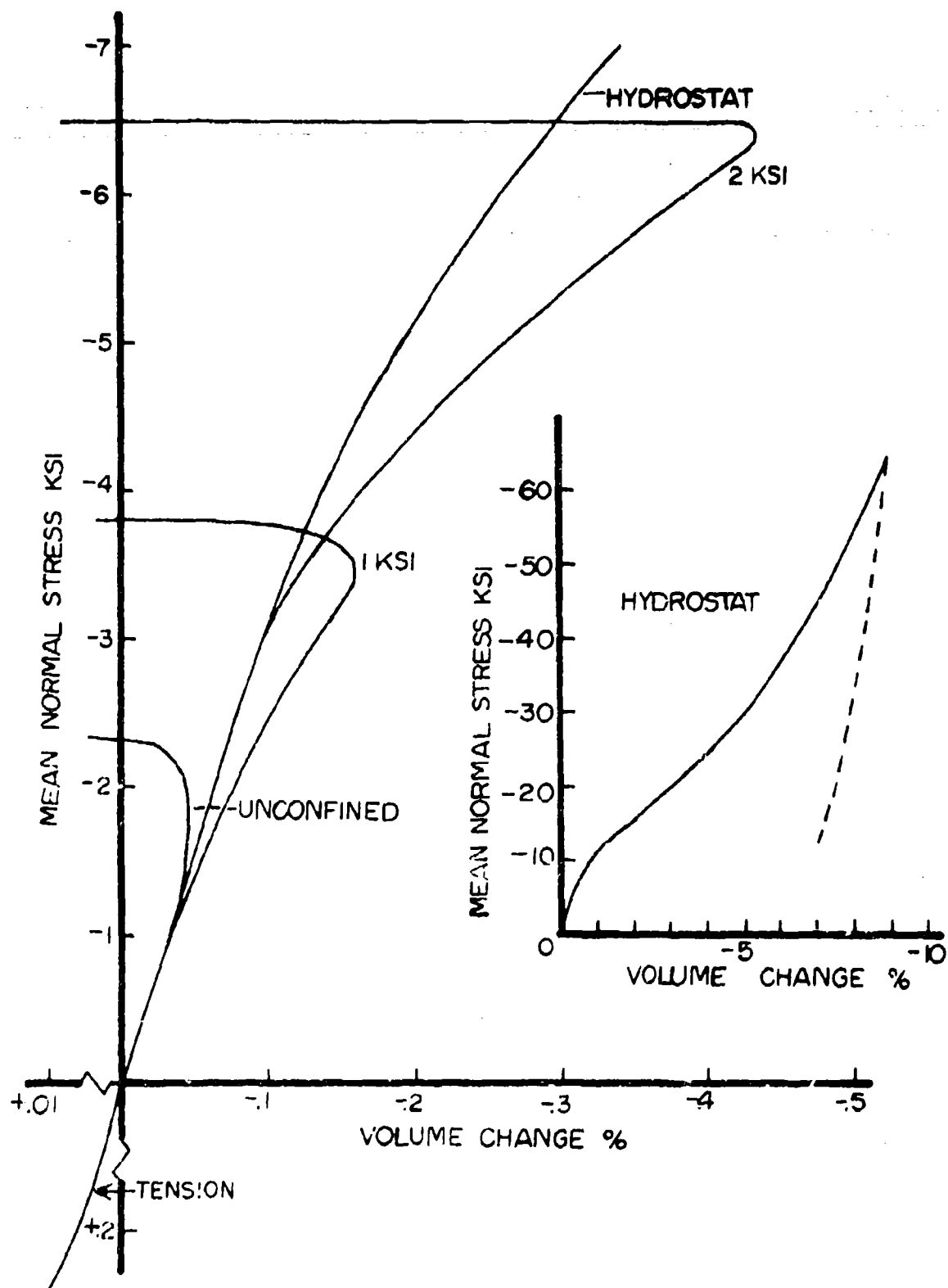


Figure 17. Dilatation stress-strain curves for constant confining pressure tests.

slightly with pressure.

In the dilatational plane, Figure 17, the mean normal stress, p_m , is plotted versus volume change, $\Delta V/V_0$, defined as

$$p_m = 1/3 (\sigma_1 + \sigma_2 + \sigma_3) \quad (3)$$

$$\Delta V/V_0 = \epsilon_1 + \epsilon_2 + \epsilon_3 \quad (4)$$

The slope of this curve is equal to the apparent bulk modulus, B . Pure hydrostatic loading shows that the hydrostat tends to stiffen at very low pressures, up to 2-3 ksi, then the concrete structure begins to collapse and the hydrostat softens until about 25 ksi where it again stiffens (as shown by the insert). Several pure hydrostatic load-unload tests, which were conducted to determine at what pressure permanent compaction begins, indicated that measurable permanent compaction begins at about 6 ksi pressure.

Unconfined and constant confining pressure tests show dilation begins at some load below maximum stress; however, before large dilation begins, compaction in excess of the hydrostatic compaction occurs. This compaction is believed due to collapsing of the structure caused by the shear stress, and has been observed on other porous materials (Ref. 28).

In tension, bulking is observed, with the volume change increasing toward greater volume increase with increased load. To simulate the bulking in tension and dilation in compression the apparent Poisson ratio would have to vary from negative to greater than 0.5. These curves show that the assumption of a linear elastic material with a fixed Poisson ratio is not reasonable even for the low stresses shown here.

Variable Load Path Tests: In addition to the unconfined and constant confining pressure tests, other load path tests were performed, including extension,

constant shear stress (proportional to $\sqrt{J_2'}$), constant mean stress (proportional to J_1), and uniaxial strain.

The load paths for these tests are shown in Figure 18, where stress difference, $\sigma_a - \sigma_t$, is plotted versus the transverse stress σ_t . Each curve represents a single test. For the constant J_1 , $\sqrt{J_2'}$ and uniaxial strain tests, all three stresses are compression, while for the extension tests the transverse stresses are compression while the axial stress may be compression or tension.

Figure 19 shows the stress difference plotted versus axial shortening and transverse extension strains; that is, the strains during the hydrostatic loading part of the test have not been included. The strains during the hydrostatic loading can be obtained from Figure 17 by assuming axial and transverse strains to be equal and thus given by 1/3 of the volume change. Figure 20 shows the tests plotted in the mean normal stress-volume change plane, and Figure 21 shows the tests plotted in the deviatoric invariant stress-strain plane.

Failure Envelope: The magnitude of the deviatoric stress at the brittle maximum stress or at the ductile yield, which is defined as the stress at 1% axial strain, is plotted versus mean normal stress in Figure 22. A variety of load paths are shown, including triaxial compression and extension, constant mean normal stress, constant deviatoric invariant stress and uniaxial strain. The triaxial compression tests form an upper bound while the two extension tests suggest that triaxial extension forms a lower bound. The uniaxial strain load path yields at a point between the triaxial compression and extension bounds. The 'failure envelope' suggests that for selected loads, such as triaxial compression, deviatoric invariant yield stress (or yield shear stress) may be related to the first stress invariant (mean normal stress),

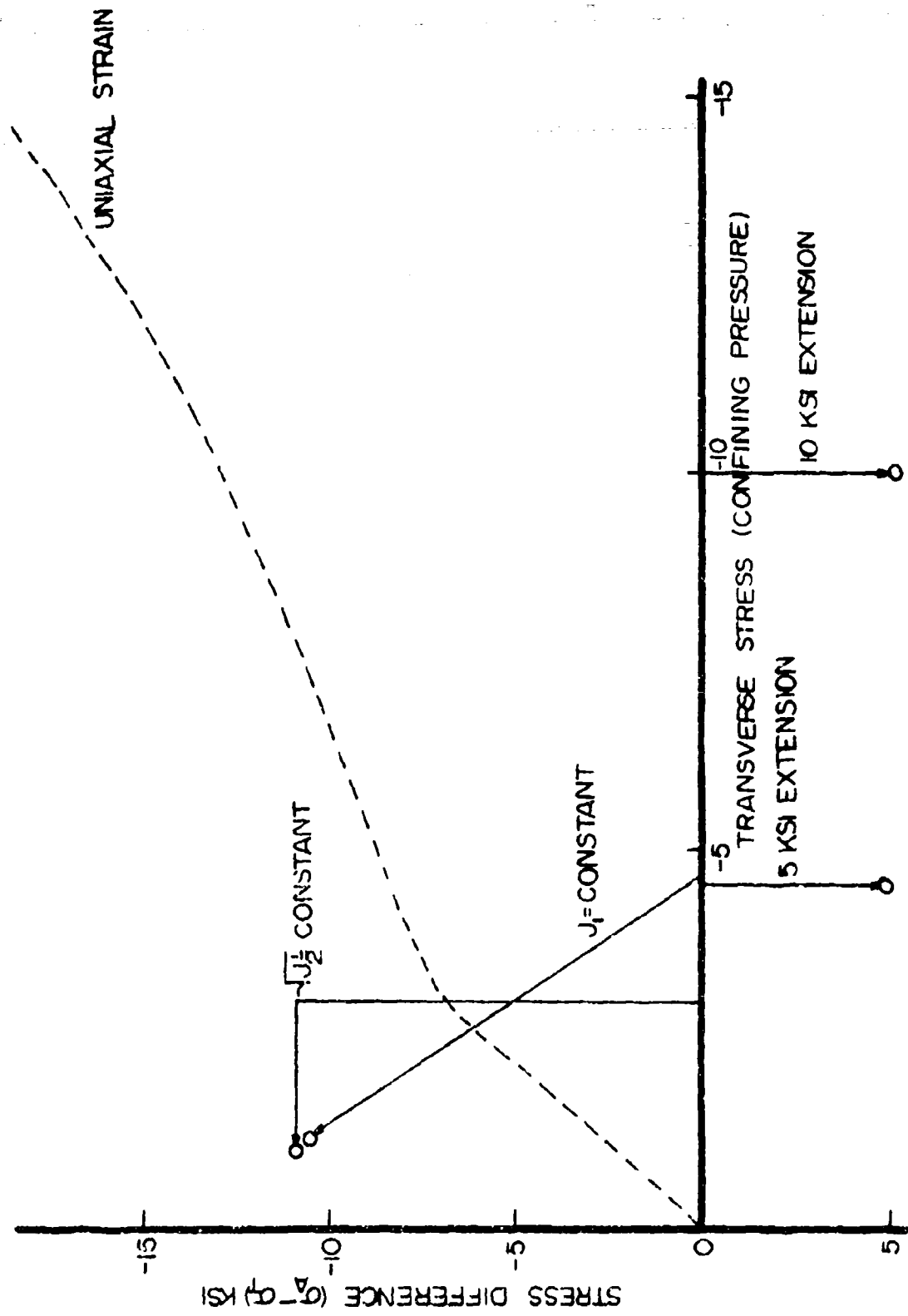


Figure 18. Stress paths for various tests.

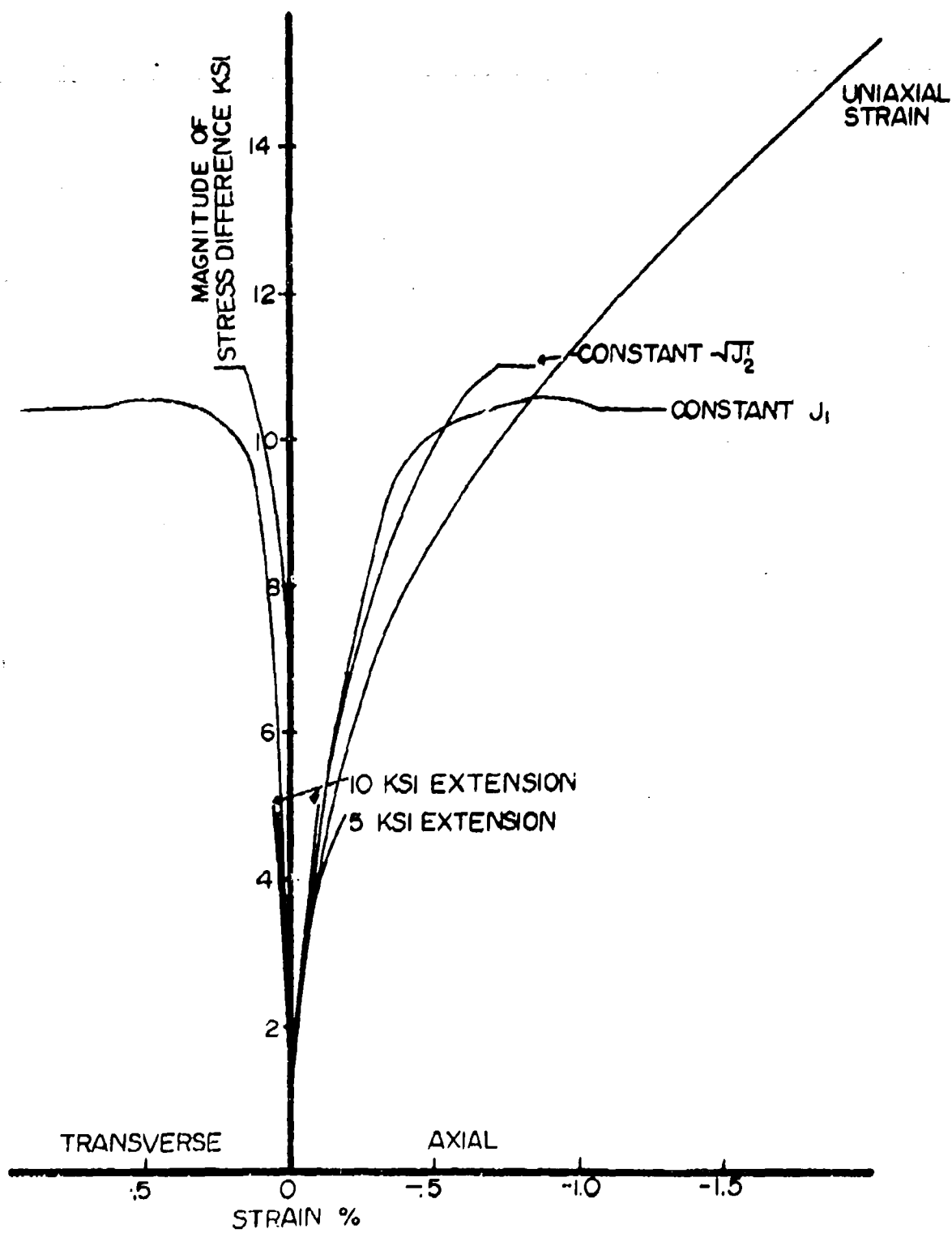


Figure 19. Principal stress-strain curves for various load paths.

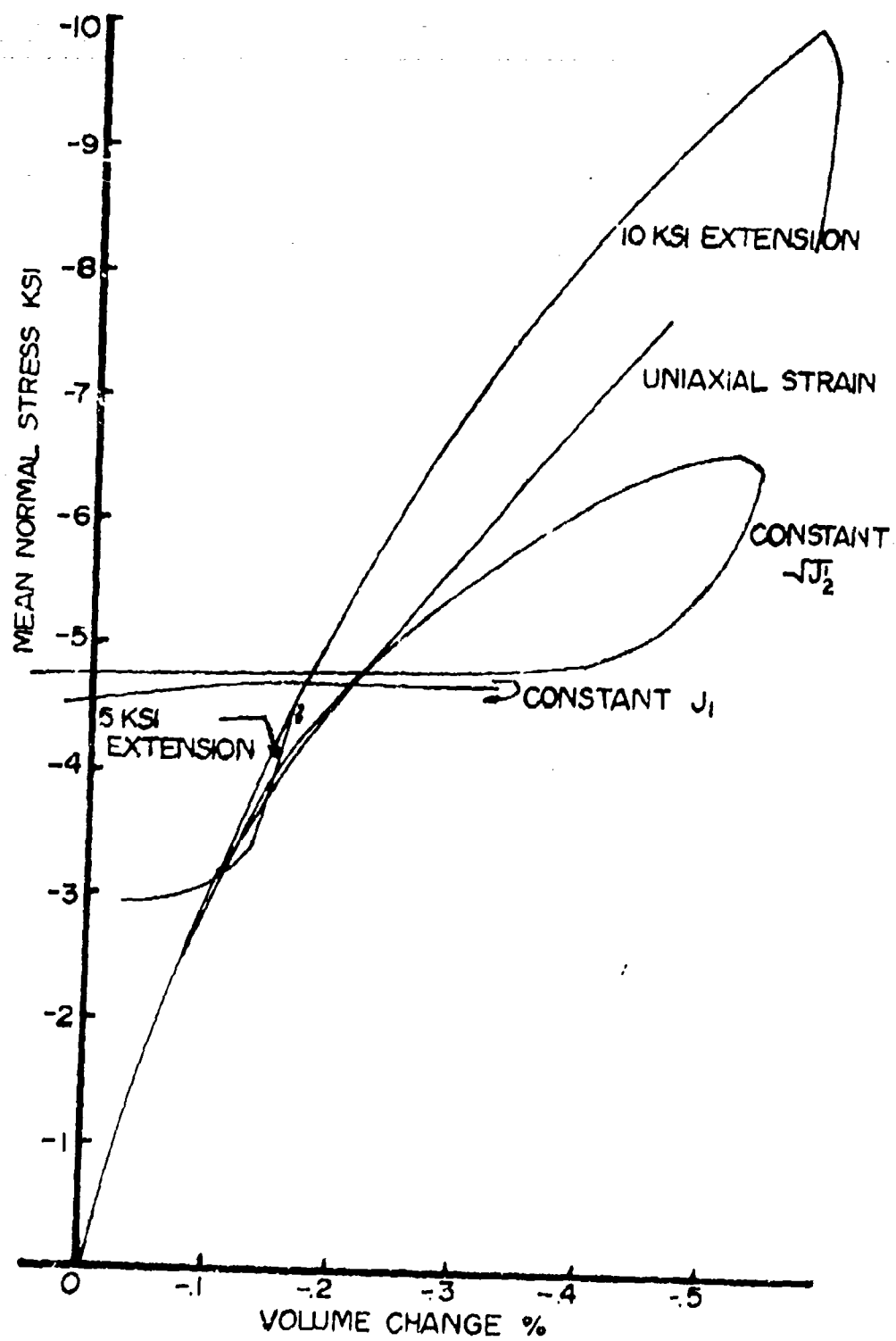


Figure 20. Dilatational stress-strain curves for various load paths.

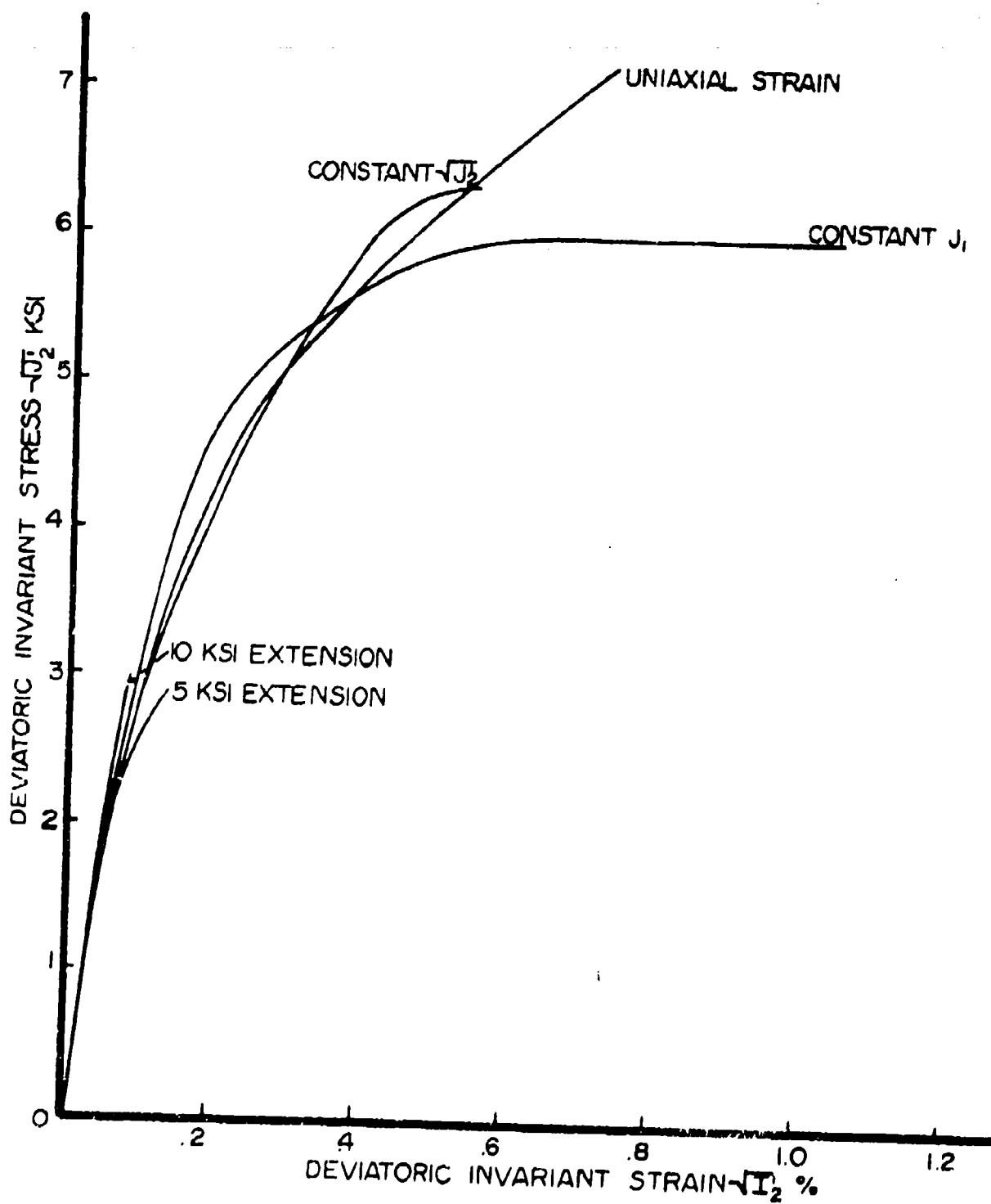


Figure 21. Deviatoric stress-strain curves for various load paths.

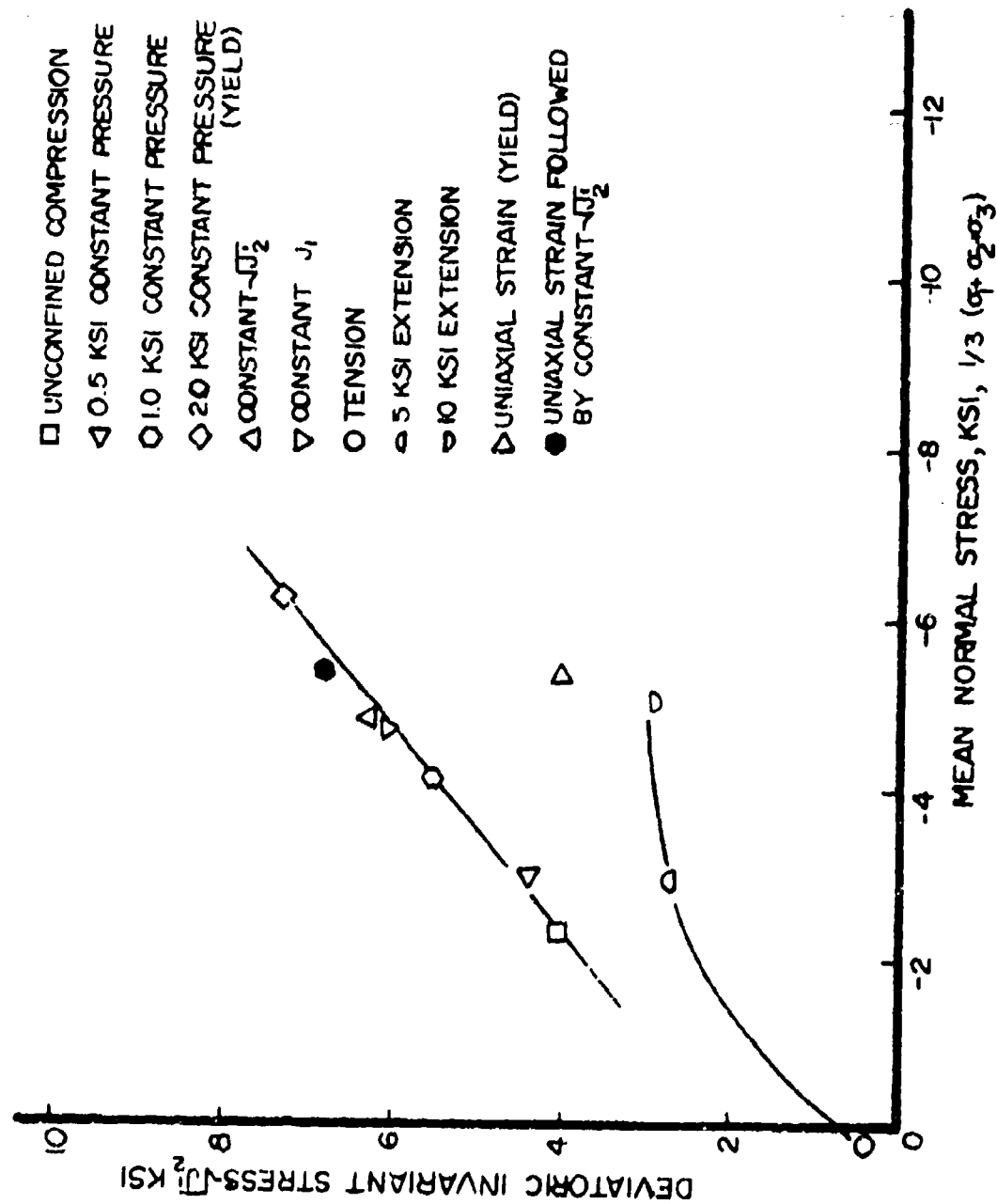


Figure 22. Maximum stress locus.

but that for more general loading, a unique relationship does not exist.

Unloading Response: Thus far, the test data show loading only, with tests generally conducted until strain gages failed or (rapid) fracture occurred. A number of tests were specifically conducted to define the unloading response, after some amount of inelastic deformation had occurred. Figures 23-26 show stress-strain curves for a number of load-unload paths. The data are plotted showing mean normal stress, $(1/3)(\sigma_1 + \sigma_2 + \sigma_3)$, versus volume change, $\epsilon_1 + \epsilon_2 + \epsilon_3$; as square root of the second deviatoric invariant of stress versus strain; and as stress difference, $|\sigma_1 - \sigma_3|$, versus strains, ϵ_1 and ϵ_3 . Here σ_1 , ϵ_1 refer to axial direction and $\sigma_2 = \sigma_3$ and $\epsilon_2 = \epsilon_3$ refer to transverse direction.

The unloading curves show that unloading paths do not follow an 'elastic' unload path, but instead suggest both an anisotropic hardening that causes yielding during unloading and strain induced anisotropy of the elastic constants. The former is suggested by the complex unload paths as the axial compression is removed at constant confining pressure, while the latter is suggested by the shape of the unload 'hydrostat' as the confining pressure is removed.

Reloading follows nearly the previous unload path if the unload-reload occurs under nearly the same load ratio. If reload occurs for a grossly different load ratio, as for example compression under constant confining pressure followed by compression without confining pressure, then the reload path does not follow the previous unload path.

Fracture: Fracture patterns are shown in the photographs of Figure 27. The photographs represent specimens taken either to brittle fracture (well beyond maximum stress) or to large ductile strains, which generally produced macro shear failures. Figure 27a shows specimens which were subjected to compressive

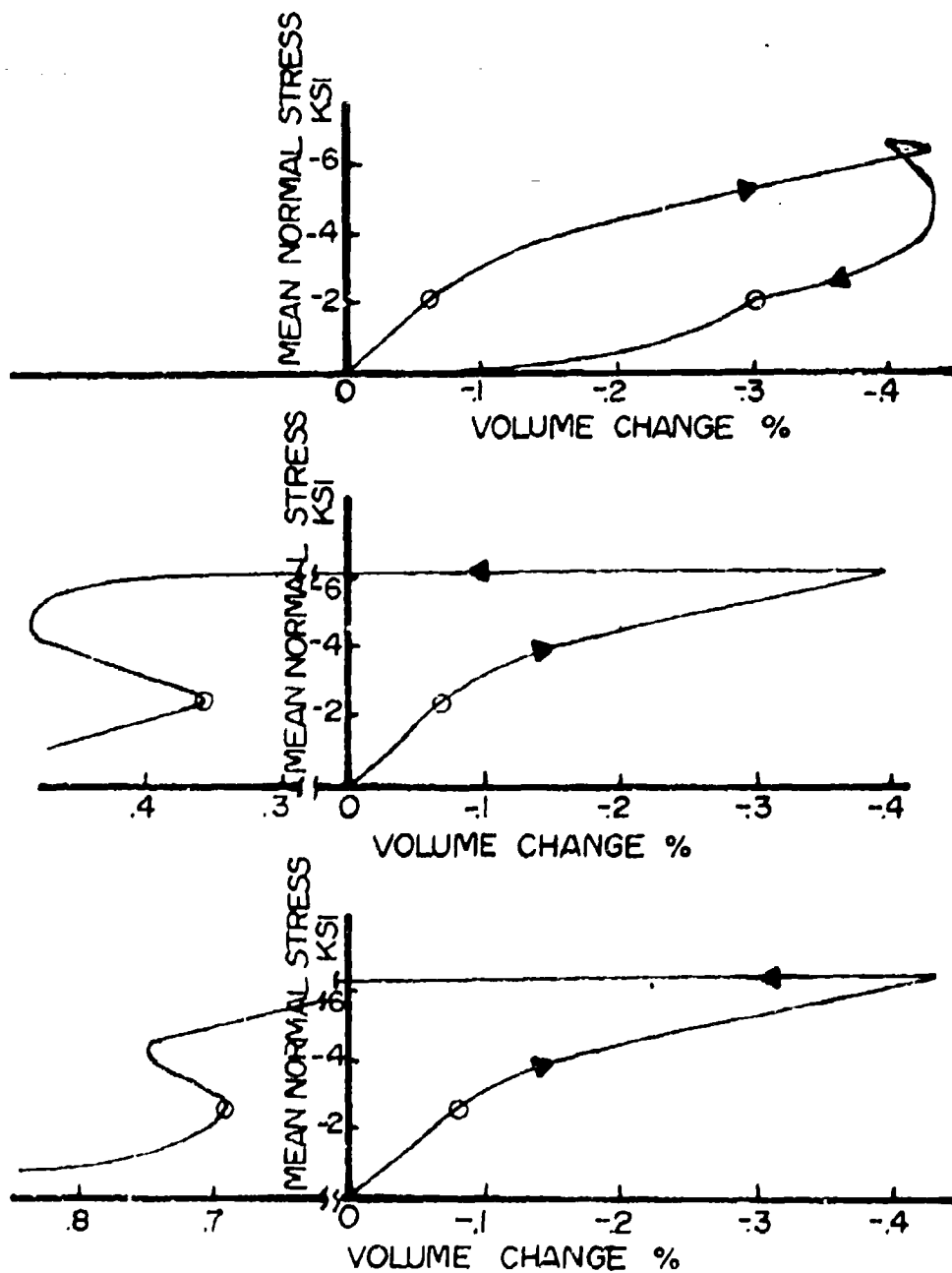


Figure 23. Triaxial compression load-unload at constant confining pressure of about 2 ksi.

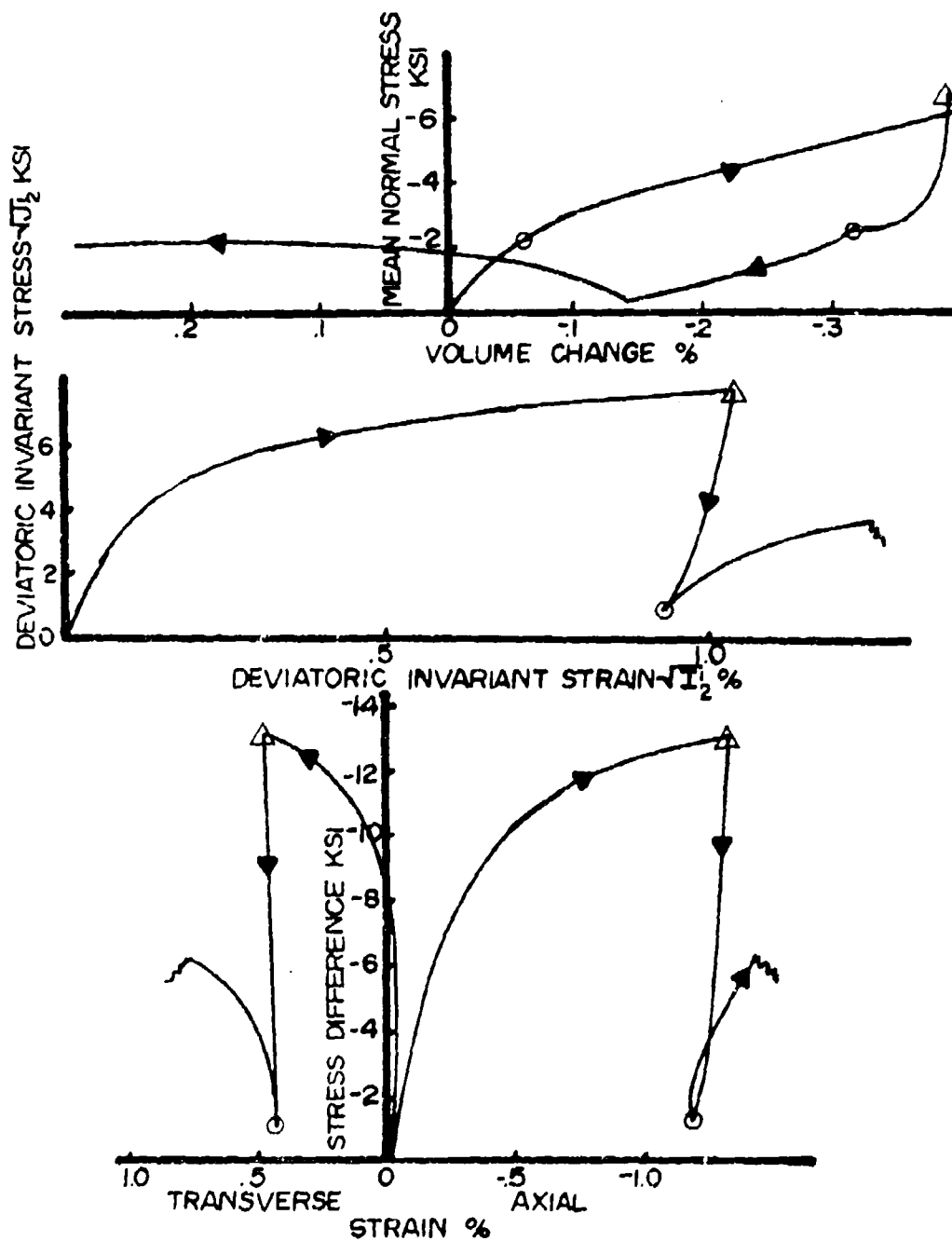


Figure 24. Triaxial compression load-unload at constant confining pressure of about 2 ksi followed by compressive reloading unconfined.

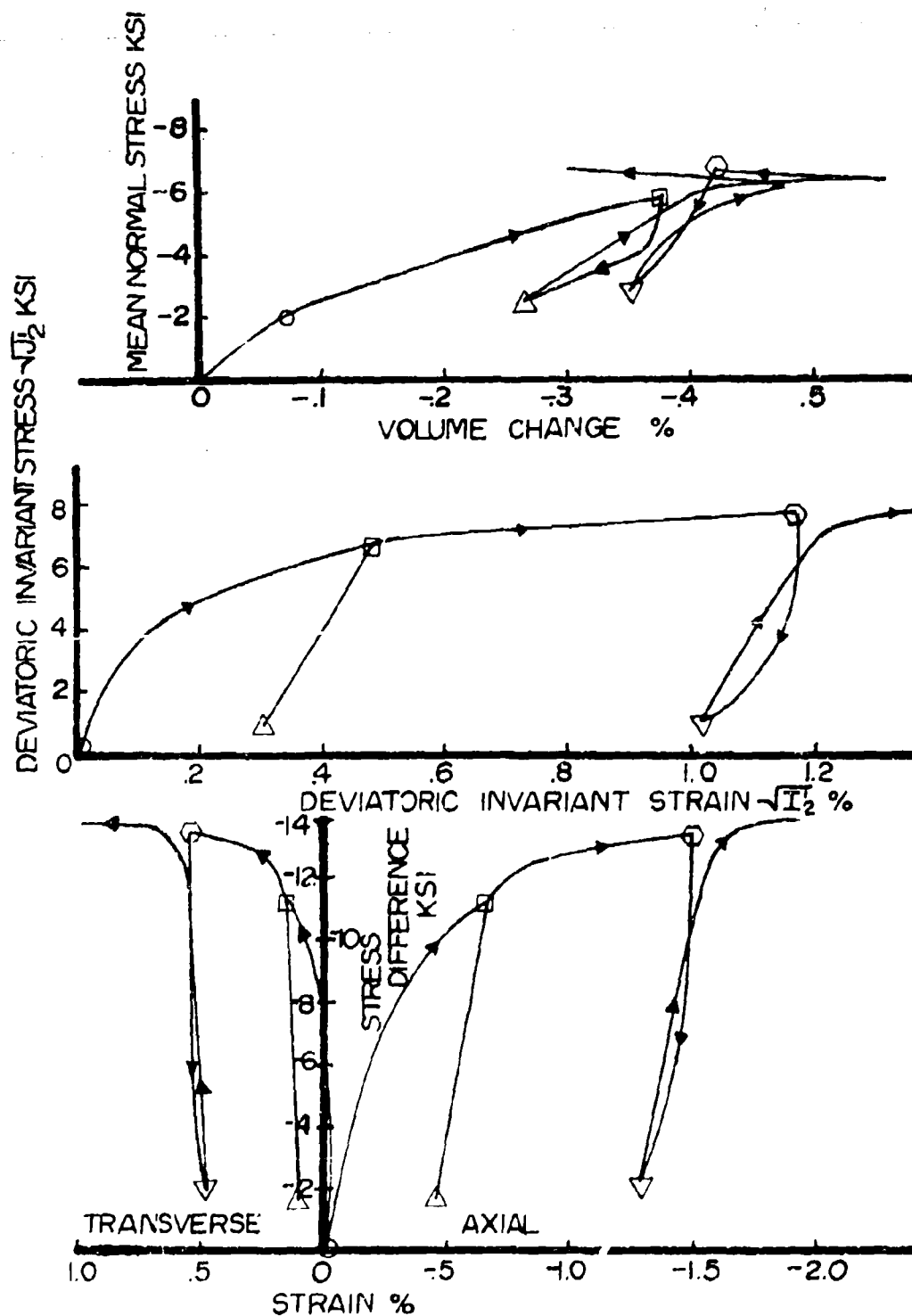


Figure 25. Triaxial compression load-unload, reload-unload, reload path at constant confining pressure of about 2 ksi.

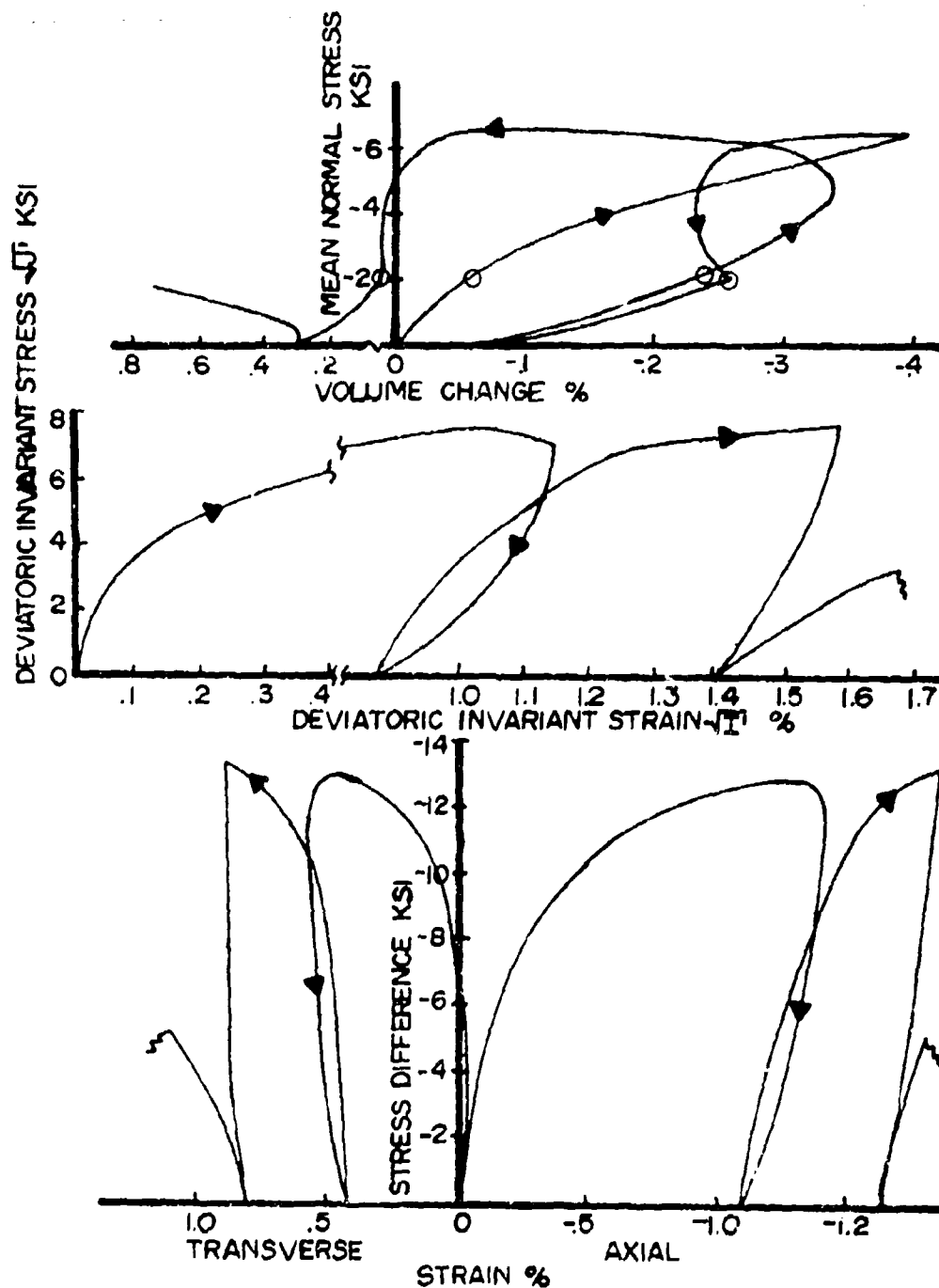


Figure 26. Triaxial compression load-unload, reload-unload path at constant confining pressure of about 2 ksi followed by compressive reloading unconfined.



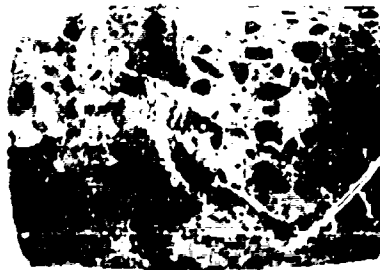
UNCONFINED

a. UNCONFINED
COMPRESSION



TRI-AXIAL
1/2 KSI C.

b. 0.5 KSI CONSTANT
PRESSURE



TRI-AXIAL
1 KSI C.P.

c. 1 KSI CONSTANT
PRESSURE



TRI-AXIAL
2 KSI C.P.

d. 2.0 KSI CONSTANT
PRESSURE



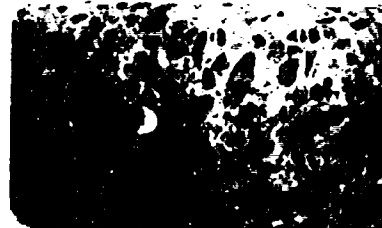
CONST J_1

e. CONSTANT MEAN
NORMAL STRESS



CONST $\sqrt{J_2}$

f. CONSTANT DEVIATORIC
INVARIANT STRESS



UNIAXIAL

g. UNIAXIAL STRAIN

Figure 27a. Photographs of tested solid cylinders (2.7 inch diameter by 6.0 inch long) loaded in compression.



TENSION

h. TENSION



EXTENSION
5 KSI

i. 5.0 KSI EXTENSION



EXTENSION
10 KSI

j. 10.0 KSI EXTENSION



k. TENSION FAILURE
SURFACE



l. 10.0 KSI EXTENSION
FAILURE SURFACE

Figure 27b. Photographs of tested solid cylinders (2.7 inch diameter by 6.0 inch long, deformed by tension or extension.

loads. The unconfined test shows brittle behavior, while 1.0 ksi confining pressure and above clearly show ductile response. The constant mean normal stress (constant J_1) and the constant deviatoric invariant stress (constant $\sqrt{J_2}$) tests were at sufficiently high enough confining pressure so that ductile behavior occurs. Under uniaxial strain loading, ductile yield is observed.

Figure 27b shows specimens which were subjected to tension or triaxial extension stress. A brittle behavior is shown, even for an extension test at 10 ksi confining pressure; however, the inserts k and l show the different failure mode between tension, where failure occurs almost totally due to fracture in the cement matrix and aggregate-cement separation, and extension at high confining pressure, where failure occurs due to fractures of the cement matrix and fracture of the aggregate. For both tension and extension tests, fracture occurred in the specimen mid-section, suggesting that the bonded end tabs were not producing an unfavorable stress concentration at the ends.

SECTION V

THEORETICAL FORMULATION OF MODEL

The features of the concrete stress-strain behavior observed in the laboratory data, particularly permanent set and hysteresis on unloading, suggest that a mathematical representation can be based on a plasticity model. This has been accomplished in that a representation of the stress-strain behavior has been developed that fits the data reasonably well. The plasticity model employed uses a strain-hardening yield surface, with two segments, and an associated flow rule.

The general characteristics of the concrete mechanical behavior are a strong dependence of stress-strain response and maximum stress (or fracture) on mean normal stress, nonlinearity, hysteresis, permanent set on unloading, and a coupling of the shear and dilatational behavior. Similar mechanical behavior has been observed in rocks and mathematical representations have been studied previously that were based on plasticity models (Refs. 23, 25, 34). The volume expansion due to shearing seen in much of the concrete data is a well-known feature for many materials and has been often termed dilatancy in the soil mechanics and rock mechanics literature. The behavior seen in the mean stress versus volume strain curves for concrete is complex, exhibiting both compaction and bulking due to shearing in different stress ranges in the same test. This can easily be seen in the comparison illustrated in Figure 28. In this figure the mean stress versus volume strain curve of a test without shearing (a hydrostatic compression loading) is compared with the same curve from a triaxial compression test. As illustrated in the figure, a compaction first occurs due to the shearing stress followed by bulking or volume expansion. This same behavior has been observed recently

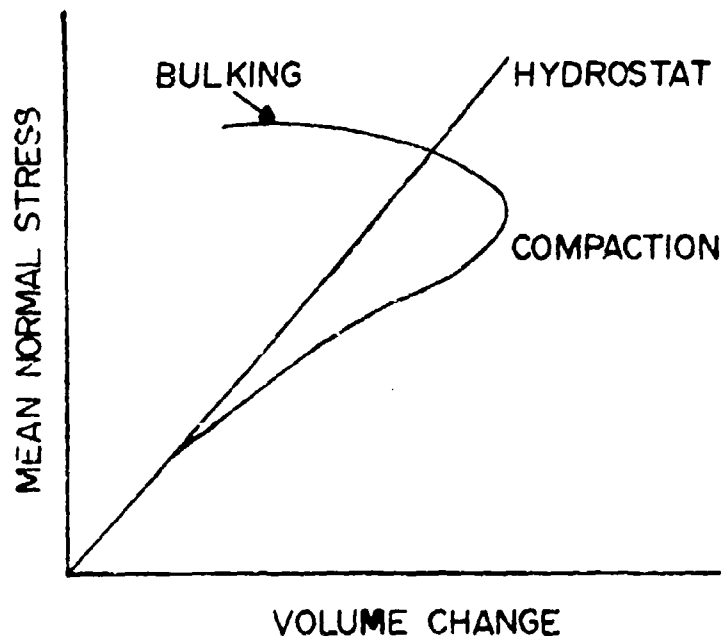


Figure 28. Illustration of compaction and bulking seen in volume behavior of porous materials.

in tests of porous rocks (Refs. 28,35). In addition, a relatively large amount of compaction can be observed in hydrostatic pressure tests at higher mean stress levels.

In the following discussion a plasticity model used to represent this mechanical behavior will be described. The model uses an associated flow law and is based on a strain hardening yield surface with two separate segments. One of the surfaces is in the form of a "cap," as used previously by Sandler, et al. (Ref. 24). The reasons for the selection of the yield surface in this form will be discussed below.

Multiple Yield-Surface Model: In the theory of plasticity it is assumed that material behavior is elastic until the applied stresses reach a critical value. Continued loading results in both elastic and irrecoverable plastic straining. The critical value of stress may be considered to be a surface in stress space and thus is referred to as a yield surface.

The yield surface to be employed for concrete is illustrated in Figure 29. Two independent segments are employed, termed F_1 and F_2 as shown. The use of two segments appears advantageous for modeling the volume plastic strain. As discussed previously, the concrete can show either compaction or bulking in the plastic (irrecoverable) volume strain. It can be shown that a yield surface with a negative slope as the segment F_1 (note that the abscissa of Figure 29 is negative to the right) will show plastic volume bulking. Conversely a yield surface with the opposite slope, such as F_2 , will show plastic volume compaction. Thus the bulking behavior is governed by the segment F_1 and the compaction by F_2 .

The theory of multiply segmented yield surfaces has been developed by Koiter (Ref. 36) and may be considered a part of the classical theory of plasticity. It should be noted that the overall yield surface does not have

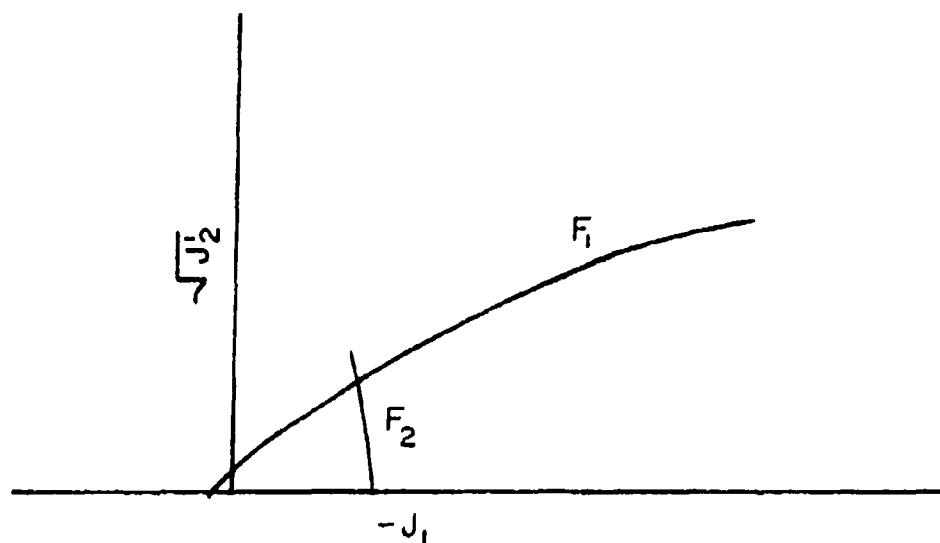


Figure 29. Illustration of two yield surfaces used for porous material plasticity model.

to be smooth. For example, as illustrated in Figure 29 the segments F_1 and F_2 are not tangent to each other at their intersection.

A number of assumptions necessarily have to be made to carry out the formulation of the model. The use of the stress invariants $\sqrt{J_2}$ and J_1 to describe the yield surface is a simplifying assumption that is inaccurate in fine detail. This assumption will be discussed further in Section VI. It is also assumed that tension stress states can be handled similarly to compression, with the decrease in $\sqrt{J_2}$ as illustrated in Figure 29 accounting for the weakness in tension. Further assumptions are that an associated flow rule and isotropic hardening can be used in the plasticity model. The use of an associated flow rule relates the plastic strain increments to the shape of the yield surface in a specific manner which will be made explicit below. It is advantageous in the sense that it greatly simplifies certain theoretical problems such as whether or not the stress-strain law is thermodynamically admissible. Isotropic hardening means that the yield surface expands uniformly as the material strain hardens. This assumption in effect insures that the unloading behavior will always be elastic, which apparently is not appropriate in detail for concrete. However isotropic hardening is at least a first step and can be considered an approximation to the real unloading behavior. In general these assumptions can be changed as detailed investigations of the various aspects of mechanical behavior are carried out.

In the theory of plasticity for small strains the strain increment can be separated into elastic and plastic components as

$$d\epsilon_{ij} = d\epsilon_{ij}^e + d\epsilon_{ij}^p \quad (5)$$

The elastic strain increment component is related to the stress increment through the elastic stress-strain law. The plastic strain increment can be expressed by the associated flow law as (Ref. 37)

$$d\epsilon_{ij}^P = \frac{\partial F}{\partial \sigma_{ij}} \lambda \quad (6)$$

where F is the yield function and λ is a constant that for strain hardening materials will contain the stress increments, thus providing a relationship between the plastic strain increments and the stress increments.

Koiter (Ref. 36) has shown that the associated flow rule for a yield surface with two segments can be written as

$$d\epsilon_{ij}^P = \frac{\partial F_1}{\partial \sigma_{ij}} \lambda_1 + \frac{\partial F_2}{\partial \sigma_{ij}} \lambda_2 \quad (7)$$

where F_1 and F_2 are the two yield surface segments. It can be seen that equation (7) is similar to (6) except that plastic strain increments can be obtained from both yield surface segments. It will be shown later that λ_1 and λ_2 will both be nonzero only if the state of stress is that defining the intersection of the two yield segments. At this point the plastic strain increment is the sum of contributions from both yield surface segments. This explains why the intersection does not have to be smooth. It is only necessary that each segment be individually smooth so that the terms

$$\frac{\partial F_1}{\partial \sigma_{ij}} \quad \text{and} \quad \frac{\partial F_2}{\partial \sigma_{ij}}$$

each exist.

The constants λ_1 and λ_2 can be defined by specifying appropriate strain hardening rules. This will be carried out in general form here and the

specific forms necessary to fit the experimental data will be examined in Section VI.

The yield surface segments are assumed to have the following forms

$$F_1 = \sqrt{J_2'} + g_1(J_1) - K_1 \quad (8)$$

$$F_2 = \frac{(\sqrt{J_2'})^2}{2} + r^2 \frac{(J_1)^2}{2} - K_2 \quad (9)$$

where $g_1(J_1)$ is a function to be determined, and r is a constant. As usual, $\sqrt{J_2'}$ is the second stress deviator invariant and J_1 is the first stress invariant given by

$$J_2' \equiv \frac{1}{2} S_{ij} S_{ij} = \frac{(\sigma_{11} - \sigma_{22})^2 + (\sigma_{22} - \sigma_{33})^2 + (\sigma_{33} - \sigma_{11})^2}{6} + \sigma_{12}^2 + \sigma_{23}^2 + \sigma_{31}^2$$

and

$$J_1 \equiv \sigma_{11} + \sigma_{22} + \sigma_{33}$$

The initial values of the constants K_1 and K_2 define the locations of the yield surface segments. When the stress state is located inside the yield surface the stress-strain response is elastic, thus $F_1 = 0$ or $F_2 = 0$ is a necessary condition for yielding.

In a strain hardening material the yield surface can move as plastic straining occurs. This can be accounted for by changing the values of the constants K_1 and K_2 as plastic straining takes place. The relationship of the change in the constants to the straining is termed the strain hardening rule. Since in the present case it is desired to have the two yield surface segments move independently it is necessary to have a hardening rule for each segment. Once the form of the yield function is established the plastic stress strain response is fully determined by the hardening rule employed.

It was assumed that the movement of the segment F_1 depended on the plastic shearing strain and that the movement of F_2 depended on the plastic compaction strain. Specifically the hardening rules were taken as

$$d\sqrt{I_2}^P = h_1 dK_1 \quad (10)$$

and

$$d\epsilon_{VC}^P = h_2 dK_2 \quad (11)$$

where $d\sqrt{I_2}^P$ is the second invariant of the plastic strain increment tensor, $d\epsilon_{VC}^P$ is the volume strain increment associated with compaction only, and h_1 and h_2 are functions to be determined by the experimental data. The total plastic volume strain has thus been divided into two parts as

$$d\epsilon_V^P = (d\epsilon_{VB}^P)_{\text{bulking}} + (d\epsilon_{VC}^P)_{\text{compaction}} \quad (12)$$

This distinction in the plastic volume strain is made for purposes of the derivation only and will not appear in the final stress strain law.

The assumption of the form of the hardening rules (equations 10 and 11) is difficult to justify until more is known about microstructural response mechanisms of concrete. The use of the deviatoric invariant in equation 10 is standard in the plasticity literature for metals (Refs. 33,37) and has been used for geologic materials (Refs. 4,23). The use of the compaction strain in equation 11 appears desirable since the yield segment F_2 should harden (expand) as compaction occurs in both hydrostatic and nonhydrostatic loadings. However, it should be recognized that these are plausibility arguments. While the appropriateness of the assumptions of equations 10 and 11 can in part be examined by the fit between the resulting model and experimental data, the full validity of extrapolation to new stress conditions is not established.

The constants λ_1 and λ_2 are determined by substituting the hardening rules into the appropriate equations as follows. Since plastic shearing strains are obtained from loading on both yield segments, the plastic strain obtained from both segments (equation 7) should be substituted in equation 10. This substitution is straightforward but lengthy and is given in Appendix C. The result is

$$\frac{\partial F_1}{\partial \sqrt{J_2}} \lambda_1 + \frac{\partial F_2}{\partial \sqrt{J_2}} \lambda_2 = 2h_1 dK_1 \quad (13)$$

The compaction plastic volume strain is obtained only from the F_2 yield surface segment, provided that the slopes of the segments F_1 and F_2 are restricted appropriately. With this implicit restriction, the strain from the F_2 segment which is given as

$$(d\epsilon_{ij}^p)_{F_2} = \frac{\partial F_2}{\partial \sigma_{ij}} \lambda_2 \quad (14)$$

should be substituted into the hardening rule for compaction, equation 11. The result of this substitution gives

$$\frac{\partial F_2}{\partial J_1} \lambda_2 = 1/3 h_2 dK_2 \quad (15)$$

To ensure that plastic straining occurs only when the material is yielding, it is necessary to define the constants λ_1 and λ_2 as follows:

$$\lambda_1 = \begin{cases} \lambda_1 & \text{if } \begin{cases} F_1 = 0 \\ dF_1 > 0 \end{cases} \\ 0 & \text{if } \begin{cases} F_1 < 0 \\ \text{or } dF_1 \leq 0 \end{cases} \end{cases} \quad (16)$$

and

$$\lambda_2 = \begin{cases} \lambda_2 & \text{if } \begin{cases} F_2 = 0 \\ dF_2 > 0 \end{cases} \\ 0 & \text{if } \begin{cases} F_2 < 0 \\ \text{or } dF_2 \leq 0 \end{cases} \end{cases} \quad (17)$$

Equation 15 can then be solved for λ_2 , subject to equation 17 above, as

$$\lambda_2 = \frac{1/3 h_2 dK_2}{\frac{\partial F_2}{\partial J_1}} \quad (18)$$

and equation 13 can be solved as

$$\lambda_1 = \frac{1}{\frac{\partial F_1}{\partial \sqrt{J_2}}} (2h_1 dK_1 - \frac{\partial F_2}{\partial \sqrt{J_2}} \lambda_2) \quad (19)$$

It should be noted that the yield surface segments do not move inward during any loading. This observation follows directly from the hardening rules assumed in equations 10 and 11, and the assumption of isotropic hardening. It is assumed that the plastic deviatoric strain invariant and the plastic compaction strain are non-decreasing in absolute magnitude. Thus the functions h_1 and h_2 are restricted to not changing sign during yielding.

The above equations complete the basic derivation of the two yield surface segment plasticity model. In Section VI the necessary functions and constants will be fitted to experimental data on concrete and the basic utility

of the model will be demonstrated.

Derivation of Strain Increment as Independent Variable: The usual plasticity model formulation as shown above considers the strain increments resulting from a stress increment loading, so that the stress increments can be considered to be the independent variables. In continuum analysis codes, particularly those using the finite-element formulation, it is often necessary to have the incremental stress-strain relationship in the inverse form so that the strain increments are the independent variables. This reformulation can be readily carried out without introducing any changes in the assumptions of the material behavior. This reformulation is carried out as follows:

Consider the usual separation of strain increments into elastic and plastic components stated previously as

$$d\epsilon_{ij} = d\epsilon_{ij}^e + d\epsilon_{ij}^p \quad (5)$$

The elastic stress-strain law can be written as

$$d\sigma_{ij} = L d\epsilon_{kk}^e \delta_{ij} + 2G d\epsilon_{ij}^e \quad (20)$$

where the symbol L is used here for the Lamé constant

$$L = \frac{\nu E}{(1+\nu)(1-2\nu)}$$

In index notation this can be written as

$$d\sigma_{ij} = C_{ijkl} d\epsilon_{kl}^e \quad (21)$$

where C is the elastic coefficient matrix. Substituting equation 5 into 21 gives

$$d\sigma_{ij} = C_{ijkl} d\epsilon_{kl}^e - C_{ijkl} d\epsilon_{kl}^p \quad (22)$$

Using the flow rule developed for the two segment yield surface

$$d\epsilon_{k1}^p = \frac{\partial F_1}{\partial \sigma_{k1}} \lambda_1 + \frac{\partial F_2}{\partial \sigma_{k1}} \lambda_2 \quad (7)$$

then equation 22 can be written as

$$d\sigma_{ij} = C_{ijkl} d\epsilon_{kl} - C_{ijkl} \left(\frac{\partial F_1}{\partial \sigma_{kl}} \lambda_1 + \frac{\partial F_2}{\partial \sigma_{kl}} \lambda_2 \right) \quad (23)$$

The hardening rules were expressed previously as

$$d\sqrt{I_2}^p = h_1 dF_1 = h_1 \frac{\partial F_1}{\partial \sigma_{ij}} d\sigma_{ij} \quad (10)$$

$$d\epsilon_{vc}^p = h_2 dF_2 = h_2 \frac{\partial F_2}{\partial \sigma_{ij}} d\sigma_{ij} \quad (11)$$

where $d\epsilon_{vc}^p$ is the volumetric compaction from the F_2 yield surface. The equations previously developed for λ_1 and λ_2 were

$$\frac{\partial F_1}{\partial \sqrt{J_2}^1} \lambda_1 + \frac{\partial F_2}{\partial \sqrt{J_2}^1} \lambda_2 = 2 h_1 \frac{\partial F_1}{\partial \sigma_{ij}} d\sigma_{ij} \quad (13)$$

$$\frac{\partial F_2}{\partial J_1} \lambda_2 = 1/3 h_2 \frac{\partial F_2}{\partial \sigma_{ij}} d\sigma_{ij} \quad (15)$$

Substituting equation 23 for $d\sigma_{ij}$ into the right hand sides of equations 13 and 15 above gives

$$\frac{\partial F_1}{\partial \sqrt{J_2}^1} \lambda_1 + \frac{\partial F_2}{\partial \sqrt{J_2}^1} \lambda_2 = 2 h_1 \frac{\partial F_1}{\partial \sigma_{ij}} \left\{ C_{ijkl} d\epsilon_{kl} - C_{ijkl} \left(\frac{\partial F_1}{\partial \sigma_{kl}} \lambda_1 + \frac{\partial F_2}{\partial \sigma_{kl}} \lambda_2 \right) \right\} \quad (24)$$

and

$$\frac{\partial F_2}{\partial J_1} \lambda_2 = \frac{h_2}{3} \frac{\partial F_2}{\partial \sigma_{ij}} \left\{ C_{ijkl} d\epsilon_{kl} - C_{ijkl} \left(\frac{\partial F_1}{\partial \sigma_{kl}} \lambda_1 + \frac{\partial F_2}{\partial \sigma_{kl}} \lambda_2 \right) \right\} \quad (25)$$

These equations can be rearranged as

$$\begin{aligned} & \left\{ \frac{\partial F_1}{\partial \sqrt{J_2}} + 2 h_1 \frac{\partial F_1}{\partial \sigma_{ij}} C_{ijkl} \frac{\partial F_1}{\partial \sigma_{kl}} \right\} \lambda_1 + \left\{ \frac{\partial F_2}{\partial \sqrt{J_2}} + 2 h_1 \frac{\partial F_1}{\partial \sigma_{ij}} C_{ijkl} \frac{\partial F_2}{\partial \sigma_{kl}} \right\} \lambda_2 \\ & = 2 h_1 \frac{\partial F_1}{\partial \sigma_{ij}} C_{ijkl} d\epsilon_{kl} \end{aligned} \quad (26)$$

and

$$\begin{aligned} & \left\{ \frac{h_2}{3} \frac{\partial F_2}{\partial \sigma_{ij}} C_{ijkl} \frac{\partial F_1}{\partial \sigma_{kl}} \right\} \lambda_1 + \left\{ \frac{\partial F_2}{\partial J_1} + \frac{h_2}{3} \frac{\partial F_2}{\partial \sigma_{ij}} C_{ijkl} \frac{\partial F_2}{\partial \sigma_{kl}} \right\} \lambda_2 \\ & = \frac{h_2}{3} \frac{\partial F_2}{\partial \sigma_{ij}} C_{ijkl} d\epsilon_{kl} \end{aligned} \quad (27)$$

These equations can be written in shorthand notation as

$$A_1 \lambda_1 + A_2 \lambda_2 = A_3 \quad (28)$$

$$A_4 \lambda_1 + A_5 \lambda_2 = A_6 \quad (29)$$

and equations 28 and 29 solved for λ_1 and λ_2 . This gives

$$\lambda_1 = \frac{A_3 A_5 - A_2 A_6}{A_1 A_5 - A_2 A_4} \quad (30)$$

$$\lambda_2 = \frac{A_1 A_6 - A_3 A_4}{A_1 A_5 - A_2 A_4} \quad (31)$$

If either $\lambda_1 = 0$ or $\lambda_2 = 0$ because loading does not occur on both yield surfaces, equations 28 and 29 should be used. Thus, if either $F_2 < 0$ or $dF_2 \leq 0$, then

$$\begin{aligned}\lambda_2 &= 0 \\ \lambda_1 &= \frac{A_3}{A_1} = \frac{A_6}{A_4}\end{aligned}\tag{32}$$

Likewise, if either $F_1 < 0$ or $dF_1 \leq 0$, then

$$\begin{aligned}\lambda_1 &= 0 \\ \lambda_2 &= \frac{A_3}{A_2} = \frac{A_6}{A_5}\end{aligned}\tag{33}$$

The final stress-strain law is given in equation 23 as

$$d\sigma_{ij} = C_{ijkl} d\epsilon_{kl} - C_{ijkl} \left(\frac{\partial F_1}{\partial \sigma_{kl}} \lambda_1 + \frac{\partial F_2}{\partial \sigma_{kl}} \lambda_2 \right)\tag{23}$$

where λ_1 and λ_2 are given as equations 30, 31 or 32, 33 above.

SECTION VI

COMPARISON OF MODEL AND EXPERIMENT

In this section the functions in the previous equations will be specified to fit the experimental data on concrete. Stress is expressed in units of psi with the convention of tensile stresses taken as positive.

The elastic behavior of the concrete was taken as linear in both shear and bulk with constants

$$\begin{aligned} G &= 2.0 \times 10^6 \text{ psi} && \text{shear modulus} \\ B &= 3.0 \times 10^6 \text{ psi} && \text{bulk modulus} \end{aligned} \quad (34)$$

The yield functions were taken as

$$F_1 = \sqrt{J_2} - 1000. \left[12.2 - 11 \exp(J_1/40000.) \right] \left[1. - \exp((J_1 - 800.)/700.) \right] - K_1 \quad (35)$$

$$F_2 = \frac{(\sqrt{J_2})^2}{2} + 2 J_1^2 - K_2 \quad (36)$$

The yield surface segment F_1 is taken as the locus of points where deviation from the initial elastic and approximately linear behavior in shear occurs. This definition is somewhat arbitrary as the point of deviation from linearity depends on subjective judgment and experimental accuracy. However, the problem is not serious if the hardening rule parameters are specified accordingly.

The segment F_1 is based on the tension, unconfined compression, and triaxial compression test results. As a smooth transition from tension to compression is assumed, no specific provision for a tension cutoff is necessary.

The yield surface segment F_2 is defined in an arbitrary manner. That is, it was taken as being small with respect to tension and compression failure stresses and thus not well defined by the experimental data. The hardening

rule was adjusted, however, so that the combined effect of yield surface and hardening rule did match experimental data. A comparison of equation 36 with equation 9 shows that the ratio of the radii of the F_2 ellipse has been taken as 2. Trial runs showed that the resulting fit was not sensitive to this parameter, thus the value of 2 is somewhat arbitrary. The constants K_1 and K_2 change as strain hardening occurs according to strain hardening rules given below and have initial values

$$\begin{aligned} K_1 &= 0.0 \text{ psi} \\ K_2 &= 5 \times 10^7 \text{ (psi)}^2 \end{aligned} \quad (37)$$

The hardening rules are given as

$$d\sqrt{I_2}^P = h_1 dF_1 = h_1 dK_1 \quad \text{if } dF_1 > 0 \quad (38)$$

with

$$h_1 = 10^{-6} \left\{ \frac{1 - 100 [1 - \exp(120 \sqrt{I_2}^P / (1 - 10^{-4} J_1))]}{2 - 7 \times 10^{-5} J_1} \right\} \quad (39)$$

and

$$d\epsilon_{vc}^P = h_2 dF_2 = h_2 dK_2 \quad \text{if } dF_2 > 0 \quad (40)$$

with

$$\begin{aligned} h_2 = & \left\{ -2.4 \times 10^{-14} \sqrt{J_2}^P [1 - \exp(-\sqrt{J_2}^P / 4000)] [\exp(-\sqrt{J_2}^P / (8 \times 10^{15}))] \right. \\ & \left. - 0.702 \times 10^{-11} [1 - \exp(J_1^3 / (1.35 \times 10^{13}))] [\exp(J_1 / (6 \times 10^4))] \right\} \end{aligned} \quad (41)$$

As discussed in the previous section the constants K_1 and K_2 defining the yield surface are changed as strain hardening occurs and are defined so as to be nondecreasing. Thus, each yield surface segment moves away from the origin as it is loaded. During loading on F_1 (i.e., $F_1 = 0$ and $dF_1 > 0$) $dF_1 = dK_1$ and during loading on F_2 (i.e., $F_2 = 0$ and $dF_2 > 0$) $dF_2 = dK_2$. Otherwise,

$dK_1 = dK_2 = 0$. Unloading from and reloading back to the yield surface is thus assumed to be elastic. Changes in stress from tension to compression are defined by the above procedure, i.e., no special or additional assumptions need be made.

The stress-strain behavior based on these equations has been computed and compared with the laboratory data in Figures 30 through 41. Figure 30 shows a hydrostatic loading comparison. In this figure the nonlinearity of the curve above a pressure of about 6,000 psi is caused by compaction.

A comparison with unconfined tension, unconfined compression, and triaxial compression is shown in Figures 31 and 32. The shearing curves in Figure 31 demonstrate the nonlinearity due to yielding. The dilatational response clearly shows compaction and bulking in both the model and experimental data.

Other comparisons are shown in Figures 33 through 41. Figures 33 and 34 show the comparisons for the tests in which $\sqrt{J_2}$ and J_1 are held constant over part of the loading. Figures 35 and 36 show comparisons for an extension test at a confining pressure of approximately 5 ksi. Figures 37, 38, and 39 give the one-dimensional strain test comparison. Figures 40 and 41 show load and unload triaxial compression test results.

In general, the comparison between model and experiment is reasonably good and the qualitative features are well represented in the model. The one-dimensional strain test comparisons are somewhat poorer than the other tests. This can largely be ascribed to the high mean stress levels in this test. The mean stress levels in the triaxial compression tests were lower and the model parameters were based primarily on these tests. Thus, the model had to be extrapolated significantly for the one-dimensional strain test. It should also be noted that the variations in the experimental data in the one-dimensional strain test were significant. For this reason the

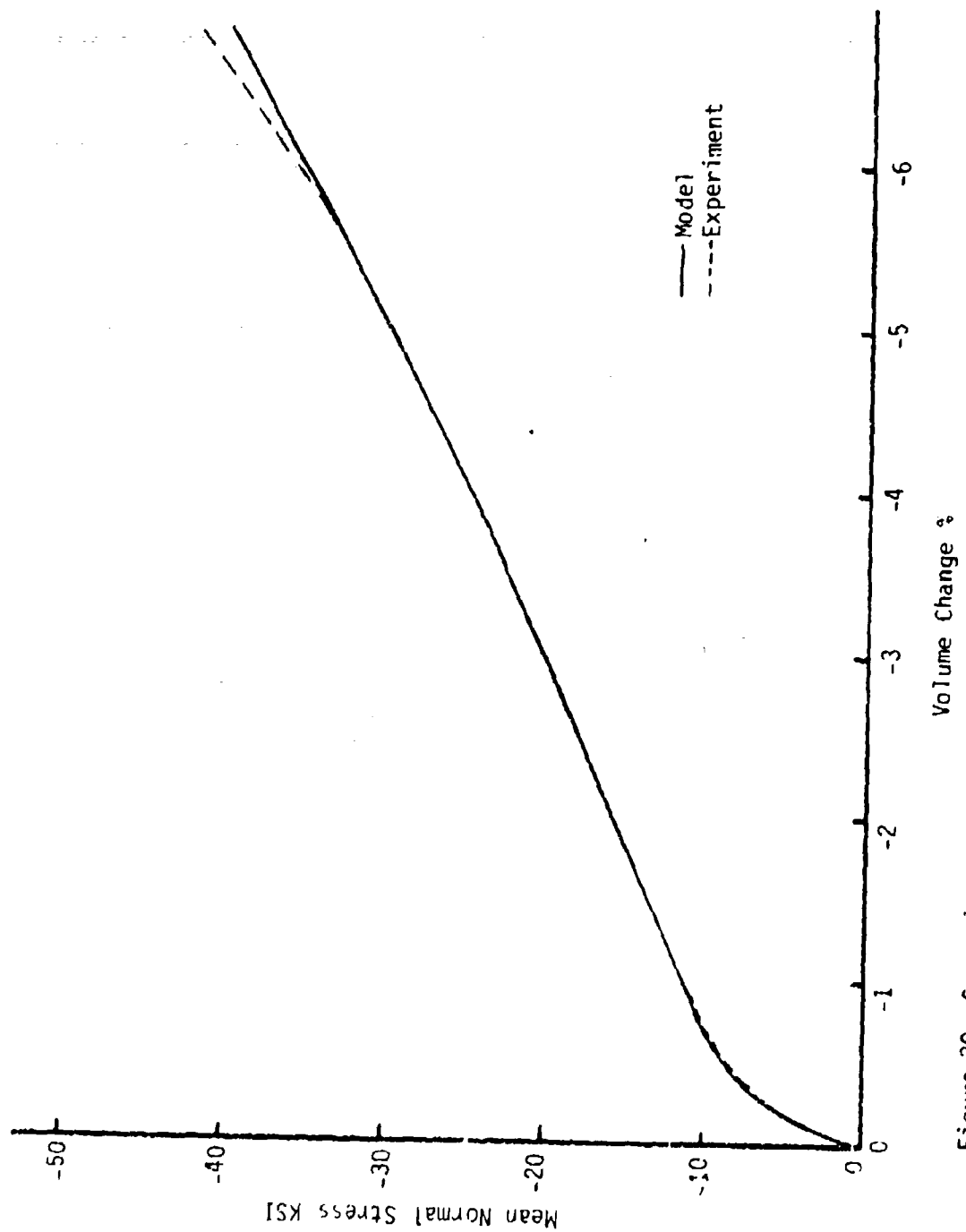


Figure 30. Comparison of model and experimental dilatational curves for concrete in hydrostatic compression.

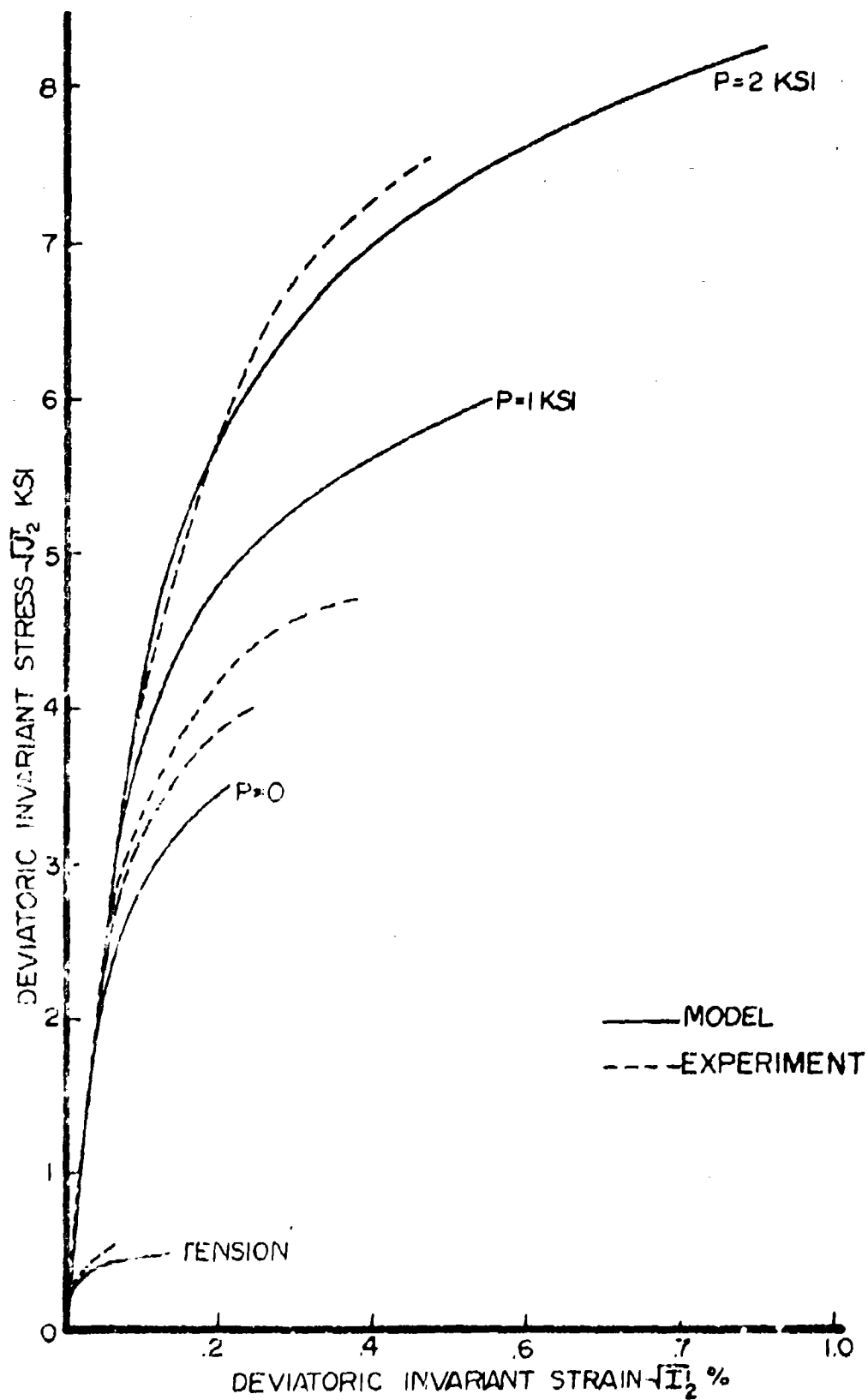


Figure 31. Comparison of model and experimental shearing stress-strain response in constant confining pressure tests.

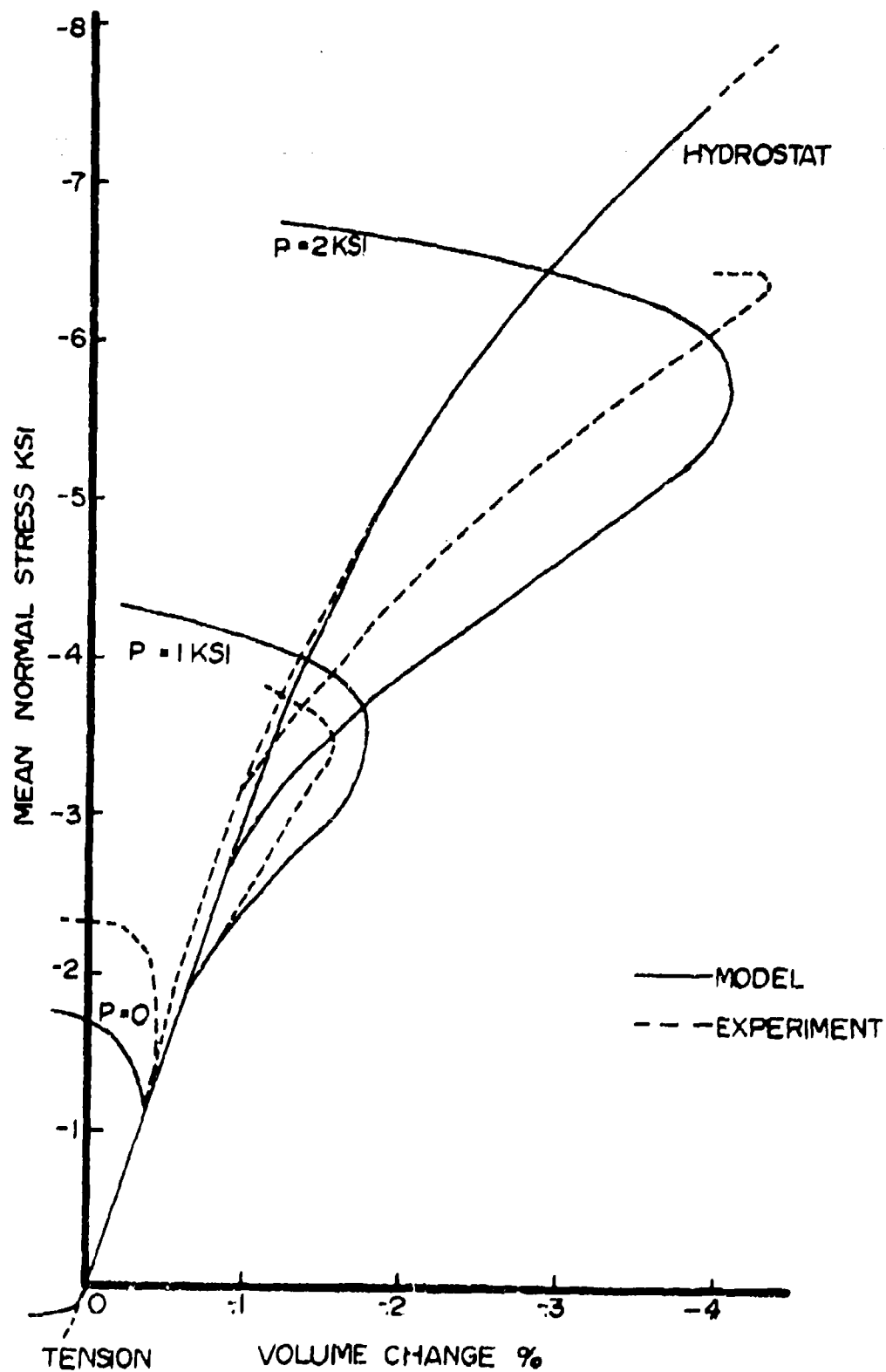


Figure 32. Comparison of model and experimental dilatational stress-strain response in constant confining pressure tests.

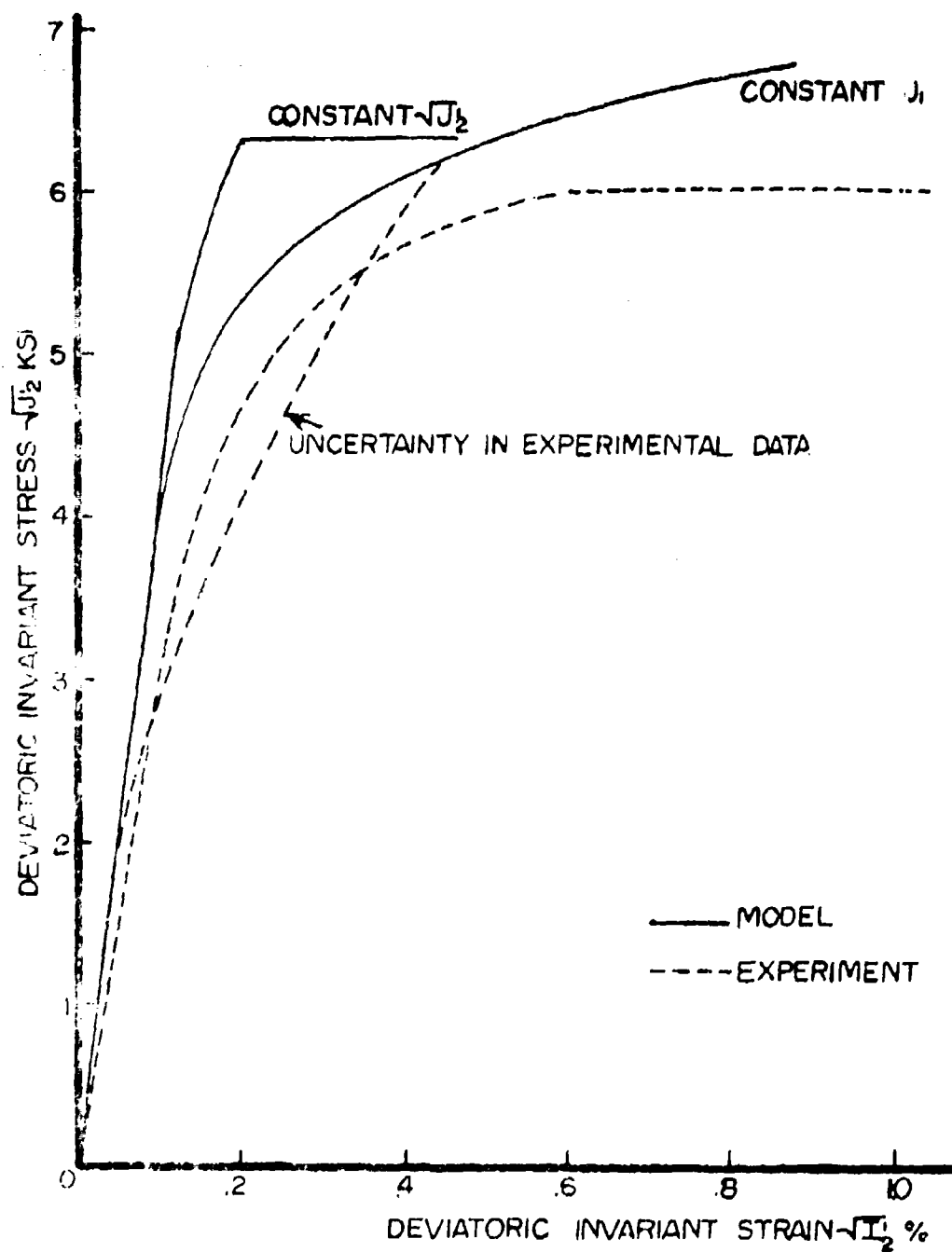


Figure 33. Comparison of model and experimental shearing stress-strain response in constant $\sqrt{J_2}$ and constant J_1 tests.

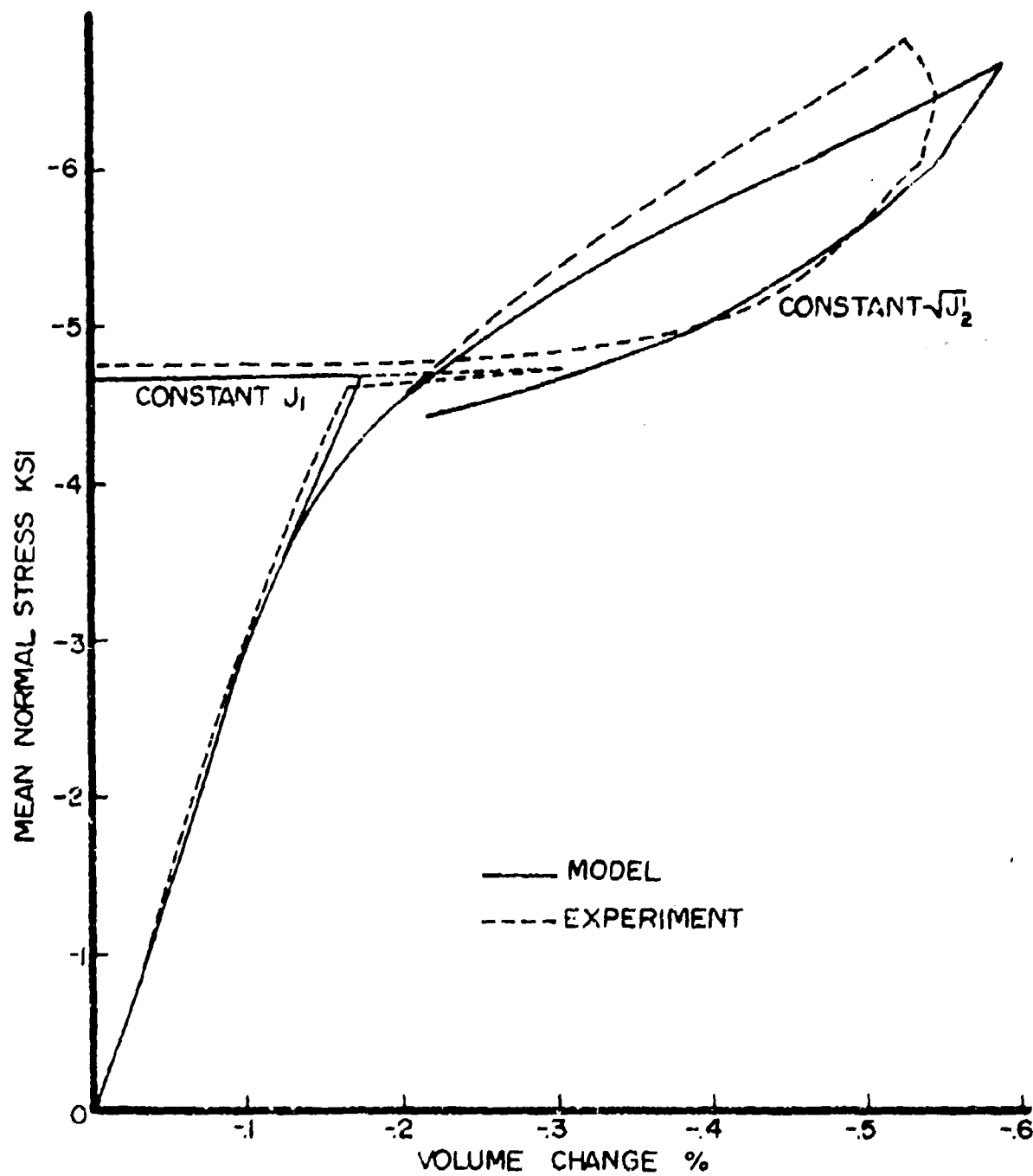


Figure 34. Comparison of model and experimental dilatational stress-strain response in constant $\sqrt{J_2}$ and constant J_1 tests.

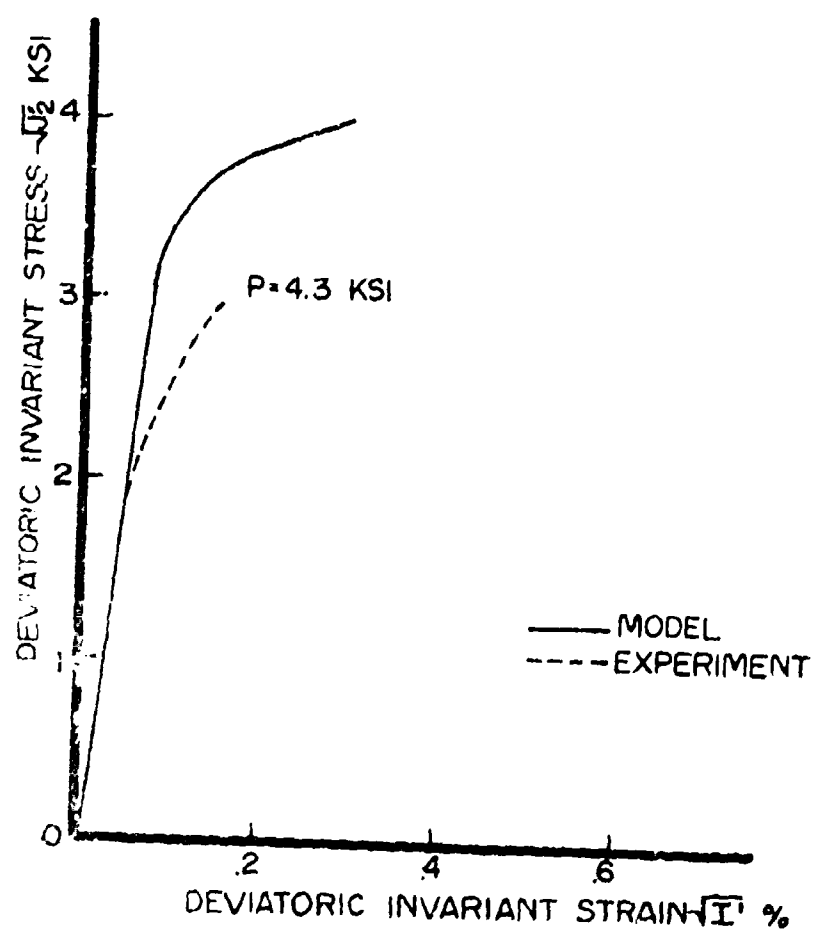


Figure 35. Comparison of model and experimental shearing stress-strain response in extension test.

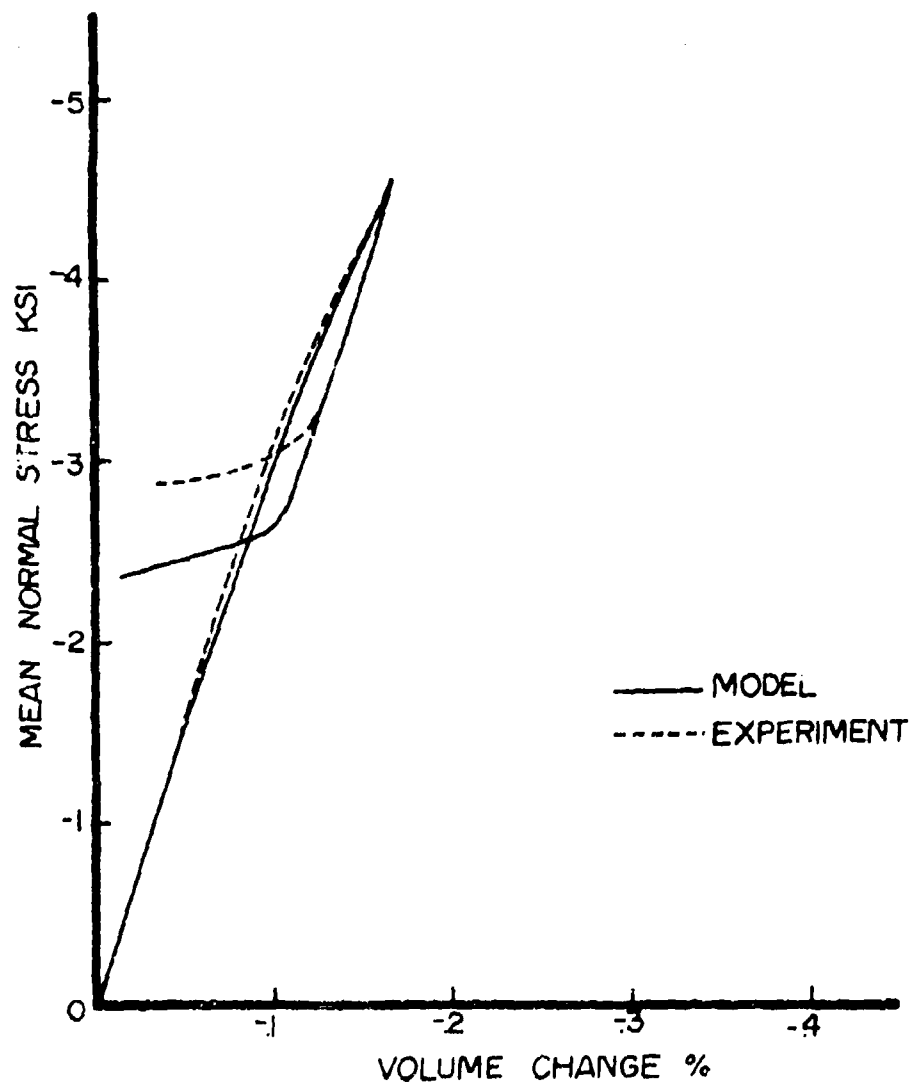


Figure 36. Comparison of model and experimental dilatational stress-strain response in extension test.

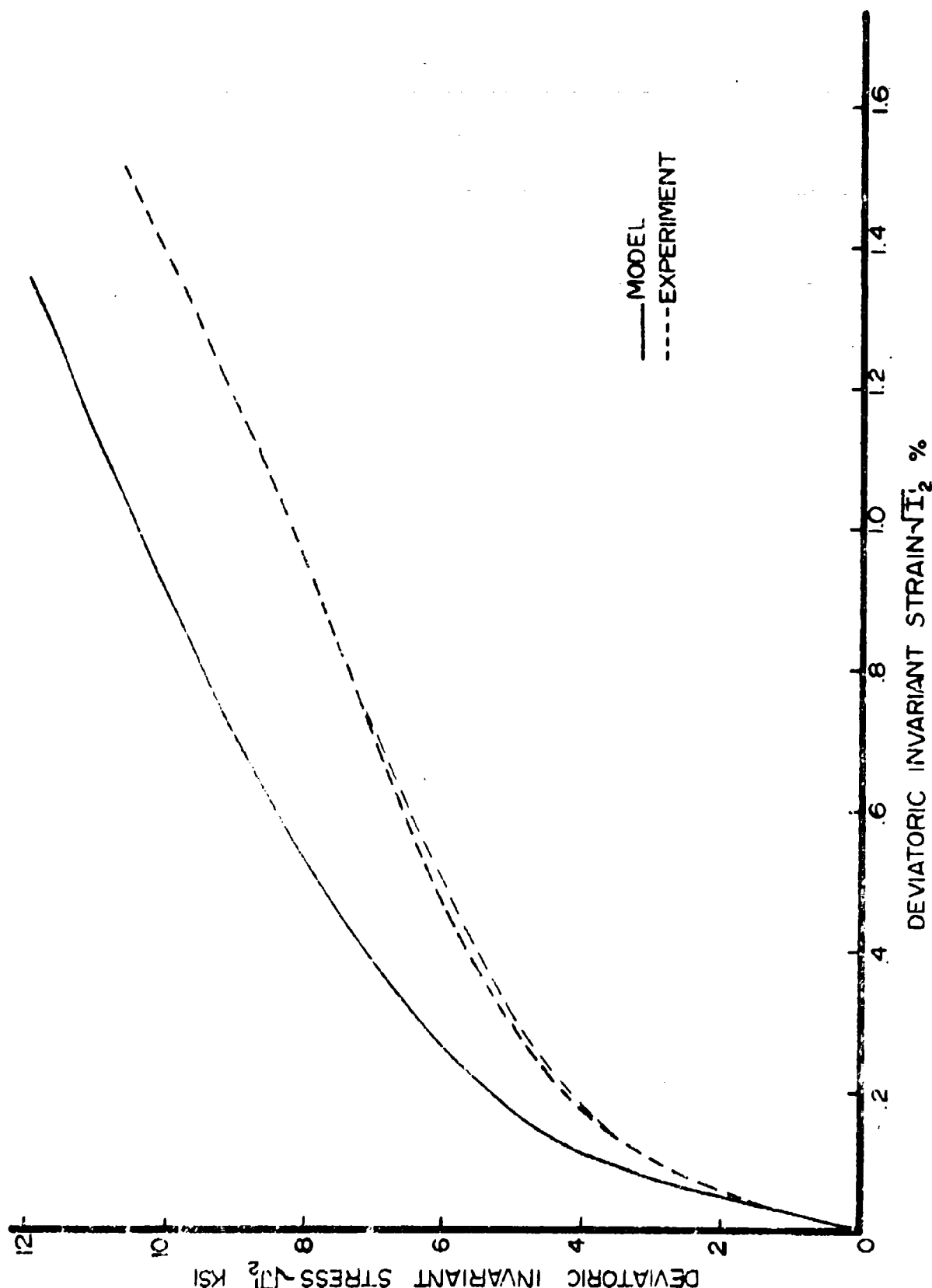


Figure 37. Comparison of model and experimental shearing stress-strain response in one-dimensional strain tests.

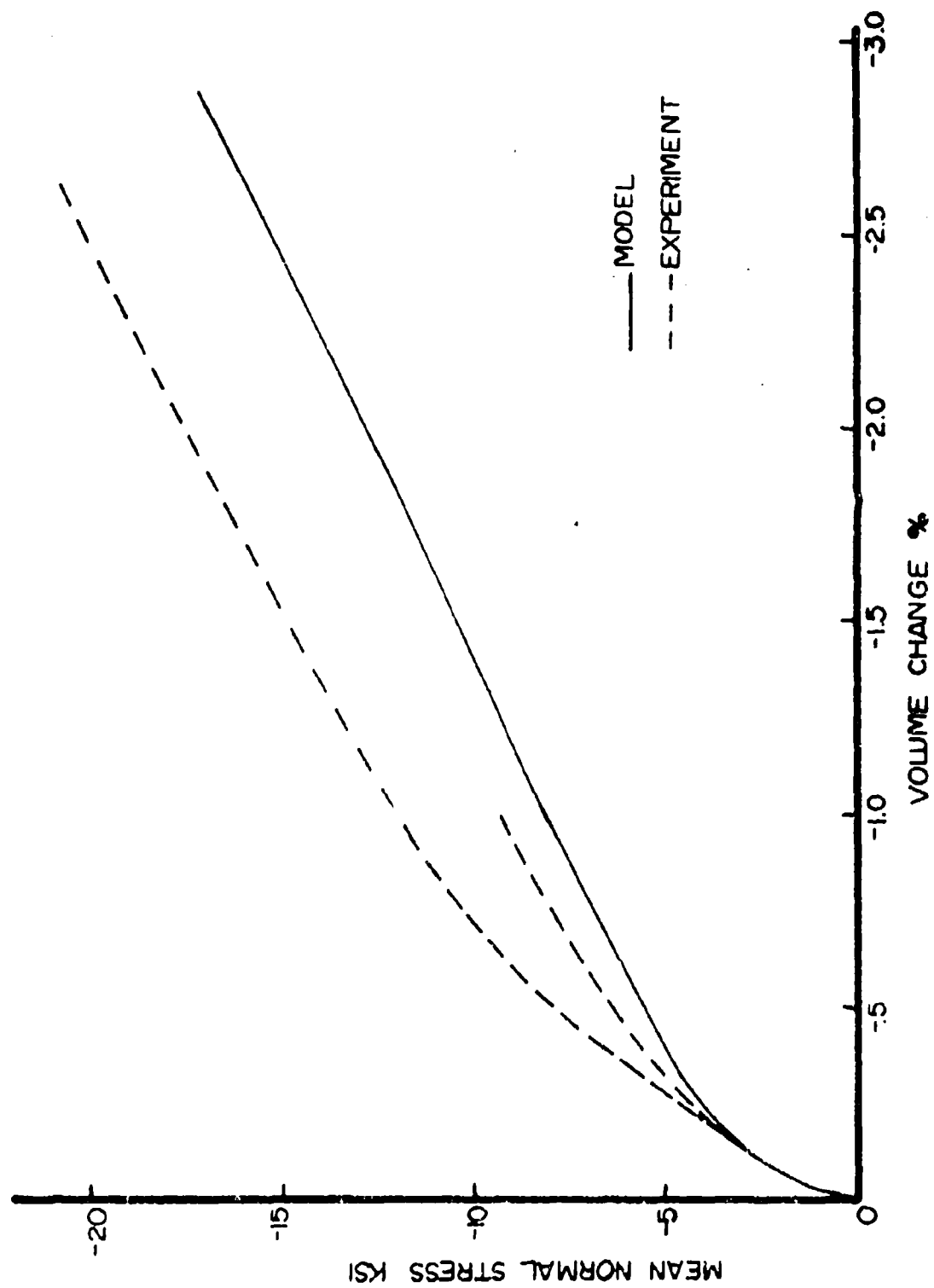


Figure 38. Comparison of model and experimental dilatational stress-strain response in one-dimensional strain tests.

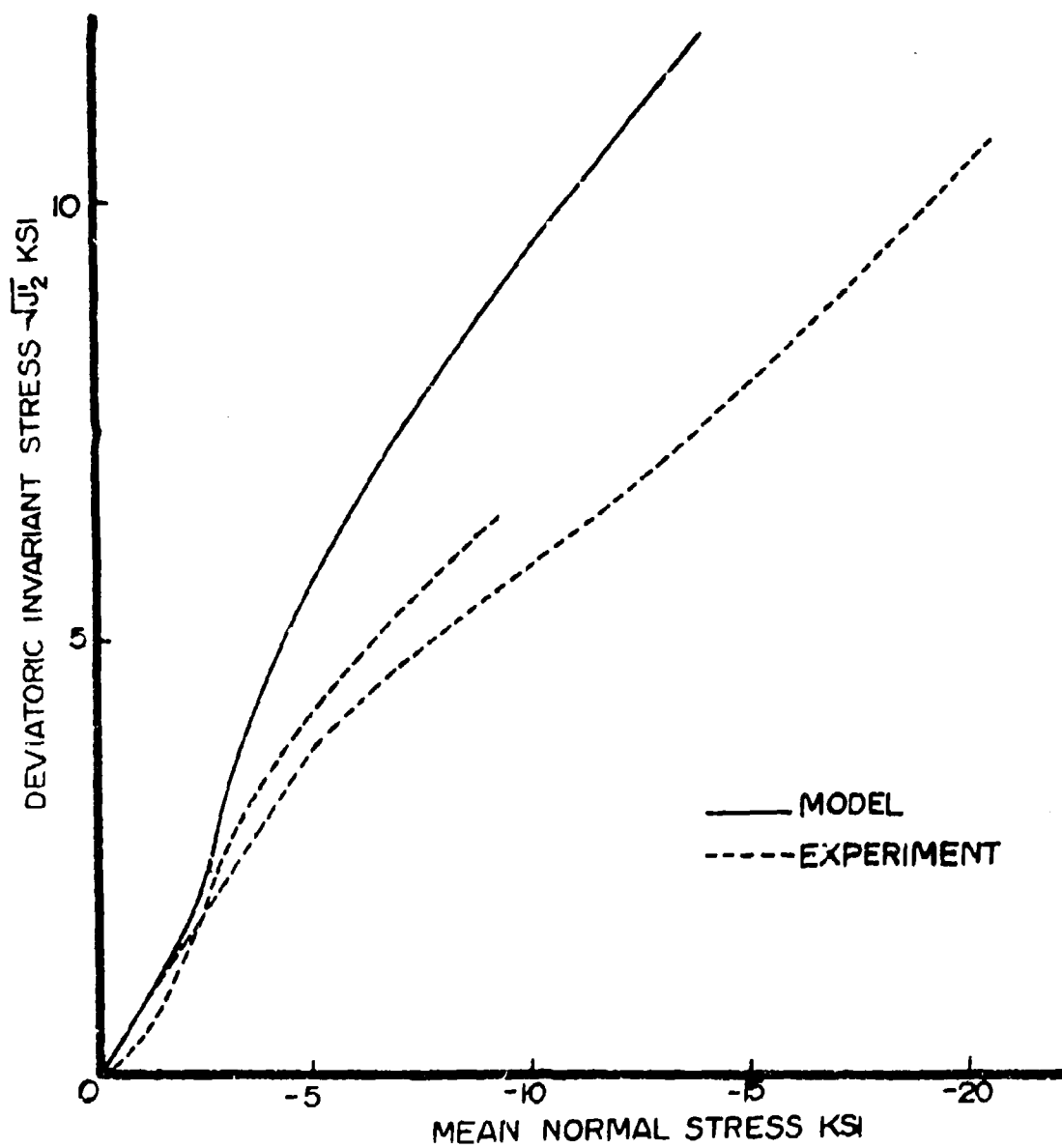


Figure 39. Comparison of model and experimental stress path response in one-dimensional strain tests.

TRIAXIAL STRESS LOAD/UNLOAD
TEST AT 2 KSI PRESSURE

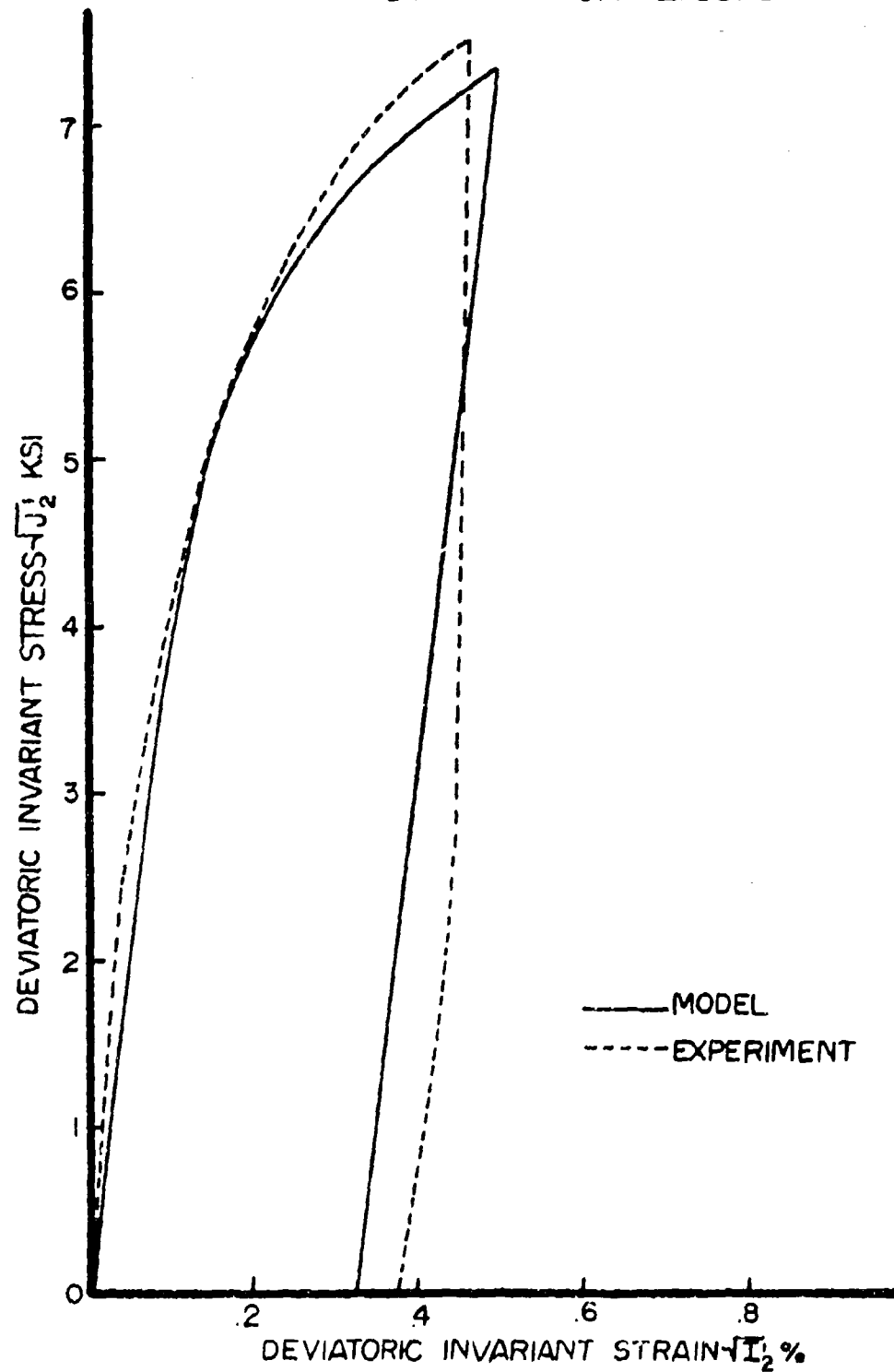


Figure 40. Comparison of model and experimental shearing stress-strain response in constant confining pressure load/unload test.

TRIAXIAL STRESS LOAD/UNLOAD
TEST AT 2 KSI PRESSURE

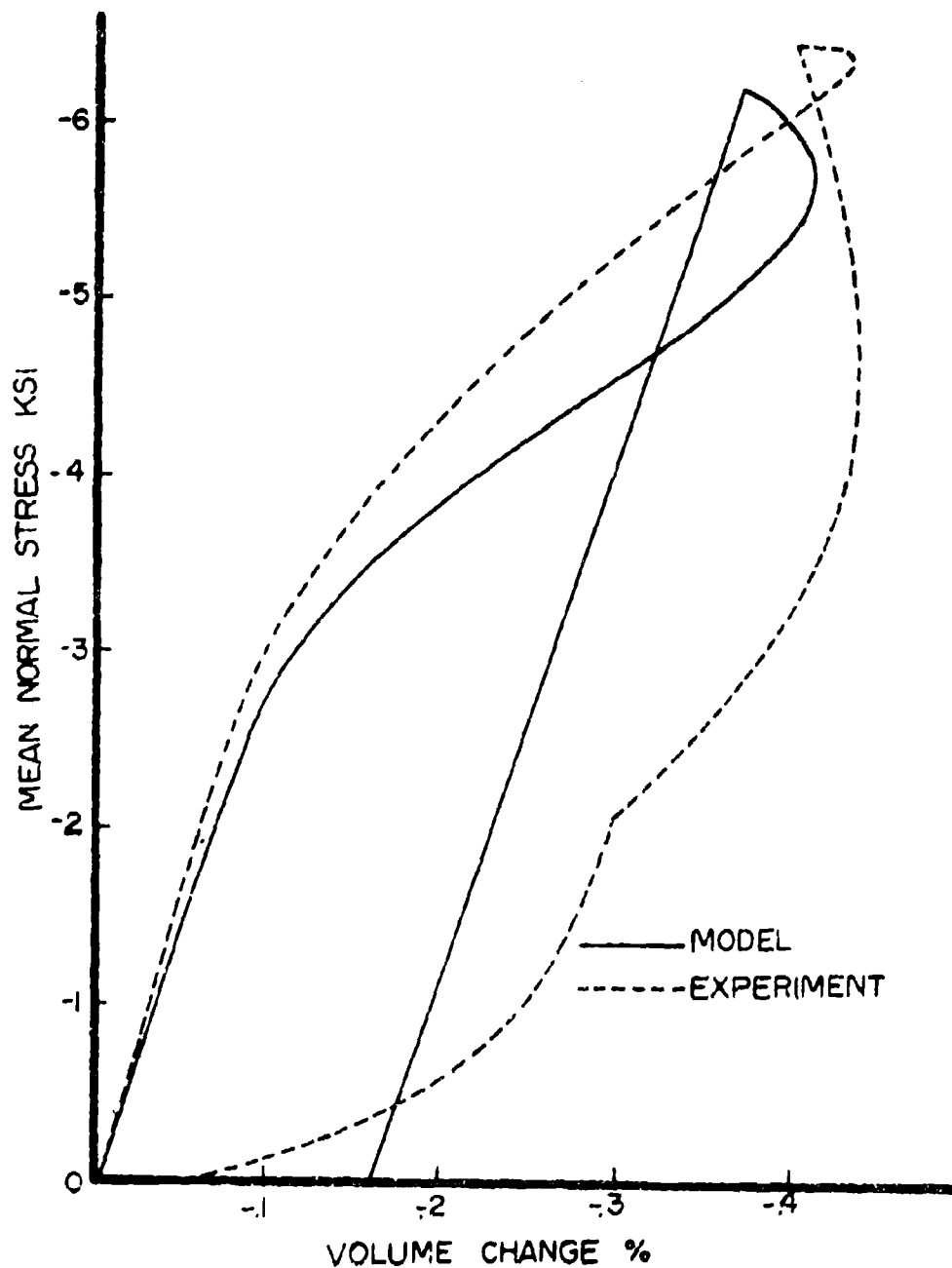


Figure 41. Comparison of model and experimental dilatational stress-strain response in constant confining pressure load/unload test.

experimental data from both tests performed are shown individually in Figures 37 through 39.

Computer Subroutine: The equations of the previous section have been programmed as a subroutine that calculates a stress increment for a given strain increment, state of stress, and plastic strain. A list of definitions of the subroutine variables and a listing of the subroutine are given in Appendix A. In general the variable names have been chosen to conform to the usage of the SLAM computer code. The subroutine utilizes an index notation for stress and strain according to the following notation, using stress as an example:

SIGI (1)	≡	radial stress, σ_{rr}
SIGI (2)	≡	hoop stress, $\sigma_{\theta\theta}$
SIGI (3)	≡	axial stress, σ_{zz}
SIGI (4)	≡	shear stress, σ_{rz}

A description of the subroutine as presently written can best be summarized by the subroutine statement

SUBROUTINE PLASTK (DEPST, SIGI, SI2P, EPSPI, ZK1, ZK2)

The variables are defined as

DEPST (I)	≡	Strain increments
SI2P	≡	Plastic strain deviatoric invariant, $\sqrt{I_2^P}$
EPSPI (I)	≡	Plastic strains
ZK1	≡	Constant in first yield surface
ZK2	≡	Constant in second yield surface

The strain increments are calculated in the main program. The remaining variables are appropriately incremented in the subroutine and must be saved in storage in the main program. The storage of SI2P, the plastic strain deviatoric invariant could be eliminated as this parameter could be calculated from the plastic strain.

Examination of Model Parameters: Although a large number of constants are used in the curve fitting expressions, only six material functions are

actually involved. These are the two linear elastic constants, the two yield functions, and the two hardening rules. Although a systematic study of how these functions would vary with concrete manufacturing variables has not been undertaken, it appears reasonable to assume that the functions would vary in a systematic manner with changes in the concrete material properties. In the following an estimate of how the functions could be changed to accommodate different concrete properties is given.

The minimum test data necessary to define the six functions could consist of stress-strain data from an unconfined compression test, a triaxial compression test at 2 ksi confining pressure, and a hydrostatic loading test. Further tests would, of course, add confirmation to the results. The six material functions would then be obtained as follows:

Bulk Modulus B: The slope of the approximately linear portion, say up to a pressure of 4 ksi, of the hydrostatic test plotted as pressure versus volumetric strain.

Shear Modulus G: One half times the slope of the approximately linear initial portion of the triaxial test, plotted as $\sqrt{J_2'}$ versus $\sqrt{I_2'}$.

Yield Function F_1 : The function F_1 is given in the form of

$$F_1 = \sqrt{J_2'} + \{g_1(J_1) - K_1\}$$

The term in brackets () should be multiplied by the ratio of the unconfined compressive strength to -7000 psi, which is the value of the unconfined compressive strength of the concrete used in the present studies, that is multiplied by $\sigma_c / -7000$.

Yield Function F_2 : No change

Hardening Rule h_1 : No change

Hardening Rule h_2 : The function h_2 is written in two terms as

$$h_2 = -f(\sqrt{J_2'}) - g(J_1)$$

The function f should be multiplied by the ratio of the strain termed "S" in the $P = 2$ ksi triaxial test illustrated in Figure 42 to the same strain in the present concrete, taken as 0.0018. That is, multiply " f " by $S/0.0018$.

The function g of h_2 should be multiplied by the ratio of the strain termed "T" in the hydrostatic test illustrated in Figure 43 to the same strain in the present concrete, taken to be 0.029. That is, multiply " g " by $T/0.029$.

It should be emphasized that the above procedure has not been verified experimentally. Rather it represents an estimate of how the model of the present investigation might be modified for a somewhat different concrete.

Discrepancies Between Model and Data: Certain features of concrete behavior exhibited in the laboratory have not been expressed explicitly in the mathematical representation at this time. One of these features is a path dependent unloading seen in the dilatational stress-strain curves of tests unloaded from near maximum load. In the model, elastic unloading is assumed in both shear and bulk. The real material behavior indicates that part of the volumetric bulking may be recoverable, and in a way that depends on the unloading path. An example of unloading in a triaxial (constant confining pressure) test is shown in Figures 40 and 41. The model assumes isotropic behavior and does not include the anisotropy produced by directional microcracking. This behavior would show up in reloading tests of concrete loaded near maximum stress, and particularly if the directions of the

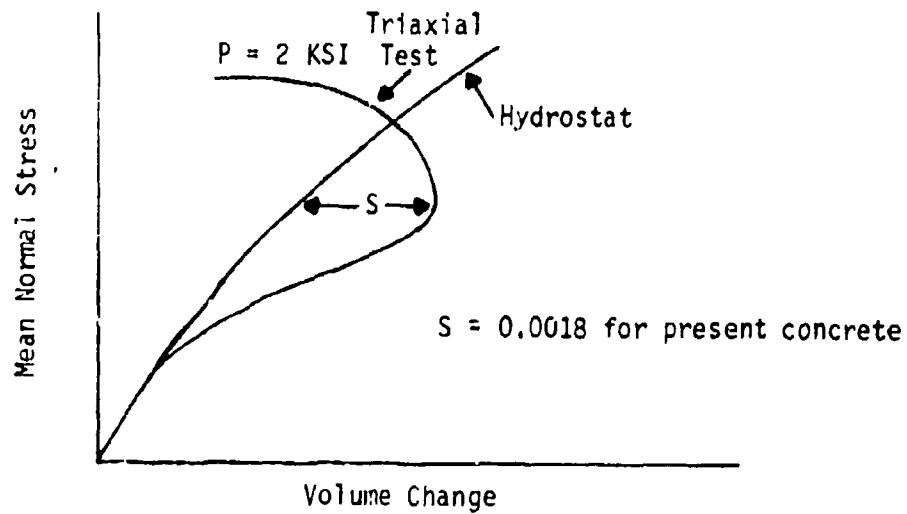


Figure 42. Illustration of volumetric strain "S" used for correction of model parameter H_2 for different concrete.

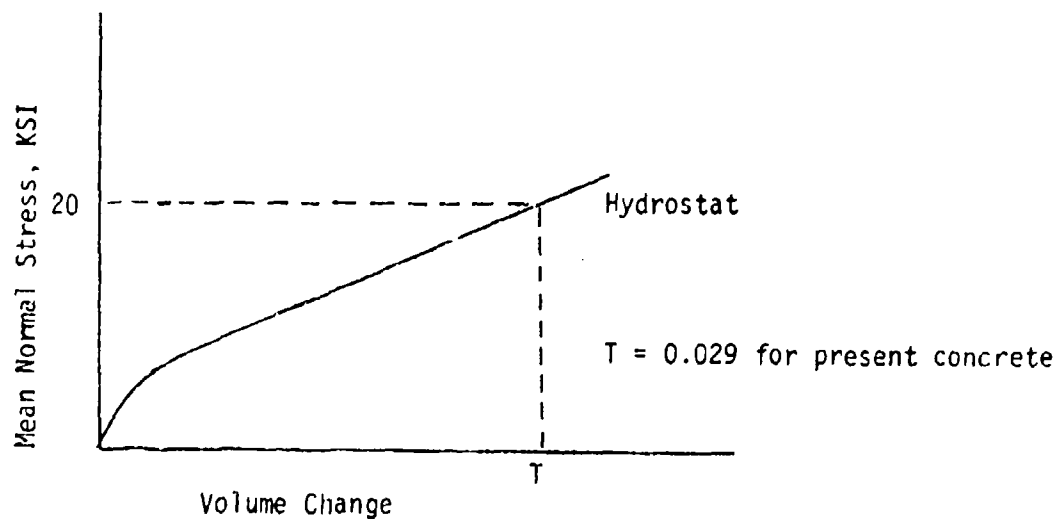


Figure 43. Illustration of volumetric strain "T" used for correction of model parameter H_2 for different concrete.

principal stress axes were rotated.

Another area of uncertainty in the present model is in the detailed description of the yield surface and maximum stress surface. The maximum stress locus has been represented in $\sqrt{J_2}$ versus J_1 coordinates in the model. It has been well established in the literature and in the present program that the maximum stress locus is not unique in these coordinates, but can vary with the type of test. In general as discussed earlier, the triaxial extension and triaxial compression test results appear to form separate curves, with biaxial compression results falling in between. Various techniques have been used to rectify this. Mills and Zimmerman (Ref. 20) have modified the shearing invariant with the addition of a "rotational term." In a similar situation for rocks, Mogi (Refs. 38,39) have modified the mean normal stress invariant by adding a weighting factor to the intermediate principal stress. An example of this for granite is shown in Figure 44. It should be noted that although the fit is apparently quite consistent in the coordinates of Figure 44, a replotting of the data in terms of a biaxial stress envelope can lead to anomalies. Further complicating the situation is the normality rule (associated flow rule) used in the plasticity model that serves to link the strength and stress-strain behavior. Although some biaxial stress-strain data are available, as by Kupfer, Hilsdorf, and Rusch (Ref. 15) for example, the situation has not been adequately studied.

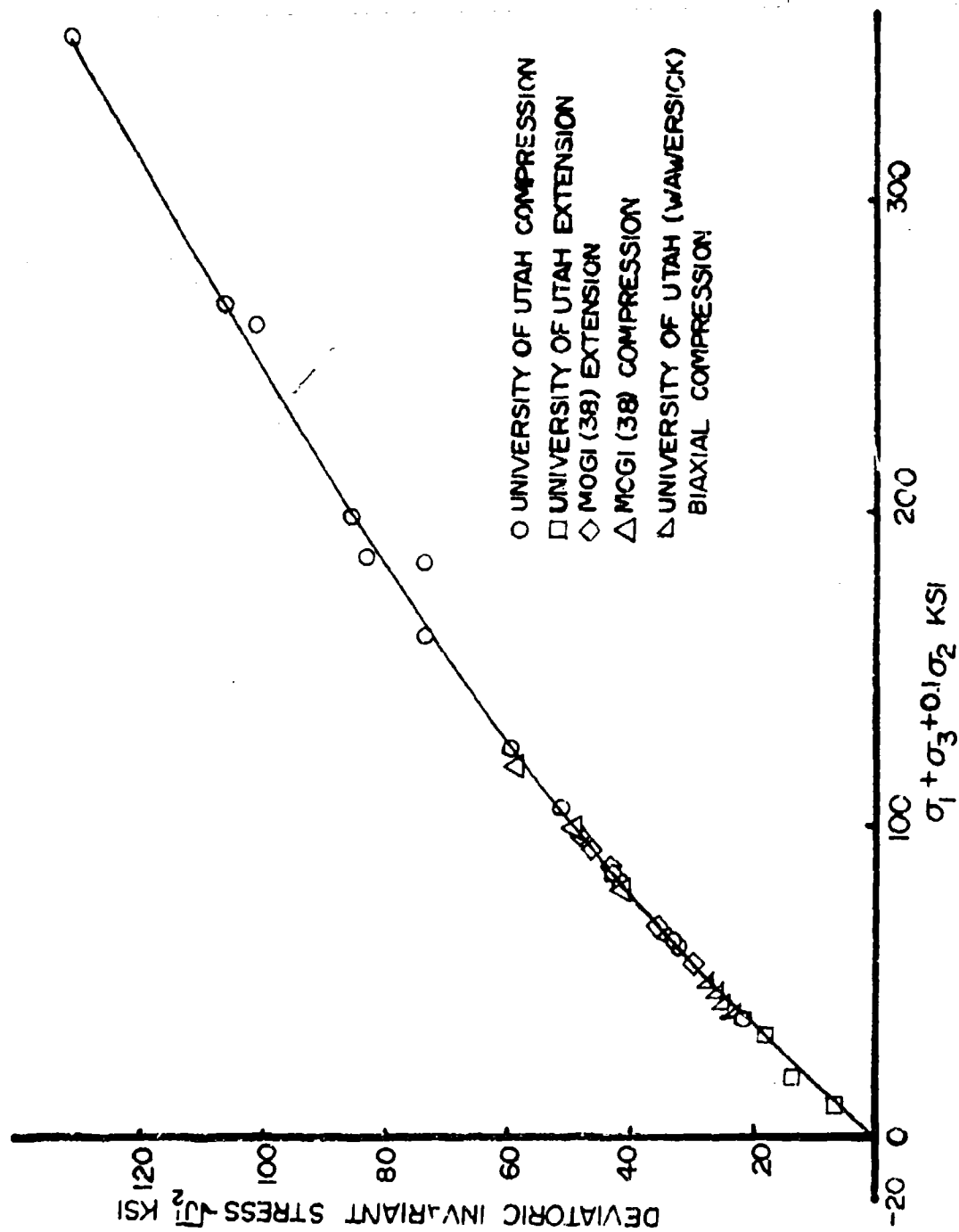


Figure 44. Failure locus for Westerly granite (uniform stress).

SECTION VII

COMPARISON TO THICK WALLED CYLINDER TESTS

A series of tests was performed on thick-walled concrete cylinders. These tests consisted of combinations of axial compression and internal pressure, producing combined compressive and tensile stresses in the concrete. To ensure an adequate wall thickness to aggregate ratio, 3/8-inch nominal aggregate size was used with a 2-inch-thick cylinder wall. The overall cylinder configuration was 7 inches I.D., 11 inches O.D., and 20 inches long.

Since the concrete constitutive model was formulated before the cylinder tests were performed, these tests served as a verification check of model parameters. A description of the analysis and comparison of theory and experimental results follows.

Analysis: If the concrete cylinders are treated as "thin walled", the hoop stresses are given simply as

$$\sigma_{\theta\theta} = \frac{pr}{t}$$

where p is the internal pressure, r is the radius (presumably an average of the inside and outside radius), and t is the wall thickness. However, because the radius varies from 3.5 inches to 5.5 inches it was considered necessary to use thick-walled cylinder theory to determine the distribution of radial and circumferential stresses and strains. This was accomplished by developing a finite difference computer code that used the concrete elastic-plastic constitutive model. The equations were derived by considering the usual equations (Ref. 40).

equilibrium:
$$\frac{d\sigma_{rr}}{dr} + \frac{\sigma_{rr} - \sigma_{\theta\theta}}{r} = 0 \quad (42)$$

strain-displacement:
$$\epsilon_{rr} = \frac{dU}{dr} \quad (43)$$

$$\epsilon_{\theta\theta} = U/r$$

stress-strain law (in incremental form);

$$d\sigma = C d\epsilon \quad (44)$$

where C is the concrete elastic-plastic stress-strain matrix. These equations were written in finite difference form after eliminating the strains in terms of the radial displacement U . The finite difference equations were readily programmed; a listing of the program is given in Appendix B. The axial stress and internal pressure were input in incremental form. The axial stress was assumed uniformly distributed throughout the cylinder and related to the measured axial load by the relationship

$$\sigma_{zz} = F/A \quad (45)$$

A check solution is shown in Figure 45 for the case of internal pressure only using elastic properties. It can be seen that good agreement was obtained using 11 mesh points. This number was used for all of the concrete cylinder solutions.

Discussion of Results: The results of the cylinder tests are shown in Figures 46 through 52. In these figures the axial stress, internal pressure, axial and circumferential strain both at the inner and outer surface of the cylinder are plotted versus the elapsed time of the test. Also shown in these figures are the strains in the axial and circumferential directions at the inner and outer surface

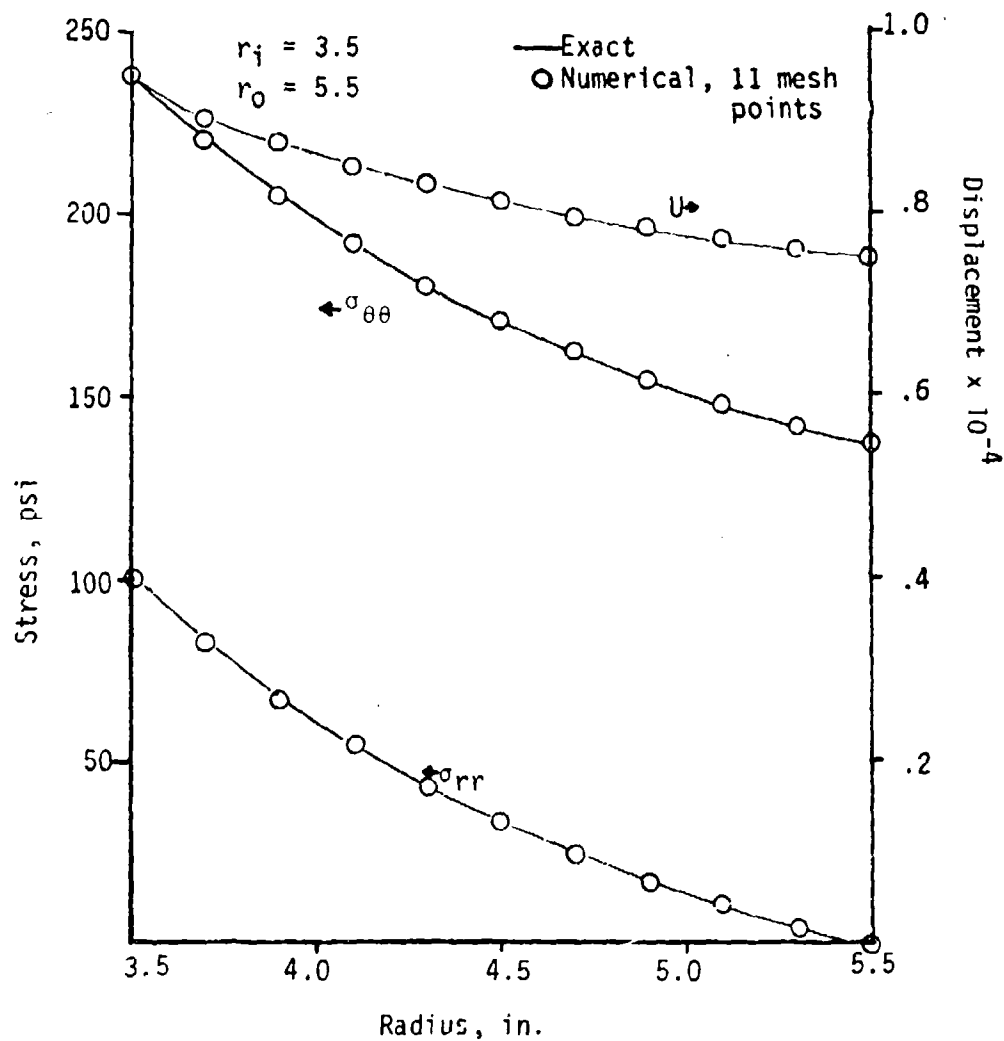


Figure 45. Comparison of numerical and exact solution for elastic thick-walled cylinder.

predicted by the numerical solution.

In general the comparison between the numerical solution and the experimental results is within the consistency of the test results. The comparisons for tests 8-3 and 8-4 shown in Figures 51 and 52, respectively, were relatively much poorer than the others. It is not apparent why this should be; however, both of these tests had a very high initial axial pre-load before the internal pressure was applied. Apparently the model exaggerates the circumferential strain at these stress levels. This could indicate that the yield function F_1 should be increased somewhat more for the cylinder concrete, or else the dilatancy effect may be too pronounced for this stress condition. However, the relatively much better comparison for the other tests suggest that the experimental results for tests 8-3 and 8-4 may not be entirely consistent with the others.

An interesting phenomenon was noted in the analysis of the cylinders. In the usual elastic-plastic cylinder under internal pressure, using say a Tresca or Von Mises yield criterion, yielding starts at the inner bore and progresses outward as the pressure is increased. In the present analysis yielding was observed to start at or near the outer surface. This can be explained by considering the pressure sensitivity of yielding in concrete. The pressure at the inner bore was evidently sufficient to shift the location of initial yielding. As a consequence of this, the "thick-wall" effect is not as pronounced for the concrete analysis as it would be for a pressure-independent elastic-plastic material.

Summary: Axial force and internal pressure tests were run on concrete cylinders. These cylinders were analyzed using thick-walled cylinder theory in conjunction with the material property model developed for concrete.

Comparison of theory and experiment was relatively good for all tests,

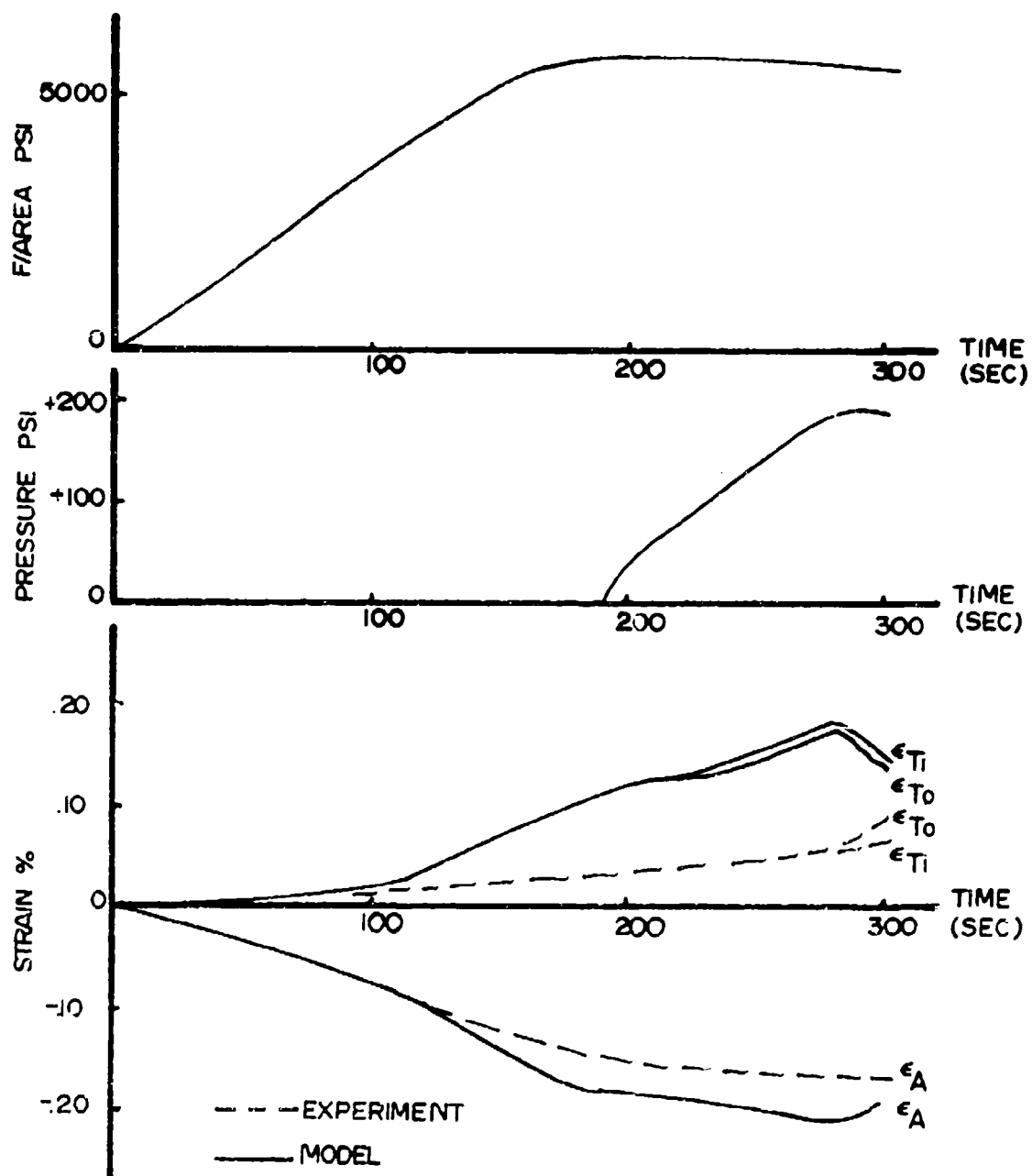


Figure 46. Comparison of model and experiment for cylinder 7-1.

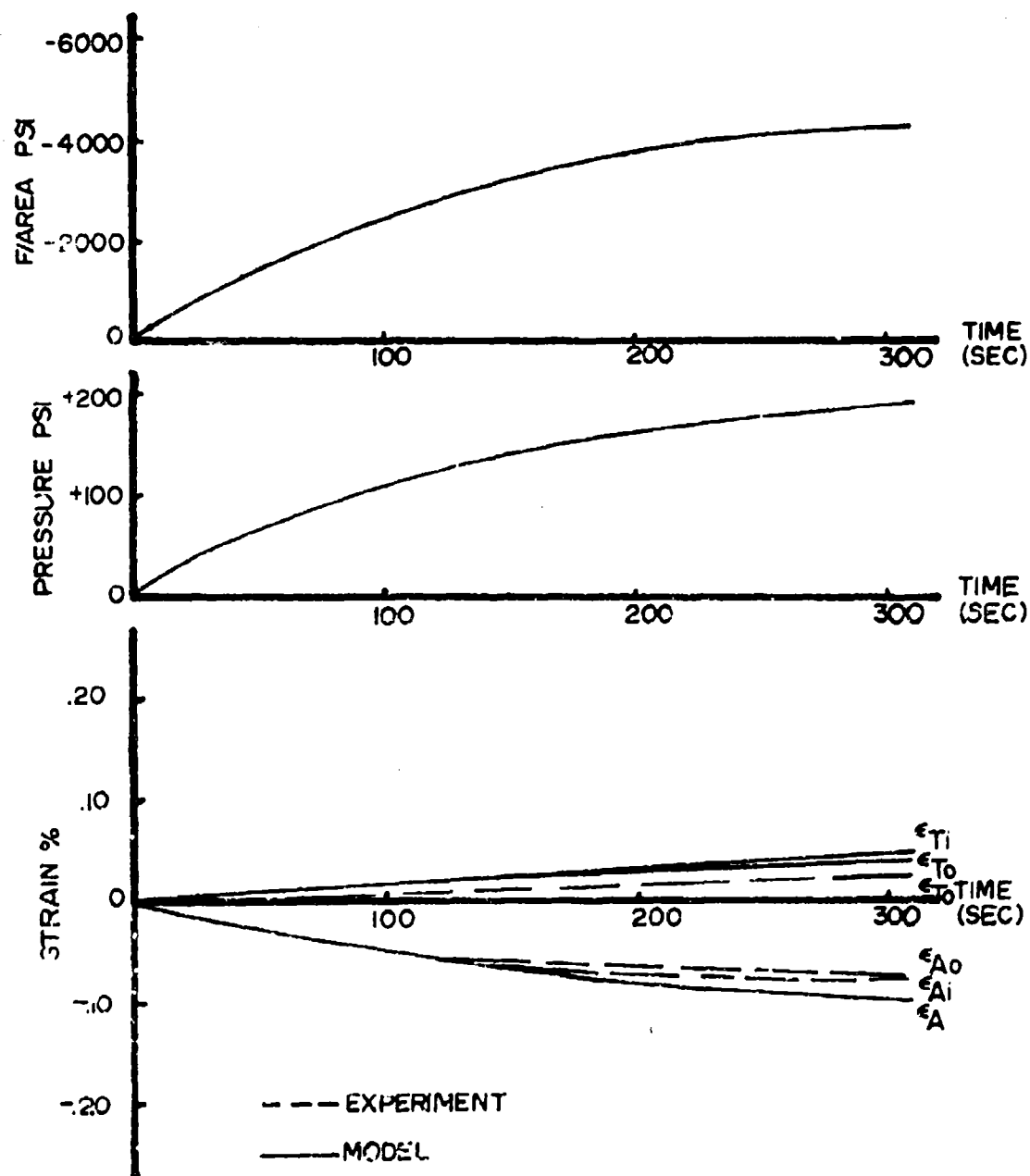


Figure 47. Comparison of model and experiment for cylinder No. 7-2.

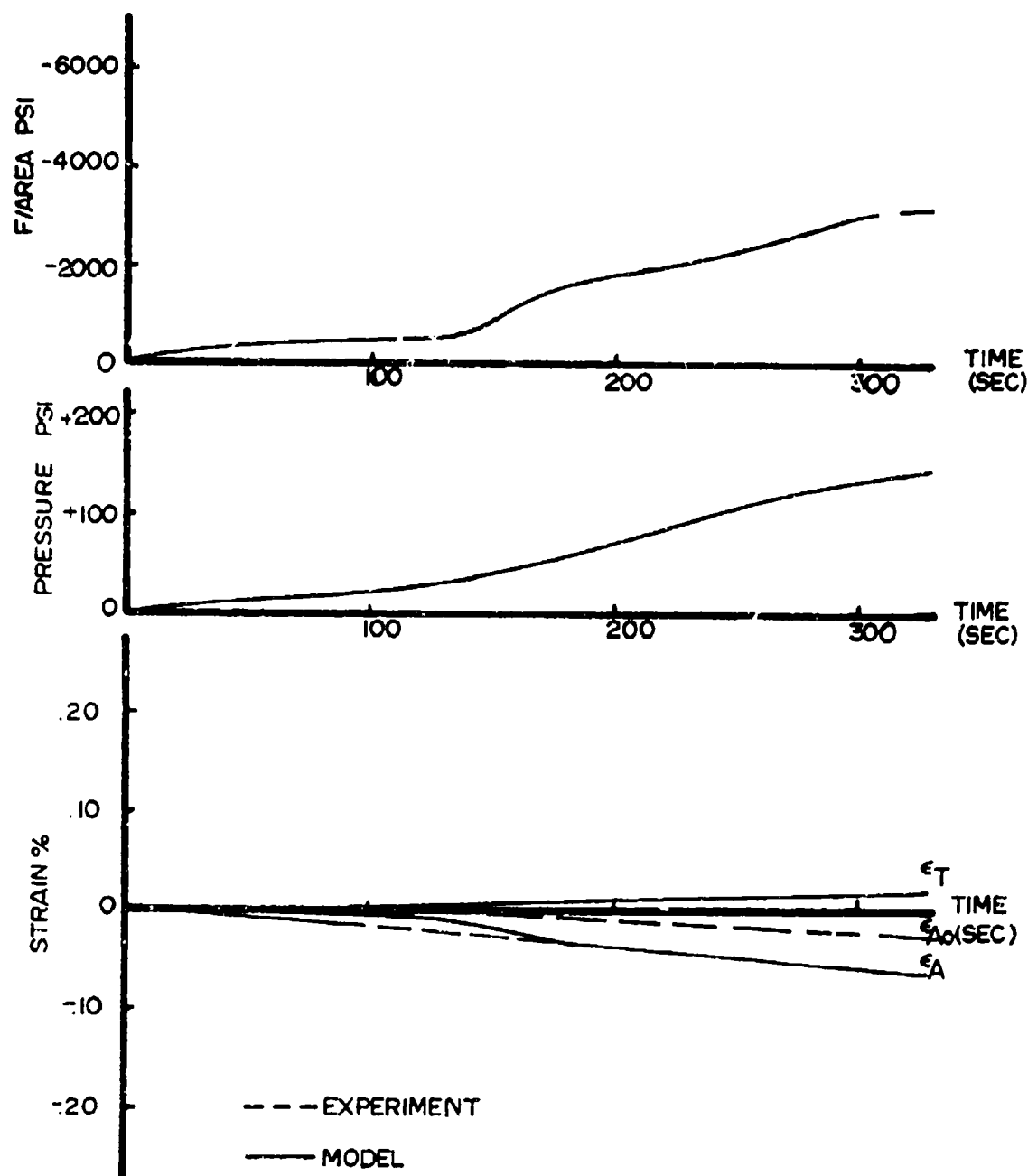


Figure 48. Comparison of model and experiment for cylinder No. 7-3.

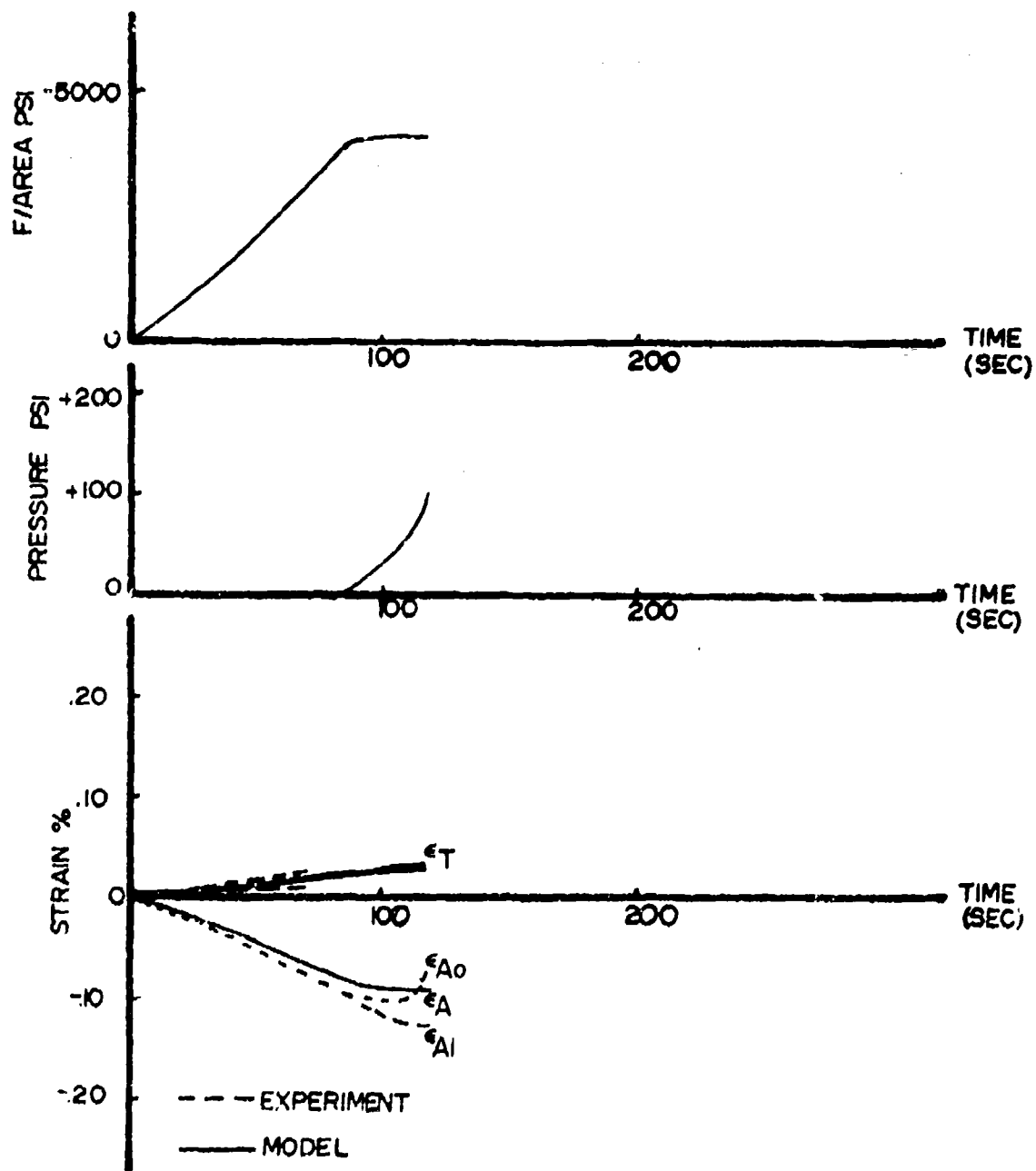


Figure 49. Comparison of model and experiment for cylinder No. 7-4.

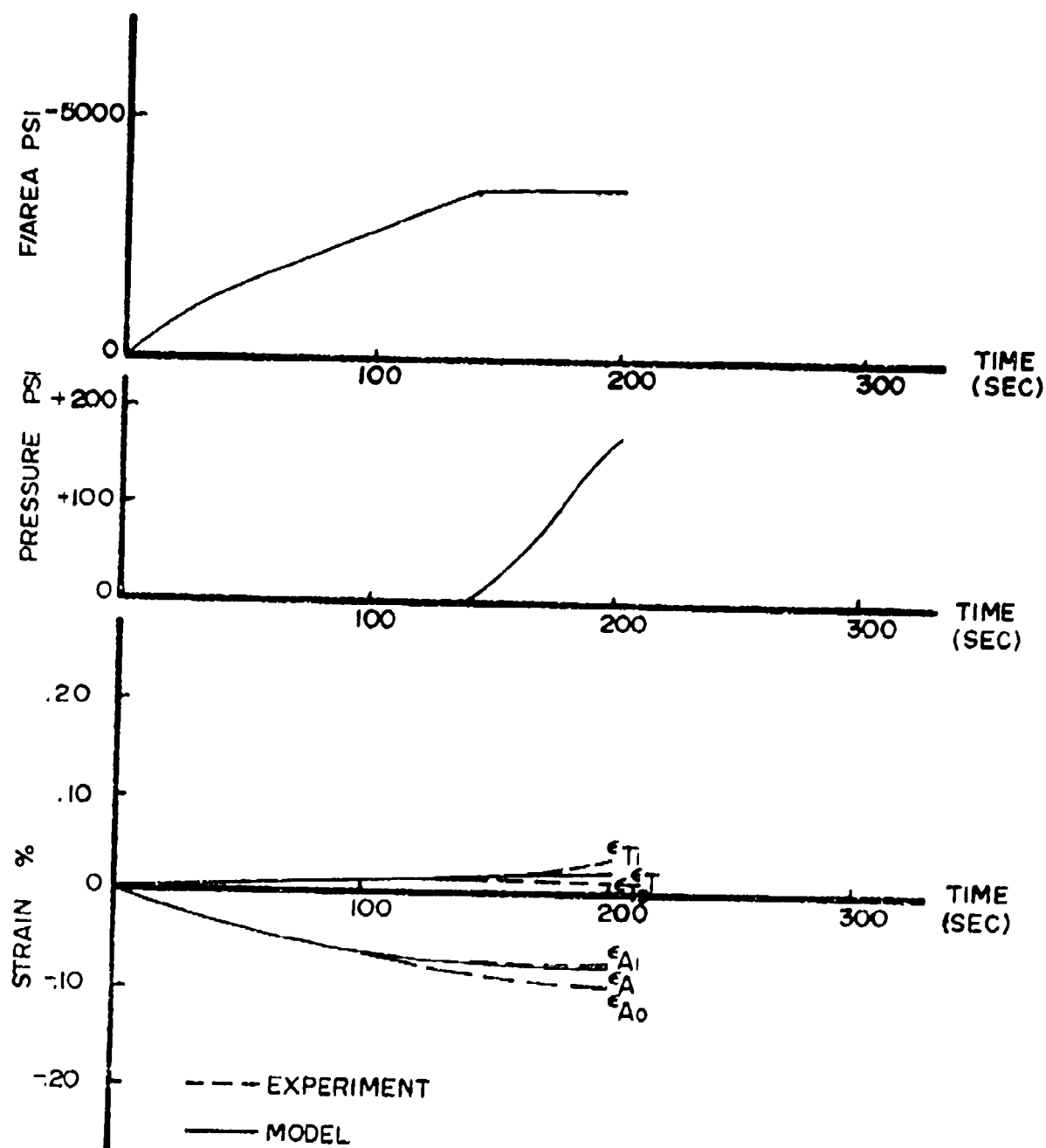


Figure 50. Comparison of model and experiment for cylinder No. 8-2.

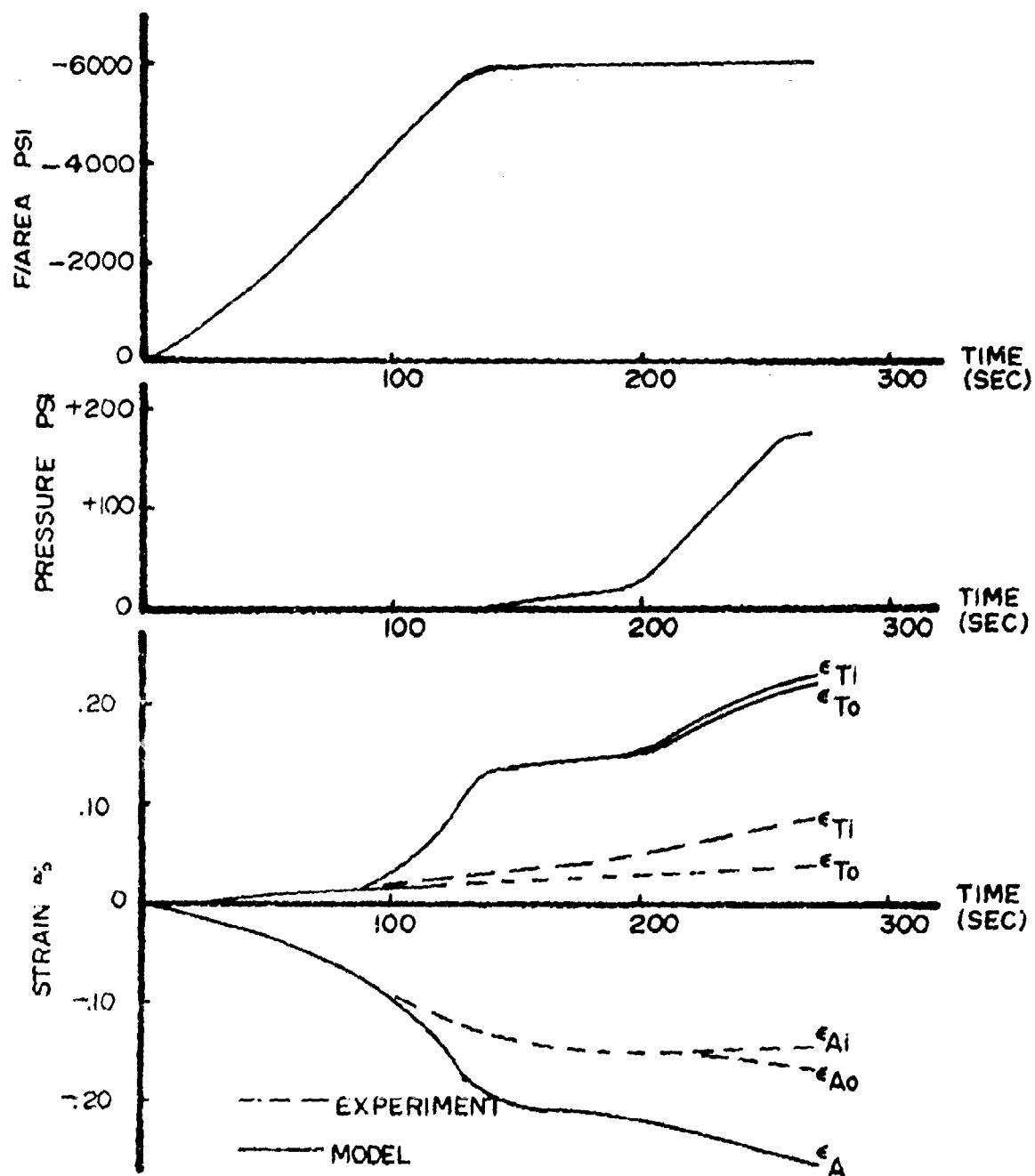


Figure 51. Comparison of model and experiment for cylinder No. 8-3.

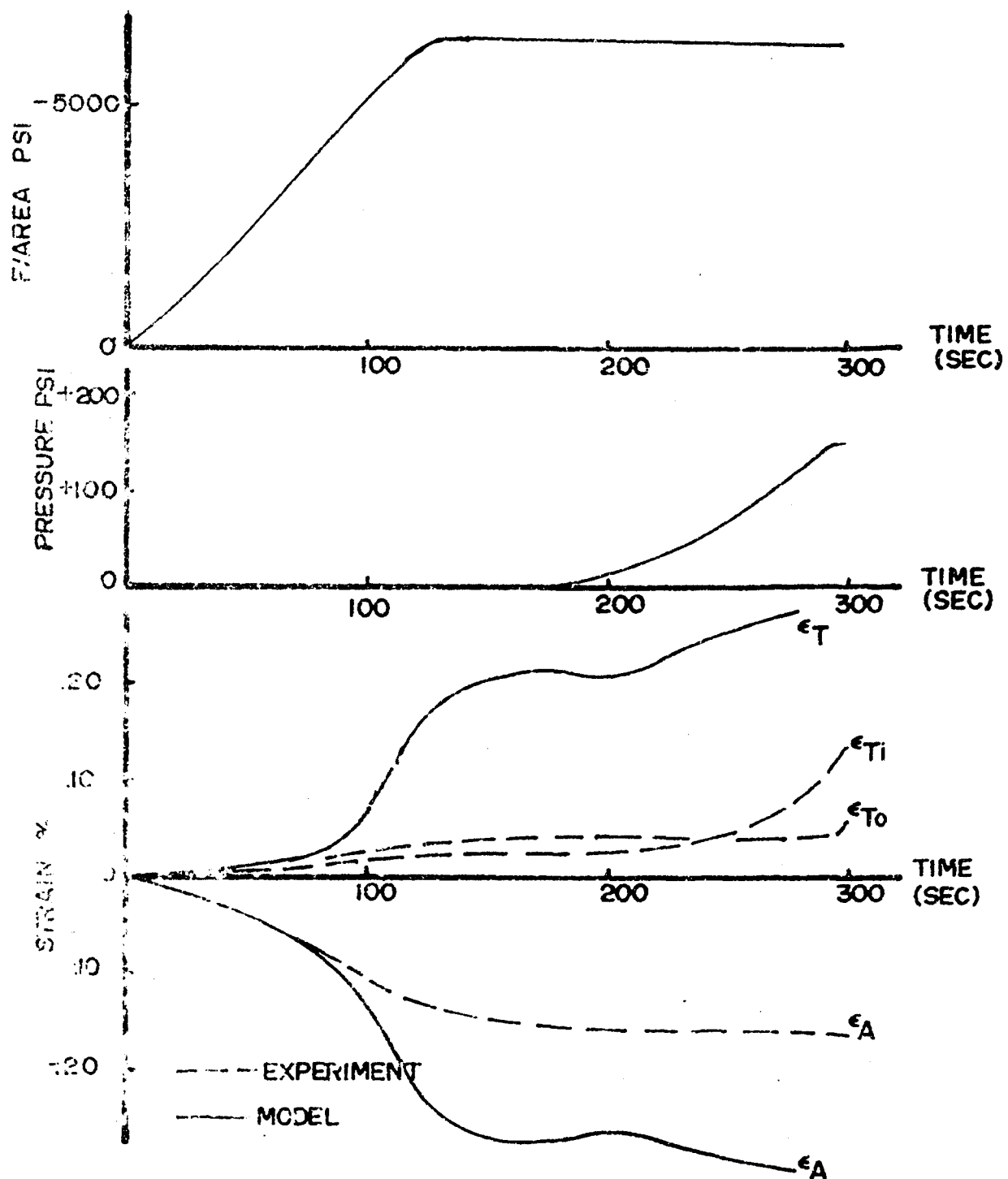


Figure 52. Comparison of model and experiment for cylinder No. 8-4.

although cylinders 8-3 and 8-4 were much poorer than the others. The evidence for explaining the poorer comparison of these two tests is not conclusive.

SECTION VIII

SUMMARY AND CONCLUSIONS

1. Although comparison of test data from different laboratories is very difficult because of the large variability and the complex response of concrete, data available in the literature do show some of the deformation features of concrete, including the increase in strength with pressure, the dependence of the yield on stress state and dilation which occurs near maximum stress. Tests here provided added detail to the stress-strain response and showed added features of deformation including a) compaction associated with shear deformation occurs before the onset of large scale dilation and b) the unloading is not elastic but shows complex unload paths which suggest anisotropic hardening and strain induced anisotropy. To a lesser extent the tests here showed the extreme sensitivity of the mechanical properties to casting procedures, and the importance of the specific aggregate surface area in determining concrete strength. The strength appeared to be far more sensitive to surface area than to aggregate size variation from 3/16 to 3/4-inch diameter aggregate.

2. The random and relatively homogeneous distribution of aggregate, cement matrix, water and voids and the general response of the concrete, including dilation and permanent set, are suggestive of a continuum, elastic-plastic model. It is not implied that concrete exhibits 'metal plasticity', but that plasticity models might adequately be used to phenomenologically model concrete as has previously been done very successfully for geologic materials. In a sense the model used here is an extension of the initial plasticity model used by Swanson to fit rock data, with the yield cap as suggested by Baron, et al. An associated flow law and a segmented yield

function have been used with a hardening law which includes the shear and dilatation terms. The segmented yield and selected hardening laws allow for compaction followed by dilation, as well as the more conventional pressure sensitivity of yield.

3. An independent check of the model has been made by calculating surface strains on a thick-walled cylinder subjected to a programmed internal pressure and axial load, and comparing the calculated strains to those measured during the loading. The thick-walled cylinders represented a concrete with a somewhat different strength, and hence, in effect represented a different batch of concrete. Comparison between the finite difference calculation and measured strain was relatively good and provided some confidence that the model developed to generally fit the features of deformation of concrete was adequate for predicting the loading response of a concrete structure.

4. The model developed does not adequately handle unloading, nor does it fit in detail the stress state dependence of yield. The latter effect would not be difficult to include as sufficient data become available. Anisotropy is not considered, nor are environmental effects such as temperature or water, or preconditioning effects such as a preshock or preload. Time-dependent effects, creep or high-strain rate loading, are not considered.

APPENDIX A

CONSTITUTIVE EQUATION SUBROUTINE

SUBROUTINE VARIABLE DEFINITIONS

AB1, AB2, AB3, AB4, AB4	
A1, A2, A3, A4, A5, A6	Terms in expression for λ_1 and λ_2
B1(I), B2(I)	
AGO	Shear modulus, psi
AKBULK	Bulk modulus, psi
AJ1I	First stress invariant, J_1 , psi
AJ2I	Second deviator stress invariant, J_2'
C(I,J)	Matrix of elastic constants
DEHP	1st plastic strain invariant, I_1^P
DEPST(I)	Total strain increments
DF1	Loading increment on 1st yield surface
DF2	Loading increment on 2nd yield surface
DS(I)	Stress increment associated with elastic strain
EL1	Lame constant, psi
EPSPI(I)	Plastic strains
FSI(I)	Partial derivative vector of F_1 with respect to stress
FS2(J)	Partial derivative vector of F_2 with respect to stress
F1	1st yield surface
F2	2nd yield surface
H1	Strain hardening function for 1st yield surface
H2	Strain hardening function for 2nd yield surface
PDE(J)	Plastic strain increment
SIGI(I)	Stresses
SIGDI(I)	Deviator stress
SI2P	2nd plastic deviator strain invariant, $\sqrt{I_2^P}$
SI2PS	Square of SI2P
SJ2	Square root of J_2' , $\sqrt{J_2'}$
TDS(I)	Stress increment associated with plastic strain
TZL2	Temporary name for λ_2
T1, T2, T3, T4, T5, T6	Terms of various functions
ZK1	Constant in 1st yield surface
ZK2	Constant in 2nd yield surface
ZL1	Constant in associated flow law, λ_1
ZL2	Constant in associated flow law, λ_2

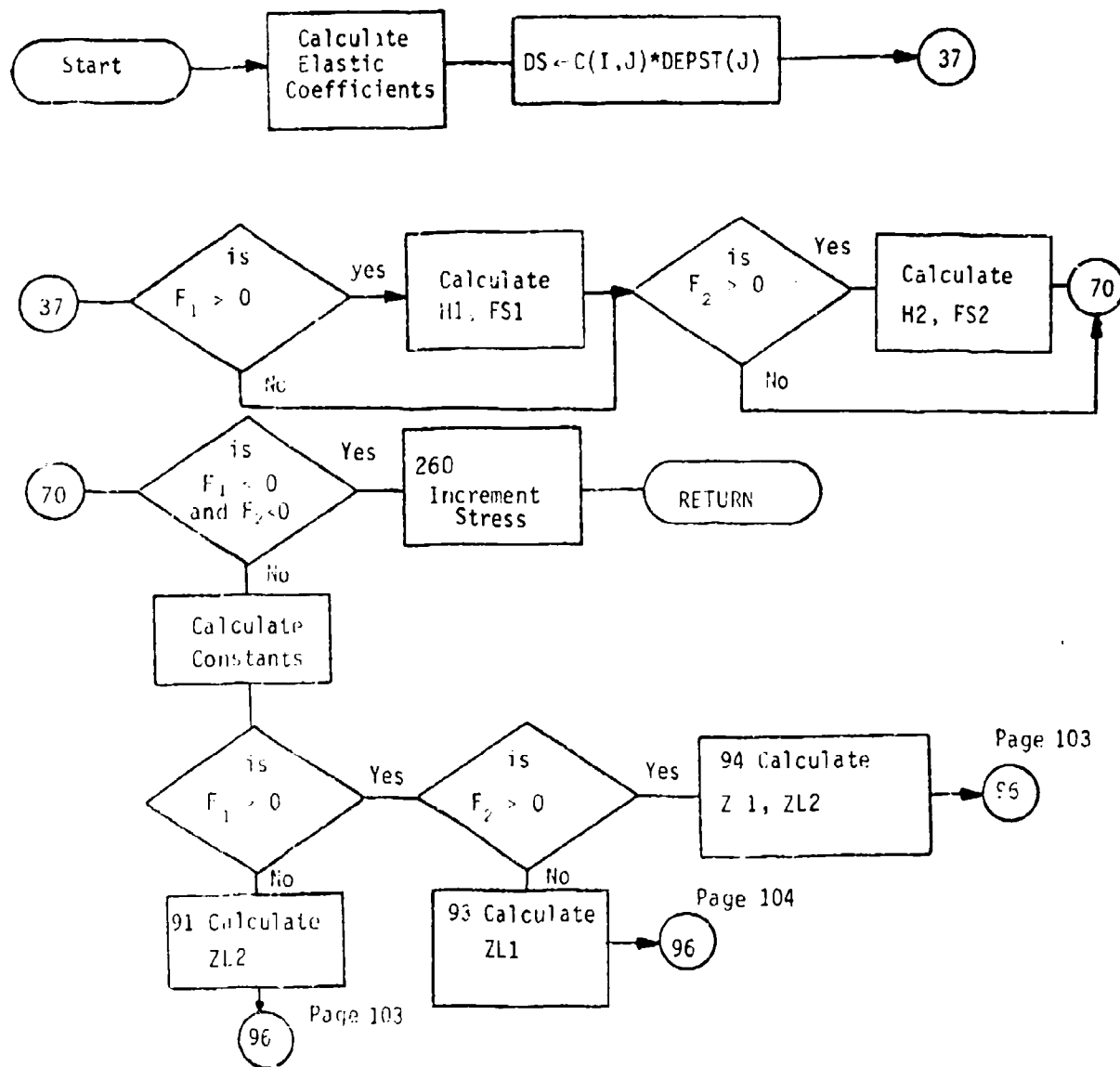


Figure 53. Subroutine PLASTK Flow Chart

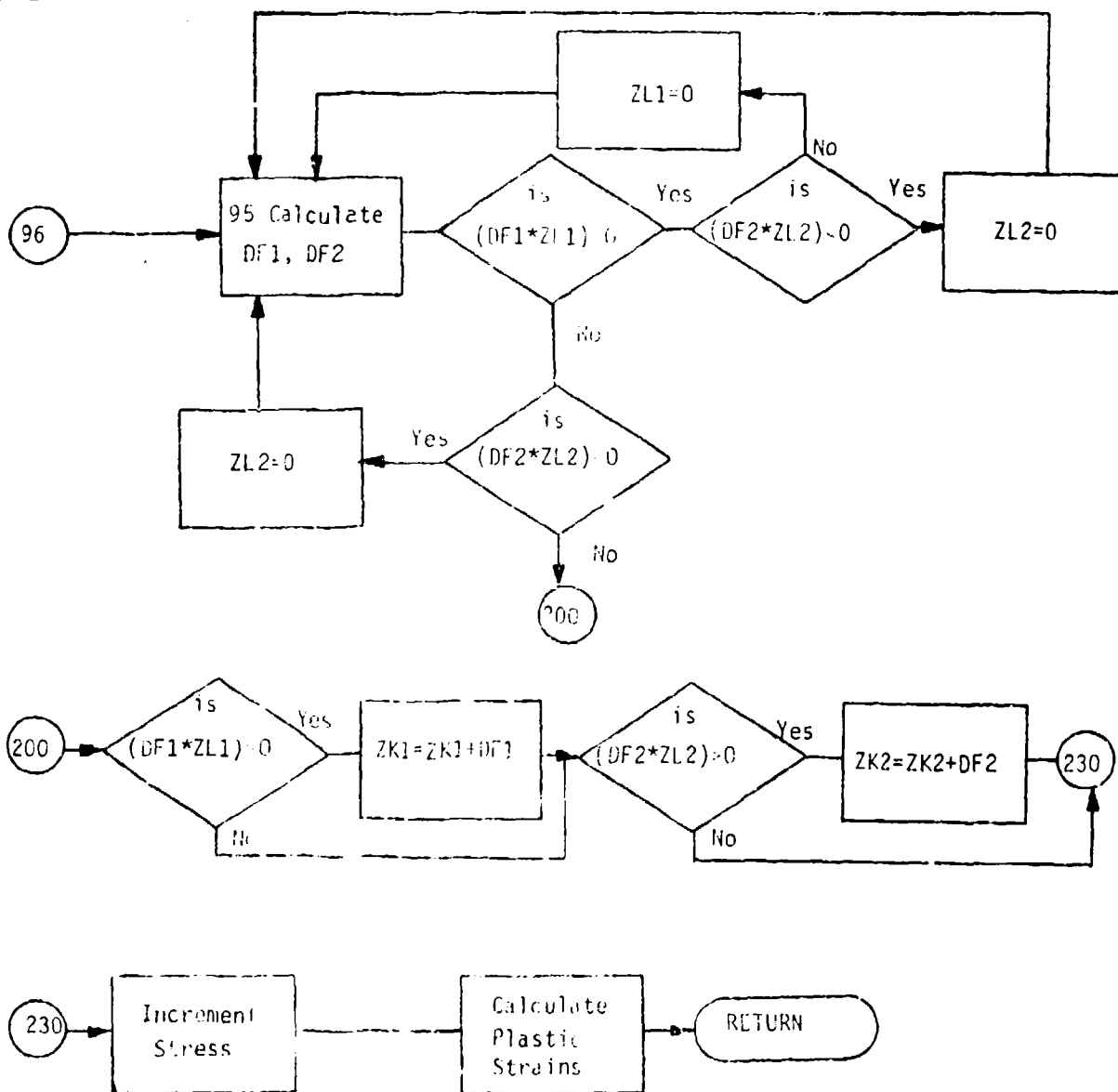


Figure 53 (Continued)

```

C-----THIS SUBROUTINE CALCULATES STRESS INCREMENTS FROM AN INPUT OF
C   STRAIN INCREMENTS, STATE OF STRESS, PLASTIC STRAIN, AND THE YIELD
C   FUNCTION CONSTANTS
C-----THIS SUBROUTINE USES TWO STRAIN-HARDENING YIELD SURFACES
SUBROUTINE PLASTK(DEPST,SIGI,SI2P,EPSP1,ZK1,ZK2)
  DIMENSION SIGI(4),DEPST(4),DS(4),SIGDI(4),C(4,4),FS1(4),FS2(4),
  1   TDS(4),B1(4),B2(4),EPSP1(4),PDE(4)
  AGO=2.E+6
  AKBULK=3.E+6
  EL1=1.66667E+6
  DO 10 I=1,4
  DO 10 J=1,4
10  C(I,J)=0.
  DO 15 I=1,3
  DO 15 J=1,3
15  C(I,J)=EL1
  DO 20 I=1,4
20  C(I,I)=C(I,I)+2.*AGO
  AJ11=SIGI(1)+SIGI(2)+SIGI(3)
  AJ2I=0.
  DO 25 I=1,3
  SIGDI(I)=SIGI(I)-AJ11/3.
25  AJ2I=AJ2I+SIGDI(I)**2
  AJ2I=.5*(AJ2I+SIGI(4)**2)
  SJ2=AJ2I**.5
C-----CALCULATION OF ELASTIC STRESS INCREMENTS FOLLOWS
  DO 30 I=1,4
30  DS(I)=0.
  DO 35 I=1,4
  DO 35 J=1,4
35  DS(I)=DS(I)+C(I,J)*DEPST(J)
  ZL1=0.
  ZL2=0.
  T1=EXP(AJ11/40000.)
  T2=1000.*(12.2-11.*T1)
  T3=EXP((AJ11-800.)/700.)
  F1=SJ2-T2*(1.-T3)-ZK1
  F2=.5*AJ2I+2.*AJ11*AJ11-ZK2
C-----TEST FOR YIELDING FOLLOWS
  IF(F1) 50,40,40
  40  H1=(1.E-6)*(1.+100.*(-1.+EXP(120.*SI2P/(1.-.0001*AJ11)))) /
  1   (2.-7.E-5*AJ11)
  T4=.275*11*(1.-T3)+T2*T3/700.
  DO 42 I=1,3
  42  FS1(I)=(.5*SIGI(I)-.16666667*AJ11)/SJ2+T4

```

```

      FS1(4)=SIGI(4)*.5/SJ2
50  IF(F2)70,60,60
60  T5= -(2.0E-14)*SJ2*(1.-EXP(-SJ2/4000.)) * EXP(-((SJ2/9457.))**4))
      1/(1.-(5.E-4)*AJ1I)
      H2=-(7.02E-12)*(1.-EXP((AJ1I/23811.))**3))*EXP(AJ1I/60000.)+T5
      DO 65 I=1,3
65  FS2(I)=.5*SIGI(I)+3.8333333*AJ1I
      FS2(4)=.5*SIGI(4)
70  IF((F1.LT. 0.).AND.(F2.LT. 0.)) GO TO 250
C-----CALCULATION OF PLASTIC STRESS INCREMENTS FOLLOWS
      DO 82 I=1,4
      B1(I)=0.
2  B2(I)=0.
      DO 85 I=1,4
      DO 85 J=1,4
      B1(I) B1(I)+C(I,J)*FS1(J)
85  B2(I)=B2(I)+C(I,J)*FS2(J)
      AB1=0.
      AB2=0.
      AB3=0.
      AB4=0.
      AB5=0.
      DO 90 I=1,4
      AB1=AB1+FS1(I)*B1(I)
      AB2=AB2+FS1(I)*B2(I)
      AB3=AB3+FS1(I)*DS(I)
      AB4=AB4+FS2(I)*B2(I)
90  AB5=AB5+FS2(I)*DS(I)
      A1=1.+2.*H1*AB1
      A2=SJ2+2.*H1*AB2
      A3=2.*H1*AB3
      A4=.3333333*H2*AB2
      A5=4.*AJ1I+.3333333*H2*AB4
      A6=.3333333*H2*AB5
      IF(F1) 91,92,92
91  ZL2=A6/A5
      GO TO 96
92  IF(F2) 93,94,94
93  ZL1=A3/A1
      GO TO 96
94  T6=A1*A5-A2*A4
      ZL1=(A3*A5-A2*AB5)/T6
      ZL2=(A1*A6-A3*A4)/T6
95  CONTINUE
95  DF1=0.

```



```

    DF2=0.
    DO 100 I=1,4
    TDS(I)=DS(I)-B1(I)*ZL1-B2(I)*ZL2
    DF1=DF1+FS1(I)*TDS(I)
100  DF2=DF2+FS2(I)*TDS(I)
    TZL2=ZL2
    IF(DF1*ZL1) 102,130,130
102  IF(DF2*ZL2) 105,110,110
105  ZL2=0.
    GO TO 95
110  ZL1=0.
    ZL2=TZL2
    GO TO 95
130  IF(DF2*ZL2) 135,200,200
135  ZL2=0.
    GO TO 95
200  CONTINUE
C-----INCREMENTING OF YIELD SURFACES FOLLOWS
    IF(DF1*ZL1) 210,210,205
205  ZK1=ZK1+DF1
210  IF(DF2*ZL2) 230,230,220
220  ZK2=ZK2+DF2
230  DO 235 I=1,4
    SIGI(I)=SIGI(I)+TDS(I)
235  PDE(I)=FS1(I)*ZL1+FS2(I)*ZL2
    DEHP=EPSPI(1)+EPSPI(2)+EPSPI(3)
    IF(SI2P) 245,245,239
239  DO 240 I=1,3
240  SI2P=SI2P+(.5*EPSPI(I)/SI2P-DEHP/6.)*PDE(I)
    SI2P=SI2P+(.5*EPSPI(4)/SI2P)*PDE(4)
    GO TO 248
245  SI2PS=((PDE(1)-PDE(2))**2+(PDE(2)-PDE(3))**2+(PDE(3)-PDE(1))**2)
1    /6.+PDE(4)**2
    SI2P=SQRT(SI2PS)
248  DO 249 I=1,4
249  EPSPI(I)=EPSPI(I)+PDE(I)
    GO TO 300
250  CONTINUE
    DO 260 I=1,4
260  SIGI(I)=SIGI(I)+DS(I)
300  RETURN
    END

```

APPENDIX B

INELASTIC THICK WALLED CYLINDER PROGRAM

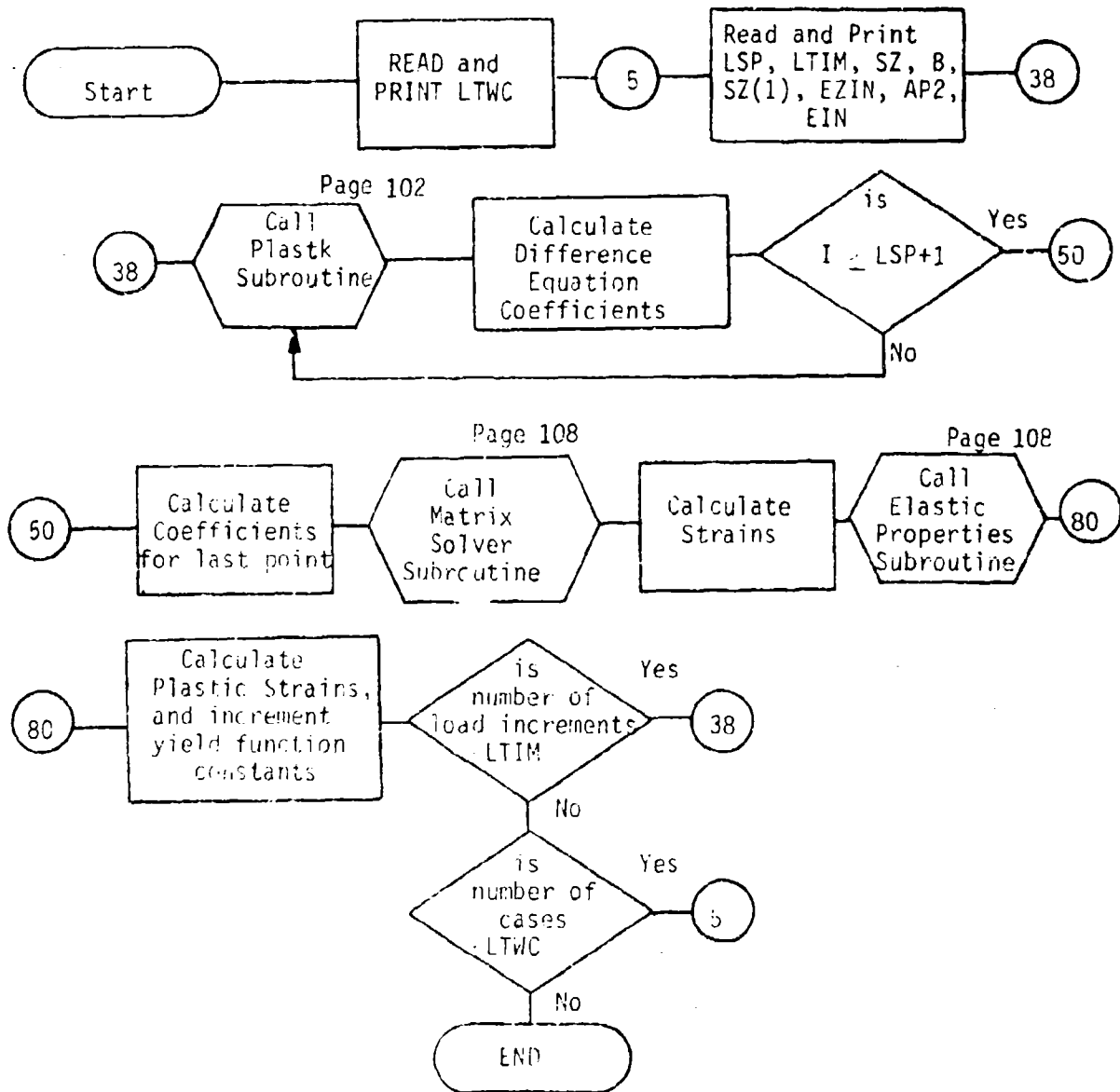


Figure 54. Inelastic cylinder program flow chart.

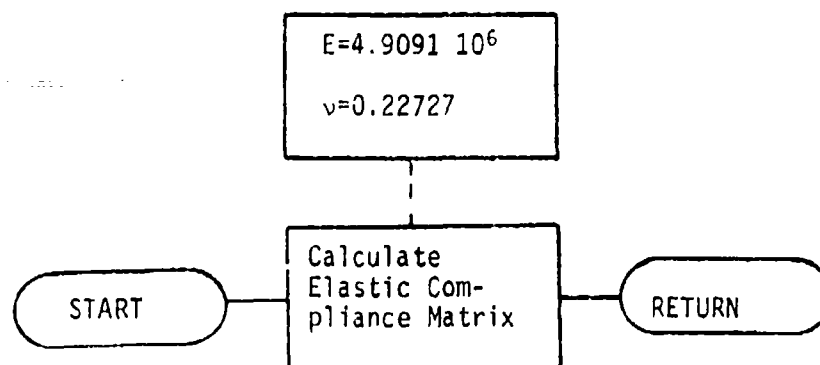


Figure 55. Flow Chart of elastic coefficient subroutine of cylinder program.

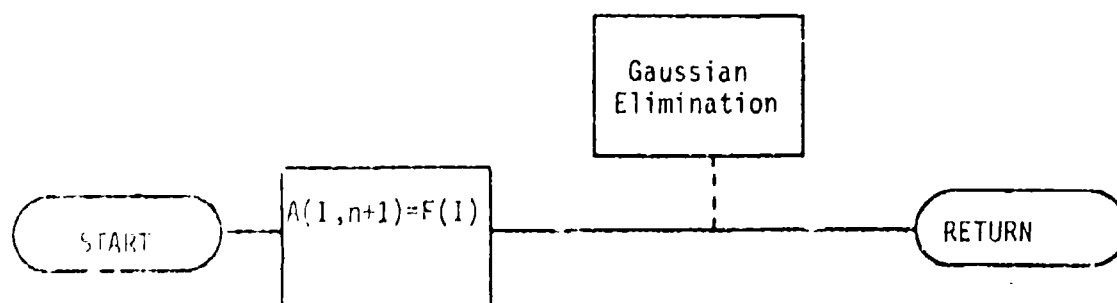


Figure 56. Flow chart of matrix solver subroutine of cylinder program.

```

[FC],IS MAIN,MAIN
  DIMENSION ST(40,40),SR(40,40),SZ(40),ET(40),ER(40),EZ(40),
1  U(40,40),C(4,4),F(40),X(40),B(40),A(40,41),PE(3),
2  S(4),XP2(40),T(40,3),EE(3),A1(4),A2(4),GP1(30,3),GP2(30,3),
3  BK1(30),BK2(30),D(3,3)
30 FORMAT (7(/, 11E12.4),/,E16.4)
  READ 10,LTWC
  DO 100 NTW=1,LTWC
  READ 10,LSP,LTIM
10 FORMAT (2I5)
  H=2./LSP
  P=3.5
  PRINT 15,H,LTIM
15 FORMAT (/ /,5X,*,THICK WALLED CYLINDER*,10X,*,RADIAL MESH =*,
1  F8.4,*,INCH*,10X,I5,*, LOADING STEPS*)
  NN=LSP+1
  READ 25,SZ(1),EZIN,AP2,EIN
25 FORMAT (4E20.8)
  PRINT 25,SZ(1),EZIN,AP2,EIN
  DO 20 I=1,NN
  ST(I,1)=0.
  SR(I,1)=0.
  ET(I)=EIN
  ER(I)=EIN
  EZ(I)=EZIN
  BK1(I)=0.
  BK2(I)=5.E+7
  XP2(I)=AP2
20 U(I,1)=(R+H*(I-1))*EIN
  R(1)=0.
  PRINT 30, (SR(I,1),I=1,NN), (ST(I,1),I=1,NN), (ER(I),I=1,NN),
1  (ET(I),I=1,NN), (XP2(I),I=1,NN), (EZ(I),I=1,NN), SZ(1)
  LTIM=LTIM+1
  READ 40,(R(J),J=2,LTIM)
  READ 40,(SZ(J),J=2,LTIM)
40 FORMAT (8F10.5)
  DO 37 J=2,LTIM
  SZ(J)=-SZ(J)
  R(J)=-R(J)
37 SR(1,J)=R(J)
  KK=3*NN-2
  S(4)=0.
  DO 100 J=2,LTIM
  DO 41 K=1,KK
  F(K)=0.

```

```

      DO 41 L=1, KK
41  A(K,L)=0.
      S(1)=SR(1,J-1)
      S(2)=ST(1,J-1)
      S(3)=SZ(J-1)
      CP2=XP2(1)
      CK1=BK1(1)
      CK2=BK2(1)
      CALL PLAST (D,S,CK1,CK2,CP2,A1,A2,C)
      DO 1 M=1,3
      GP1(1,MM)=A1(MM)
      GP2(1,MM)=A2(MM)
      1 T(1,M)=C(3,M)
C#####FIRST C EQUATION
      P=0.928*H
      A(1,1)=1.
      A(1,5)=-D(2,1)/P
      A(1,2)=D(2,1)/P-D(2,2)/R
      F(1)=ST(1,J-1)-(D(2,1)/P)*U(2,J-1)+(D(2,1)/P-D(2,2)/R)*U(1,J-1)
      1 +D(2,3)*(SZ(J)-SZ(J-1))
C#####FIRST B EQUATION
      A(2,5)=D(1,1)/P
      A(2,2)=(D(1,2)/R)-A(2,5)
      F(2)=B(J)-B(J-1)+D(1,1)/P*(U(2,J-1)-U(1,J-1))+D(1,2)/R*U(1,J-1)
      1 -D(1,3)*(SZ(J)-SZ(J-1))
C#####FIRST A EON, SECOND POINT
      A(3,6)=1.
      A(3,3)=2.*H/(R+H)
      F(3)=B(J)
      A(3,4)=-A(3,3)
      NT=LSP-1
C#####CENTRAL A EQUATIONS
      DO 45 I=3,NT
      L=3*(I-1)+1
      M=L-1
      A(M,L+2)=1.
      A(M,L-4)=-1.
      A(M,L-1)=2.*H/(R+(I-1)*H)
45  A(M,L)=-A(M,L-1)
      DO 50 I=2,LSP
      S(1)=SR(I,J-1)
      S(2)=ST(I,J-1)
      S(3)=SZ(J-1)
      CP2=XP2(I)
      CK1=BK1(I)

```

```

      CK2=BK2(I)
      CALL PLAST (D,S,CK1,CK2,CP2,A1,A2,C)
      DO 3 MM=1,3
        GP1(I,MM)=A1(MM)
        GP2(I,MM)=A2(MM)
3     T(I,MM)=C(3,MM)
      M=3*I-1
      L=M-1
C####CENTRAL B EQUATIONS
      RT=R+(I-1)*H
      A(L,L-1)=1.
      A(L,L+4)=-0.5*D(1,1)/H
      A(L,L-2)=-A(L,L+4)
      A(L,M)=-D(1,2)/RT
      F(L)=SR(I,J-1)-(0.5*D(1,1)/H)*(U(I+1,J-1)-U(I-1,J-1))-D(1,2)/RT
1     *U(I,J-1)+D(1,3)*(SZ(J)-SZ(J-1))
C####CENTRAL C EQUATIONS
      A(M,L)=1.
      A(M,L+4)=-0.5*D(2,1)/H
      A(M,L-2)=-A(M,L+4)
      A(M,M)=-D(2,2)/RT
      F(M)=-0.5*D(2,1)/H*(U(I+1,J-1)-U(I-1,J-1))-D(2,2)/RT*U(I,J-1)
1     +D(2,3)*(SZ(J)-SZ(J-1))
50  CONTINUE
      L=3*LSP-3
      M=L-3
C####NEXT TO LAST A EQUATION, NEXT TO LAST POINT
      A(L,M)=-1.
      A(L,L)=2.*H/(R+(LSP-1)*H)
      A(L,L+1)=-A(L,L)
C####NEXT TO LAST B EQN(ADDITION TO)
      A(L+1,L+4)=-0.5*D(1,1)/H
      A(L+2,L+4)=-0.5*D(2,1)/H
      L=3*LSP+1
      M=L-1
      RT=R+(LSP*H)
C####LAST A EQUATION
      A(M,M-3)=1.
      A(M,M)=H/RT *1.057
C####LAST C EQUATION
      S(1)=SR(NN,J-1)
      S(2)=ST(NN,J-1)
      S(3)=SZ(J-1)
      CP2=XP2(NN)
      CK1=BK1(NN)

```

```

CK2=PK2(NN)
CALL PLAST (D,S,CK1,CK2,CP2,A1,A2,C)
DO 4 MM=1,3
GP1(NN,MM)=A1(MM)
GP2(NN,MM)=A2(MM)
4 T(NN,MM)=C(3,MM)
P=1.091*H
A(L,P)=1.
A(L,L)=- (D(2,2)/RT+D(2,1)/P)
A(L,L-2)=D(2,1)/P
F(L)=-D(2,1)/P*(U(I,J-1)-U(I-1,J-1)) -D(2,2)/RT*U(I,J-1)+D(2,3)*
1 (SZ(J)-SZ(J-1))
CALL SOL(NN,A,F,X)
ST(1,J)=X(1)
U(1,J)=X(2)
ST(NN,J)=X(3*NN-3)
U(NN,J)=X(3*NN-2)
DO 60 I=2,LSP
L=3*I
SR(I,J)=X(L-3)
ST(I,J)=X(L-2)
60 U(I,J)=X(L-1)
SR(NN,J)=0.
ST(NN,J)=X(3*NN-3)
U(NN,J)=X(3*NN-2)
DO 70 I=1,NN
70 ET(I)=U(I,J)/(R+(I-1)*H)
DO 71 I=2,LSP
ER(I)=(U(I+1,J)-U(I-1,J))/(2.*H)
71 EZ(I)=EZ(I)-(T(I,1)*(ER(I)-(U(I+1,J-1)-U(I-1,J-1))/(2.*H))+T(I,2)*
1 (ET(I)-U(I,J-1)/(R+(I-1)*H))-(SZ(J)-SZ(J-1)))/T(I,3)
ER(1)=(U(2,J)-U(1,J))/H
EZ(1)=EZ(1)-(T(1,1)*(ER(1)-(U(2,J-1)-U(1,J-1))/H)+T(1,2)*(ET(1)-
1 U(1,J-1)/R)-(SZ(J)-SZ(J-1)))/T(1,3)
ER(NN)=(U(NN,J)-U(NN-1,J))/H
EZ(NN)=EZ(NN)-(T(NN,1)*(ER(NN)-(U(NN,J-1)-U(NN-1,J-1))/H)+T(NN,2)
1 *(ET(NN)-U(NN,J-1)/(R+LSP*H))-(SZ(J)-SZ(J-1)))/T(NN,3)
S(3)=SZ(J)
CALL PROP(C)
DO 90 I=1,NN
DO 81 M=1,3
91 EE(M)=0.
S(1)=SR(I,J)
S(2)=ST(I,J)
DO 82 M=1,3

```

```

      DO 82 L=1,3
82  EE(M)=EE(M)+C(M,L)*S(L)
      PE(1)=EP(I)-EE(1)
      PE(2)=ET(I)-EE(2)
      PE(3)=EZ(I)-EE(3)
      PM=(PE(1)+PE(2)+PE(3))/3.
      DO 83 M=1,3
83  PE(M)=PE(M)-PM
      XP2(I)=0.
      DO 84 M=1,3
84  XP2(I)=XP2(I)+PE(M)*PE(M)
90  XP2(I)=SORT(XP2(I)*0.5)
      DO 220 I=1,NN
      DBK1=GP1(I,1)*(SP(I,J)-SR(I,J-1))+GP1(I,2)*(ST(I,J)-ST(I,J-1))+
1    GP1(I,3)*(SZ(J)-SZ(J-1))
      DBK2=GP2(I,1)*(SR(I,J)-SR(I,J-1))+GP2(I,2)*(ST(I,J)-ST(I,J-1))+
1    GP2(I,3)*(SZ(J)-SZ(J-1))
      IF(DBK1) 210,210,205
205  BK1(I)=BK1(I)+DBK1
210  IF(DBK2) 220,220,215
215  BK2(I)=BK2(I)+DBK2
220  CONTINUE
      PRINT 30, (SP(I,J),I=1,NN), (ST(I,J),I=1,NN), (ER(I),I=1,NN),
1    (ET(I),I=1,NN), (XP2(I),I=1,NN), (EZ(I),I=1,NN), (U(I,J),I=1,NN),
2    SZ(J)
130 CONTINUE
      END

```



```

IFOR,IS SUP1,SUB1
  SUBROUTINE PROP(C)
    DIMENSION C(4,4)
    EM=4.909091E+6
    EU=0.2272727
    DO 5 I=1,3
      DO 5 J=1,3
        5 C(I,J)=-EU/EM
      DO 10 I=1,3
        10 C(I,I)=1./EM
    RETURN
  END

```

```

IFOR,IS SUP2,SUB2
  SUBROUTINE SOL(NN,A,F,X)
    DIMENSION A(40,41),F(40),X(40)
    N=3*NN-2
    NP=N+1
    DO 2 I=1,N
      2 A(I,NP)=F(I)
      DO 9 I=1,N
        IP=I+1
        DO 9 J=1,N
          IF(I-J)4,9,4
          4 G=-A(J,I)/A(I,I)
          DO 3 K=IP,NP
            3 A(J,K)=A(J,K)+G*A(I,K)
          9 CONTINUE
        DO 10 I=1,N
          10 X(I)=A(I,NP)/A(I,I)
    RETURN
  END

```

```

(FOR,IS SUP3,SUP3
  SUBROUTINE PLAST(D,SIGI,ZK1,ZK2,SI2P,FS1,FS2,C)
C-----THIS SUBROUTINE CALCULATES STRESS INCREMENTS FROM AN INPUT OF
C   STRAIN INCREMENTS, STATE OF STRESS, PLASTIC STRAIN, AND THE YIELD
C   FUNCTION CONSTANTS
C-----THIS SUBROUTINE USES TWO STRAIN-HARDENING YIELD SURFACES
  DIMENSION SIGI(4),          SIGDI(4),C(4,4),FS1(4),FS2(4),
1    P1(3,3),P2(3,3),
2    P3(3,3),P4(3,3),D(3,3)
  AGO=2.E+6
  AKBULK=3.E+6
  EL1=1.66667E+6
  DO 10 I=1,4
    FS1(I)=0.
    FS2(I)=0.
  DO 10 J=1,4
10  C(I,J)=0.
  DO 15 I=1,3
  DO 15 J=1,3
15  C(I,J)=EL1
  DO 20 I=1,4
20  C(I,I)=C(I,I)+2.*AGO
    AJ1I=SIGI(1)+SIGI(2)+SIGI(3)
    AJ2I=0.
  DO 25 I=1,3
    SIGDI(I)=SIGI(I)-AJ1I/3.
25  AJ2I=AJ2I+SIGDI(I)**2
    AJ2I=.5*(AJ2I+SIGI(4)**2)
    SJ2=AJ2I**.5
    ZL1=0.
    ZL2=0.
    T1=EXP(AJ1I/40000.)

    T2=1000.*(12.2 -11.*T1)
    T3=EXP((AJ1I- 800.)/700.)
    F1=SJ2-T2*(1.-T3)-ZK1
    F2=.5*AJ2I+2.*AJ1I*AJ1I-ZK2
C-----TEST FOR YIELDING FOLLOWS
    IF(F1) 50,40,40
40  H1=(1.E-6)*(1. + 100.*(-1.+EXP(120.*SI2P/((1.-.0001*AJ1I)))) /
1    (2.-7.E-5*AJ1I)
    T4= .275*T1*(1.-T3) + T2*T3/700.
  DO 42 I=1,3
42  FS1(I)=(.5*SIGI(I)-.16666667*AJ1I)/SJ2 +T4
    FS1(4)=SIGI(4)*.5/SJ2
50  IF(F2)70,60,60
60  T5= -(2.0E-14)*SJ2*(1.-EXP(-SJ2/4000.)) * EXP(-((SJ2/9457.))**4))

```

```

1 / (1. - (5.E-4) * AJ1I)
H2 = - (7.02E-12) * (1. - EXP((AJ1I/23811.) ** 3)) * EXP(AJ1I/60000.) + T5
DO 55 I=1,3
55 FS2(I) = .5 * SIGI(I) + 3.8333333 * AJ1I
FS2(4) = .5 * SIGI(4)
70 IF ((F1.LT. 0.).AND.(F2.LT. 0.)) GO TO 250
C-----CALCULATION OF PLASTIC STRESS INCREMENTS FOLLOWS
DO 82 I=1,4
B1(I) = 0.
82 B2(I) = 0.
DO 85 I=1,4
DO 85 J=1,4
B1(I) = B1(I) + C(I,J) * FS1(J)
85 B2(I) = B2(I) + C(I,J) * FS2(J)
AB1 = 0.
AB2 = 0.
AB3 = 0.
AB4 = 0.
AB5 = 0.
DO 90 I=1,4
AB1 = AB1 + FS1(I) * B1(I)
AB2 = AB2 + FS1(I) * B2(I)
AB4 = AB4 + FS2(I) * B2(I)
90 CONTINUE
A1 = 1. + 2. * H1 * AB1
A2 = SJ2 + 2. * H1 * AB2
A4 = .7333333 * H2 * AB2
A5 = 4. * AJ1I + .3333333 * H2 * AB4
DO 280 I=1,3
DO 280 J=1,3
P1(I,J) = B1(I) * B1(J)
P2(I,J) = B1(I) * B2(J)
P4(I,J) = B2(I) * B1(J)
280 P3(I,J) = B2(I) * B2(J)
A8 = 2. * H1
A9 = 0.33333 * H2
290 A10 = A1 * A5 - A2 * A4
DO 295 I=1,3
DO 295 J=1,3
295 C(I,J) = C(I,J) - (P1(I,J) * A5 * A8 - P2(I,J) * (A2 * A9)
1 - P4(I,J) * A4 * A8) / A10 + P3(I,J) * A1 * A9
250 CONTINUE
300 CONTINUE
DO 310 I=1,2
C(I,3) = C(I,3) / C(3,3)
DO 310 J=1,2
310 D(I,J) = C(I,J) - C(I,3) * C(J,3) / C(3,3)
RETURN
END

```

APPENDIX C

DERIVATION OF EQUATIONS FOR λ_1 AND λ_2

In Section V it was stated that equations 13 and 15 could be developed by substitution of previous equations. This will be shown in this Appendix.

Starting with the hardening rule assumed in the form of equation 10, Section V

$$d\sqrt{I_2}^P = h_1 dK_1 \quad (10)$$

where by $d\sqrt{I_2}^P$ it is meant

$$d\sqrt{I_2}^P = \left\{ \frac{(d\epsilon_{11}^P - d\epsilon_{22}^P)^2 + (d\epsilon_{22}^P - d\epsilon_{33}^P)^2 + (d\epsilon_{33}^P - d\epsilon_{11}^P)^2}{6} + (d\epsilon_{12}^P)^2 + (d\epsilon_{23}^P)^2 + (d\epsilon_{31}^P)^2 \right\}^{1/2} \quad (46)$$

As explained in Section V, since $d\sqrt{I_2}^P$ involves strains from both yield surfaces, the flow rule given by

$$d\epsilon_{ij}^P = \frac{\partial F_1}{\partial \sigma_{ij}} \lambda_1 + \frac{\partial F_2}{\partial \sigma_{ij}} \lambda_2 \quad (7)$$

should be considered. This equation (7) is substituted into (10) to obtain the desired result. Making this substitution

$$\left\{ \left[\left(\frac{\partial F_1}{\partial \sigma_{11}} \lambda_1 + \frac{\partial F_2}{\partial \sigma_{11}} \lambda_2 \right) - \left(\frac{\partial F_1}{\partial \sigma_{22}} \lambda_1 + \frac{\partial F_2}{\partial \sigma_{22}} \lambda_2 \right) \right]^2 + \dots + \left[\frac{\partial F_1}{\partial \sigma_{12}} \lambda_1 + \frac{\partial F_2}{\partial \sigma_{12}} \lambda_2 \right]^2 + \dots \right\}^{1/2} = h_1 dK_1 \quad (47)$$

Since the yield surface segments are functions of the stress invariants

$\sqrt{J_2}$ and J_1 only, the derivatives can be written as

$$\frac{\partial F_1}{\partial \sigma_{ij}} = \frac{\partial F_1}{\partial \sqrt{J_2}} \frac{\partial \sqrt{J_2}}{\partial \sigma_{ij}} + \frac{\partial F_1}{\partial J_1} \frac{\partial J_1}{\partial \sigma_{ij}} \quad (48)$$

and similarly for F_2 . Noting the definition of the stress invariants, the derivatives can be written as

$$\frac{\partial \sqrt{J_2}}{\partial \sigma_{ij}} = \frac{\sigma_{ij}}{2\sqrt{J_2}} - \delta_{ij} \frac{J_1}{6\sqrt{J_2}} \quad (49)$$

$$\text{and } \frac{\partial J_1}{\partial \sigma_{ij}} = \delta_{ij}$$

$$\text{where } \delta_{ij} = \begin{cases} 0 & \text{if } i \neq j \\ 1 & \text{if } i = j \end{cases}$$

substituting equation C-3 into C-2 and rearranging gives

$$\begin{aligned} & \left\{ \frac{1}{6} \left[\frac{\partial F_1}{\partial \sqrt{J_2}} \left(\frac{\partial \sqrt{J_2}}{\partial \sigma_{11}} - \frac{\partial \sqrt{J_2}}{\partial \sigma_{22}} \right) \lambda_1 + \frac{\partial F_2}{\partial \sqrt{J_2}} \left(\frac{\partial \sqrt{J_2}}{\partial \sigma_{11}} - \frac{\partial \sqrt{J_2}}{\partial \sigma_{22}} \right) \lambda_2 \right. \right. \\ & \quad \left. \left. + \frac{\partial F_1}{\partial J_1} \left(\frac{\partial J_1}{\partial \sigma_{11}} - \frac{\partial J_1}{\partial \sigma_{22}} \right) \lambda_1 + \frac{\partial F_2}{\partial J_2} \left(\frac{\partial J_1}{\partial \sigma_{11}} - \frac{\partial J_1}{\partial \sigma_{22}} \right) \lambda_2 \right]^2 + \dots \right. \\ & \quad \left. + \left[\left(\frac{\partial F_1}{\partial \sqrt{J_2}} \frac{\partial \sqrt{J_2}}{\partial \sigma_{12}} + \frac{\partial F_1}{\partial J_1} \frac{\partial J_1}{\partial \sigma_{12}} \right) \lambda_1 + \left(\frac{\partial F_2}{\partial \sqrt{J_2}} \frac{\partial \sqrt{J_2}}{\partial \sigma_{12}} + \frac{\partial F_2}{\partial J_1} \frac{\partial J_1}{\partial \sigma_{12}} \right) \lambda_2 \right]^2 + \dots \right\} \\ & = h_1 dK_1 \end{aligned}$$

and using 49 simplifies this to

$$\left\{ \frac{1}{6} \left[\frac{\partial F_1}{\partial \sqrt{J'_2}} \left(\frac{\sigma_{11} - \sigma_{22}}{2\sqrt{J'_2}} \right)^{\lambda_1} + \frac{\partial F_2}{\partial \sqrt{J'_2}} \left(\frac{\sigma_{11} - \sigma_{22}}{2\sqrt{J'_2}} \right)^{\lambda_2} \right]^2 + \dots \right. \\ \left. + \left[\frac{\partial F_1}{\partial \sqrt{J'_2}} \frac{\sigma_{12}}{2\sqrt{J'_2}} \lambda_1 + \frac{\partial F_2}{\partial \sqrt{J'_2}} \frac{\sigma_{12}}{2\sqrt{J'_2}} \lambda_2 \right]^2 + \dots \right\} = h_1 dK_1$$

Factoring the terms gives

$$\left\{ \frac{1}{2\sqrt{J'_2}} \right\} \left\{ \frac{\partial F_1}{\partial \sqrt{J'_2}} \lambda_1 + \frac{\partial F_2}{\partial \sqrt{J'_2}} \lambda_2 \right\} \left\{ \frac{(\sigma_{11} - \sigma_{22})^2}{6} + \dots + \sigma_{12}^2 + \dots \right\} \\ = h_1 dK_1 \quad (50)$$

Noting that the last term is just $\sqrt{J'_2}$

$$\frac{1}{2\sqrt{J'_2}} \left\{ \frac{\partial F_1}{\partial \sqrt{J'_2}} \lambda_1 + \frac{\partial F_2}{\partial \sqrt{J'_2}} \lambda_2 \right\} \sqrt{J'_2} = h_1 dK_1 \quad (51)$$

and finally equation 13 of Section V is obtained as

$$\frac{\partial F_1}{\partial \sqrt{J'_2}} \lambda_1 + \frac{\partial F_2}{\partial \sqrt{J'_2}} \lambda_2 = 2 h_1 dK_1 \quad (13)$$

Equation 15 is obtained in a similar manner. Starting with the hardening rule assumed in the form

$$d\epsilon_{vc}^p = h_2 dK_2 \quad (11)$$

where by $d\epsilon_{vc}^p$ it is meant

$$d\epsilon_{vc}^p = (d\epsilon_{11}^p + d\epsilon_{22}^p + d\epsilon_{33}^p) \text{ segment } F_2 \quad (52)$$

As discussed in Section V, equation 11 involves the compaction strain from the F_2 segment of the yield surface only. Thus the strains obtained from this yield segment only should be used. These are given by

$$(d\epsilon_{ij}^p)_{F_2} = \frac{\partial F_2}{\partial \sigma_{ij}} \lambda_2 \quad (14)$$

Substituting equation 14 into equation 11 gives

$$\frac{\partial F_2}{\partial \sigma_{11}} \lambda_2 + \frac{\partial F_2}{\partial \sigma_{22}} \lambda_2 + \frac{\partial F_2}{\partial \sigma_{33}} \lambda_2 = h_2 dK_2 \quad (53)$$

Since F_2 has been assumed to be a function of $\sqrt{J_2'}$ and J_1 only, the derivatives can be expressed as done previously in C-3 for F_1 . Making this substitution gives

$$\lambda_2 \left\{ \frac{\partial F_2}{\partial \sqrt{J_2'}} \left[\frac{\sigma_{11} + \sigma_{22} + \sigma_{33}}{2\sqrt{J_2'}} - \frac{3J_1}{6\sqrt{J_2'}} \right] + \frac{\partial F_2}{\partial J_1} \left[3 \right] \right\} = h_2 dK_2 \quad (54)$$

Noting that the first term is zero gives

$$3 \frac{\partial F_2}{\partial J_1} \lambda_2 = h_2 dK_2 \quad (55)$$

and finally equation 15 of Section V is obtained as

$$\frac{\partial F_2}{\partial J_1} \lambda_2 = 1/3 h_2 dK_2 \quad (15)$$

REFERENCES

1. K. Newman, Chapter VIII Concrete Systems, Composite Materials, Elsevier Publishing Co., 1966.
2. Proceedings of an International Conference, The Structure of Concrete, London, Sept. 1968, Cement and Concrete Association, edited by A. E. Brooks and K. Newman.
3. H. E. Read and C. J. Maiden, The Dynamic Behavior of Concrete, Systems, Science and Software Report 3SR-707, August 1971.
4. W. S. Brown and S. R. Swanson, Constitutive Equations of Westerly Granite and Cedar City Tonalite for a Variety of Loading Conditions, DASA-2473, University of Utah Report, March 1970.
5. K. Newman and J. B. Newman, "Failure Theories and Design Criteria for Plain Concrete", Proc. Int. Conf. on Structures, Solid Mech. and Engr. Design in Civil Engr. Materials, Southampton Univ., Wiley-Interscience, 1971.
6. J. Isenberg, Inelastic and Fracture in Concrete, Thesis, Univ. of Cambridge, June 1966.
7. C. D. Johnson and E. H. Sidwell, "Testing Concrete in Tension and Compression," Mag. Concrete Research, Vol. 20, 221-228, 1968.
8. W. R. Wawersik, Detailed Analysis of Rock Failure in Laboratory Compression Tests, Thesis, Univ. of Minnesota, July 1968.
9. F. E. Richart, A. Brandtzaeg and R. L. Brown, A Study of the Failure of Concrete Under Combined Compressive Stresses, Univ. of Illinois, Engr. Expt. Station, Bul. No. 185, 1-102, 1928.
10. G. G. Balmer, V. Jones, and D. McHenry, Shearing Strength of Concrete Under High Triaxial Stress, Lab. Report SP-23, Bureau of Reclamation, Denver, Colo., Oct. 1949.
11. N. J. Gardner, "Triaxial Behavior of Concrete," ACI Jour. Feb. 1969.
12. J. Chinn and R. Zimmerman, Behavior of Plain Concrete Under Various High Triaxial Compression Loading Conditions, U.S. Air Force Weapons Lab. Tech. Report WL-TR-64-163, 1965.
13. D. W. Hobbs, "Strength of Concrete Under Combined Stress", Cement and Concrete Res., Vol. 1, 1971.
14. G. Winter, et al., Design of Concrete Structures, McGraw-Hill, 1964.
15. H. Kupfer, H. K. Hilsdorf, and H. Rusch, "Behavior of Concrete Under Biaxial Stress", Proc. Amer. Conc. Inst., Vol. 66, No. 8, Aug. 1969.

16. Y. Niwa, W. Koyanagi, and S. Kobayashi, "Failure Criterion of Lightweight Concrete Subjected to Triaxial Compression," Trans. JSCE, No. 147, July 1967.
17. J. E. Shale, "The Strength of Concrete Under Short-Term Static Stress," Proc. The Structure of Concrete, London, Sept. 1965, and Concrete Association, edited by A. E. Brooks and K. Newman.
18. D. J. G. Fry and J. Karki, "Strength of Concrete Under Combined Tensile and Compressive Stresses," Proc. Amer. Conc. Inst., Vol. 54, 829-839, 1958.
19. B. Bresler and K. S. Pister, "Failure of Plain Concrete Under Combined Stresses," Trans. Amer. Soc. Civ. Engr., Vol. 122, 1049-1059, 1958.
20. L. L. Mills and R. M. Zimmerman, "Compressive Strength of Plain Concrete Under Multiaxial Loading Conditions," ACI Jour., Vol. 67, 802-807, 1970.
21. P. R. Barnard, "Researches Into the Complete Stress-Strain Curve for Concrete," Mag. of Conc. Res., Vol. 16, December 1964.
22. A. H. Nilson, "Nonlinear Analysis of Reinforced Concrete by the Finite Element Method," ACI Jour., Vol. 65, 757-766, 1968.
23. S. R. Swanson, Development of Constitutive Equations for Rocks, Thesis, Univ. of Utah, December 1969.
24. I. Sandler and F. L. DiMaggio, Material Model for Rocks, DASA Report 2595, Oct. 1970, and I. Nelson, M. L. Baron and I. Sandler, Mathematical Models for Geological Materials for Wave Propagation Studies, DASA Report 2672, March 1971.
25. S. R. Swanson, A Multiple Yield Surface for Moderate Porosity Rocks, unpublished, Univ. of Utah, 1971.
26. W. Herrmann, "Constitutive Equations for Compaction of Porous Materials," Proc. ASME Winter Meeting, December 1971.
27. W. H. Taylor, "Concrete Technology and Practice," New York, Amer. Elsevier Publishing Co., Inc., 1965, and J. D. McIntosh, Concrete Mix Design, Second Edition, 1966, Cement & Concrete Association.
28. S. J. Green, J. D. Leasia, R. D. Perkins and A. H. Jones, "Triaxial Stress Behavior of Solenhofen Limestone and Westerly Granite," Jour. Geo. Res., Vol. 77, 3711-3723, July 1972.
29. W. F. Brace, "Effect of Pressure on Electric-Resistance Strain Gages," Exp. Mech., July 1964.
30. R. D. Binns and H. S. Mygind, Magazine Concrete Research, Vol. 1, 35, 1949.

31. K. Newman and L. Lachance, Proc. Amer. Soc. Testing Material, Vol. 64, 1044, 1964.
32. S. Walker and D. L. Bloem, "Effects of Aggregate Size on Properties of Concrete," Jour. of the American Concrete Institute, 89, Sept. 1960.
33. A. Mendelson, Plasticity: Theory and Application, MacMillan Co., New York, 1968.
34. W. S. Brown and S. R. Swanson, Stress-Strain and Fracture Properties of Nugget Sandstone, University of Utah Final Report UTEC ME 71-058 to Kirtland Air Force Base, New Mexico, 1971.
35. S. J. Green, R. M. Griffin and H. R. Pratt, Material Properties of a Shale for Shock Calculations, Terra Tek, Inc. Tech. Rept. TR 71-12, February 1971.
36. W. T. Koiter, "Stress-Strain Relations, Uniqueness and Variational Theorems for Elastic-Plastic Materials with a Singular Yield Surface," Q. Appl. Math., Vol. 11, 350-354, 1953.
37. Y. C. Fung, Foundations of Solid Mechanics, Prentice-Hall, 1965.
38. K. Mogi, "Effect of the Intermediate Principal Stress on Rock Failure," Jour. Geo. Res., Vol. 72, 5117, 1967.
39. K. Mogi, "Fracture and Flow of Rocks Under High Triaxial Compression," Jour. Geo. Res., Vol. 76, 1255-1269, 1971.
40. S. P. Timoshenko and J. N. Goodier, Theory of Elasticity, McGraw-Hill, 1970